MRI Techniques for the Visualization of Induced Magnetic Field Alterations for Cell Tracking and Interventional Procedures

Dissertation
der Mathematisch-Naturwissenschaftlichen Fakultät
der Eberhard Karls Universität Tübingen
zur Erlangung des Grades eines
Doktors der Naturwissenschaften
(Dr. rer. nat.)

vorgelegt von
Frank Eibofner
aus Tübingen

Tübingen
2015

Gedruckt mit Genehmigung der Mathematisch-Naturwissenschaftlichen Fakultät der Eberhard Karls Universität Tübingen.

Tag der mündlichen Qualifikation: 08.06.2015

Dekan:	Prof. Dr. Wolfgang Rosenstiel
1. Berichterstatter:	Prof. Dr. Dr. Fritz Schick
2. Berichterstatter:	Prof. Dr. Klaus Scheffler

Contents

Summary

The aim of this thesis was the development of visualization techniques for cell therapy and interventional procedures with Magnetic Resonance Imaging. Two post-processing techniques for the detection and discrimination of magnetically labeled cells were successfully implemented and experimentally verified in homogeneous phantoms and in an ex-vivo bovine liver. Both techniques are based on the effects of magnetic field alterations in gradient echo sequences. Variations in the frequency domain were utilized to generate highlighted areas around the labeled cells in the image domain, while suppressing magnetically homogeneous areas. The techniques mainly differed in the application of a frequency domain filter and hereafter in the further post-processing steps in the image domain. The aims of both techniques were a short calculation time of the post-processing algorithm and detectability of small aggregations of labeled cells. The highlighting of the areas with frequency variations in the resulting image, in contrast to depiction of them in conventional imaging as hypointensities, is beneficial for discriminating magnetically labeled cells from natural low signal tissue. The developed techniques are helpful for the tracking of magnetically labeled cells in immune- or stem-cell therapy.
Alterations of the magnetic field can also be utilized for the visualization of interventional devices. A basic spin echo imaging sequence was modified to release a trigger signal at an external output of the scanner. The trigger signal switched a direct current on a metallic conductor generating a magnetic field, which disturbed the homogeneity of the main magnetic field. A transient field alteration is generated, if the current is switched by the trigger only in certain time intervals during the sequence. In this case, distinct phase variations around the conductor, without image distortions in the remaining parts of the image, can be generated and assigned to the interventional device. The generated field alteration is controllable by amperage, thus the dimension of the phase variation in the image is scalable as well, which cannot be accomplished with visualization techniques based on susceptibility differences. This technique allows for flexible choice of sequence parameters to achieve the desired image contrast and simultaneously visualizes the interventional device without the need of additional scanning time.

Zusammenfassung

Ziel dieser Arbeit war die Entwicklung von Bildgebungstechniken in der Magnetresonanztomographie für die Zelltherapie und interventionelle Verfahren. Zwei Nachbearbeitungsalgorithmen zum Nachweis von magnetisch markierten Zellen wurden entwickelt und erfolgreich getestet. Beide Techniken basieren auf Effekten, die in Gradienten-Echo Sequenzen durch Feldstörungen hervorgerufen werden. Dazu wurden Veränderungen im Frequenzraum ausgenützt um im Bildraum Bereiche um die markierten Zellen hell darzustellen und gleichzeitig homogene Bildbereiche signalarm darzustellen. Die Techniken unterscheiden sich dabei vor allem in der Verwendung des Frequenzraumfilters und in den Nachbearbeitungsschritten im Bildraum. Das Hauptaugenmerk bei der Entwicklung der Nachbearbeitungstechniken lag auf einer kurzen Rechenzeit und auf dem Nachweis von kleinen Zellhaufen. Der Vorteil der Darstellung von markierten Zellen mit positivem Kontrast, im Gegensatz zur Darstellung derselben in konventionellen Bildern als Signalauslöschungen, liegt in der Möglichkeit, diese von Bildbereichen, die von Natur aus signalarm sind, zu unterscheiden. Die hier entwickelten Techniken sind hilfreich für den Nachweis und die Darstellung des Migrationsverhaltens von magnetisch markierten Zellen in der Stamm- oder Immunzelltherapie.
Störungen des Magnetfelds können auch bei der Sichtbarmachung von interventionellen Instrumenten ausgenützt werden. Eine einfache Spin-Echo Sequenz wurde so modifiziert, dass ein Triggersignal an einem Ausgang des MR-Scanners bereitgestellt wurde. Das Triggersignal wurde verwendet, um einen Gleichstrom durch einen Messingleiter fließen zu lassen, der dadurch ein magnetisches Feld erzeugte welches die Homogenität des statischen Magnetfelds störte. Eine zeitlich begrenzte Feldstörung wurde erzeugt, in dem der Gleichstrom nur zu bestimmten Zeiten während der Sequenz geschaltet wurde. Dadurch wurden Veränderungen im Phasenbild in der Nähe des Leiters erzeugt, wobei die restlichen Bildbereiche nicht beeinflusst wurden, die eindeutig dem interventionellen Instrument zugeordnet werden konnten. Die Feldstörung und damit die Größe der Phasenvariation ist durch die angelegte Stromstärke steuerbar, was mit Techniken, die auf Suszeptibilitätsunterschieden beruhen, nicht möglich ist. Diese Technik erlaubt eine flexibele Wahl von Sequenzparametern um den gewünschten Bildkontrast zu erreichen und gleichzeitig eine Sichtbarmachung des interventionellen Geräts mit nur einer Bildaufnahme.

Chapter 1

Introduction

1.1 Development of Magnetic Resonance Imaging

It was in the winter holidays of 1922 when Otto Stern and Walther Gerlach implemented an experiment which proofed the quantization of magnetic moments as predicted by the Bohr-Sommerfeld hypothesis [Ger22]. They sent a beam of silver particles through an inhomogeneous magnetic field and observed their deflection. Instead of the classically expected single spot centered around the beam, two separated areas could be identified on a photographic plate. They concluded that the magnetic moment of the silver atom can only take two states with respect to the magnetic field.
Inspired by this experiment, Isidor Rabi postulated that a transition between the two states could be induced by a electromagnetic field of the according frequency. He sent a beam of lithium chloride molecules through two inhomogeneous magnetic fields, which were separated by a gap. The source of the adjustable electromagnetic field was mounted in the gap, and the deflection of the beam, dependent on the frequency of the radiation, was observed by a detector. Rabi realized that the measured resonances could be used to identify types of atoms or the structure of molecules [Rab39].
In 1946, Edward Purcell, Henry Torrey and Richard Pound measured the nuclear magnetic resonance effect in bulk materials for the first time [Pur46]. Only one month later a second group of scientists, Felix Bloch,

William Hansen, and Martin Packard, obtained a resonance signal from water protons [Blo46]. In the following years, the nuclear magnetic resonance technique was used for spectroscopic measurements while being constantly improved. Several techniques, introduced in those days, like pulsed radio frequency excitation or the spin echo technique developed by Erwin Hahn [Hah50], are still of prominent significance.
However, it was not before the early 1970s, when nuclear magnetic resonance took the step from a technique for the assessment of molecular structures to a diagnostic tool in medicine. At this time Raymond Damadian measured different relaxation times for healthy tissue and malignant tumors [Dam71]. Although, the assumption that relaxation time is a reliable indication for malignant tumor tissue could not stand the test of time, Damadians discovery was the first implementation of magnetic resonance for medical purposes.
Two years later, Paul Lauterbur [Lau73] laid the cornerstone for the acquisition of images with the magnetic resonance technique. Imaging became possible by the introduction of additional linear magnetic field gradients in all three spatial directions. In 1977, two major breakthroughs happened: On one side, Raymond Damadian succeeded in the acquisition of the first magnetic resonance image of a human [Dam77]. On the other side Peter Mansfield invented an imaging technique that allowed the acquisition of images in a clinical relevant time [Man77]. The acquisition time for one image was reduced from several hours to some seconds with Echoplanar Imaging (EPI), however at the cost of reduced image quality.
The mathematical basis for imaging was an arrangement of signal frequencies and phases in an entity that is now known as k-space. The k-space formalism as the basic mathematical concept of Magnetic Resonance Imaging (MRI) was introduced and developed by Richard Likes [Lik79], Donald Twieg in 1983 [Twi83], and Stig Ljunggren [Lju83], and is still valid.
In 1986, another major step toward rapid image acquisition was taken by introduction of the FLASH (Fast Low Angle SHot) sequence [Haa86]. In contrast to spin echo imaging, the acquisition time could largely be reduced while maintaining image quality and contrast.
In 1988, the first contrast agent for MRI was approved for usage in clinical practice. This contrast agent was based on Gadolinium whose presence in a tissue reduces the longitudinal relaxation time. Since then, Gadolinium contrast agents have been used mainly for tumor identification or angiography several hundred million times all over the world.
Soon after the first MR scanners were established in medical facilities,

two main medical branches had emerged: Diagnostic imaging of the muscoloskeletal system and the visceral organs (at first the stationary organs could be measured and later, with more dedicated sequences, also the thorax region, the abdomen and the heart) and on the other side diagnostics of the brain and the central nervous system. Examinations of the brain, in particular functional investigations of the same, were based on a discovery of Linus Pauling, who realized in 1936 that the magnetic properties of hemoglobin are dependent on the oxygenation level [Pau36]. In 1990, Seiji Ogawa recognized the importance of this effect for the visualization of activity in parts of the brain making functional MRI an integral part of neurological sciences.
From the beginning of MRI in clinical practice in the early 1980s, the technical components (magnet, gradient system, radio frequency system, and computers) were rapidly and constantly improved. Most of the advances contribute to acceleration of the imaging process, by acquisition of a reduced amount of k-space data, and the increase of resolution with the step to higher field strengths. Other improvements were made to obtain more homogeneous fields or to achieve more uniform excitation profiles. The aim of these was to improve image quality through reduction of image artifacts. The general development of computer hardware allowed the acquisition of more data in the same time and also the online reconstruction and even post-processing of large datasets in almost real time.

1.2 Thesis Background

The quality of MR images can be influenced in the negative sense by many effects, whose results in the image are summarized by the term artifacts. Sources of artifacts can either be of technical or of biological nature. Technical sources are inhomogeneities of the magnetic field or the radio frequency system in combination with imperfect shimming gradients, resulting in large scaled image distortions and phase variations. These artifacts are often unavoidable during image acquisition and have to be removed by post-processing.
The most common biological source of artifacts is the living subject itself, which is examined. This source can be further divided in two branches: motion and fat. Since the MR system is not expecting that the subject is moving, every motion, i.e., heartbeat, blood flow, breathing, and fidgeting, results in a false encoding during data acquisition and furthermore

to blurring in the final image. These artifacts can be avoided to some extent by special acquisition techniques, electrocardiographic gating, or short time breath holds. Artifacts due to fat occur during data acquisition, because of different precession frequencies of fat protons and water protons. This type of artifact is commonly referred to as chemical shift artifact. Chemical shift artifacts cause serious problems with echoplanar imaging techniques or by usage of long readout times, but can be avoided with additional saturation pulses or binomial excitation schemes.
Apart from the artifacts with a negative effect on image quality, some artifacts are deliberately generated for a certain purpose. In this case, the artifacts can help for the detection or discrimination of structures from a homogeneous background. The artifacts can be generated for instance by microscopic, magnetic perturbers with high susceptibility differences toward the generally diamagnetic tissue. The disturbances of the local magnetic field due to the perturbers can be strong enough for a visible effect but do not compromise the remainder of the image. In medicine, the perturbers can be used to label certain cells and monitor their fate during follow-up examinations. One purpose of this thesis was the development of methods for visualization of cells labeled with superparamagnetic iron oxide particles. Hereby, the focus was on generating positive contrast in the areas around the labeled cells, instead of signal voids. Visualization of the labeled cells with positive contrast is advantageous, because discrimination between natural low signal tissue areas can be achieved.
Artifacts play also a role in the visualization of medical instruments. In minimally invasive treatments, thin and often flexible instruments are brought into the patient and have to be navigated to their port of call. Detection of these instruments can be challenging especially if imaging is performed in the region of the body. There, several structures in combination with a low image resolution can mask the instrument. However, the artifact induced by the instrument shall not hide the organ which is perforated or navigated through. For the visualization of interventional instruments an approach based on the application of direct currents was developed.

1.3 Thesis Structure

In Chapter 2, the basics of Magnetic Resonance Imaging, which are of importance for the understanding of the following chapters, are given.

The techniques for positive contrast imaging of iron oxide labeled cells are summarized in Chapter 3. Section 3.2 is part of the work "Positive contrast imaging of iron oxide nanoparticles with susceptibility-weighted imaging" published in Magnetic Resonance in Medicine [Eib10]. Section 3.3 has been taken from "Utilizing echo-shifts in k-Space for generation of positive contrast in areas with marked susceptibility alterations" published in Magnetic Resonance in Medicine [Eib12].
In Chapter 4, the technique for the visualization of conductive, current carrying structures is presented which has been published in Medical Physics as "Magnetic resonance visualization of conductive structures by sequence-triggered direct currents and spin echo phase imaging" [Eib14].

Chapter 2

Theory *

2.1 Physical Basis of Nuclear Magnetic Resonance

2.1.1 Spin and Magnetic Moment

With the development of quantum mechanics, the intrinsic angular moment or spin $\vec{I}$ was introduced as an additional property of elementary and composite particles. Due to its quantum-mechanical nature, the spin can only take distinct values. The basis of the quantized values is the reduced Planck constant $\hbar$ ($\hbar = 6.626 \cdot 10^{-34} Js$). Particles can be divided in two groups: fermions with spin values that are half-integer multiples of $\hbar$, and bosons with spin values that are integer multiples of $\hbar$. Electrons, protons, and neutrons are fermions with $\vec{I} = 1/2$, whereas the photon as the elementary particle of electromagnetism is a boson with $\vec{I} = 1$. The quantization of the spin can be summarized by:

- The magnitude of $||\vec{I}||$ is related to the spin quantum number I by $||\vec{I}|| = \hbar\sqrt{I(I+1)}$.
- The projection of $\vec{I}$ on the z-axis is given by $I_z = m\hbar$.

where the magnetic quantum number m can take the values $m =$

*Sources for the theory chapter were [Kop56, Abr83, Bri88, Can91, Chr92, Cal93, Che95, Sli96, Haa99, Ber04, Ber05, Lev08, Haa11]

Nucleus	$^{1}_{1}\mathbf{H}$	$^{13}_{6}\mathbf{C}$	$^{19}_{9}\mathbf{F}$	$^{23}_{11}\mathbf{Na}$	$^{31}_{15}\mathbf{P}$
$\gamma/2\pi$ [MHz/T]	42.58	10.71	40.08	11.27	17.25

Table 2.1: Gyromagnetic ratios for MR relevant nuclei.

$-I, -I+1, ..., I-1, I$ resulting in $2I+1$ possible values for I_z. Atomic nuclei are composed of different numbers of protons and neutrons and can be classified by the AZE notation, where A is the mass number, Z the atomic number, and E the name of the element. For nuclei with more than one nuclear constituent, a total angular moment is formed by summing up of the single spins and orbital angular moments. Since orbital angular moments are always integral multiples of $\hbar$, the total angular moment of a nucleus is dependent on A and Z:

- If A and Z are even, the total angular moment is zero, because protons and neutrons can each form pairs of opposite spins.
- If A is even and Z is odd, the total angular moment is integral, because the surplus proton and neutron cannot form a pair of opposite spins with each other.
- If A is odd, the total angular moment is half-integral.

In analogy to a rotating particle with an electric charge in classical electrodynamics, atomic nuclei with a non-zero total spin $\vec{I}$ generate a magnetic moment $\vec{\mu}$ while spinning. The magnetic moment of a nucleus is directly proportional to the spin

$$\vec{\mu} = \gamma \vec{I}$$

The proportionality constant γ is the gyromagnetic ratio which can be calculated with

$$\gamma = g_n \frac{\mu_n}{\hbar}$$

where g_n is the g-factor, a nucleus specific constant and μ_n the nuclear magneton ($\mu_n = 5.051 \cdot 10^{-27} JT^{-1}$) which is the natural unit for the magnetic moment. Some gyromagnetic ratios for nuclei used in MRI are given in Table 2.1.

2.1.2 Nuclei in an External Magnetic Field

Without an external magnetic field, the magnetic moment of a nucleus has no preferred orientation, since both possible levels (for $\vec{I} = 1/2$) are

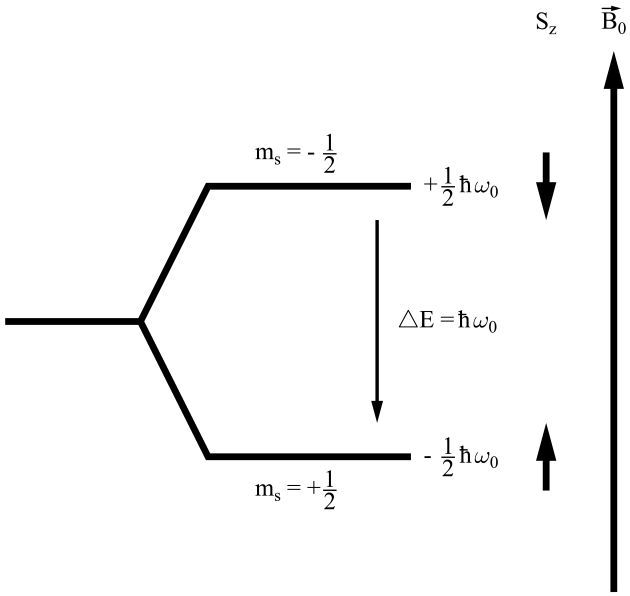

Figure 2.1: Zeeman energy levels for a spin 1/2 nucleus in an external magnetic field B_0. The level for the spin parallel to B_0 is energetically lower.

energetically equivalent or degenerate. When placed in an external magnetic field with a magnetic flux density $\vec{B}_0$ and $||\vec{B}_0|| = B_0\hat{z}$, the magnetic moment can align either parallel or anti-parallel to $\vec{B}_0$. The degenerate energy levels in absence of $\vec{B}_0$ are split into two levels with different energies, known as Zeeman effect. The energy difference between the degenerate level with $\vec{B}_0 = 0$ and the split levels is $\Delta E = \pm\mu_z B_0$ with $\mu_z = \pm m\gamma\hbar$. The energy of the split levels is then

$$\begin{aligned} E_{-1/2} &= E_0 - (-1/2\gamma\hbar B_0) \\ E_{+1/2} &= E_0 - (+1/2\gamma\hbar B_0) \end{aligned}$$

The negative energy difference reflects an energetically higher level, since in this case the magnetic moment that is orientated anti-parallel to $\vec{B}_0$.

The energy difference between the two split levels is

$$E = \gamma \hbar B_0$$

which is the energy mandatory to shift a nucleus in the energetically higher level and to change the orientation of its magnetic moment from being parallel to $\vec{B}_0$ to anti-parallel. This energy, connected with a change of the spin $\Delta m = \pm 1$, has to be transported by a photon. The energy of the photon can be expressed by

$$E_{RF} = \hbar\omega = \gamma \hbar B_0$$

or

$$\omega_L = \gamma B_0$$

This equation provides the condition for resonant absorption of a photon by a nucleus. Since only one photon can be absorbed by a nucleus, because of the quantum-mechanical selection rule $\Delta m = \pm 1$, in order to be shifted in a higher energy level, the frequency of the photon has to match the precession frequency of the magnetic moment, which is called Larmor frequency ω_L. Vice versa, an excited nucleus can emit a photon with ω_L to return to the energetically lower level.

2.1.3 Magnetization

Generally, more than one nucleus is necessary for a measurable effect in MRI. Considering the Avogadro constant, one mole of hydrogen consists of $6.022 \cdot 10^{23}$ molecules. Although the level with parallel orientation of the magnetic moment is energetically preferable for the hydrogen nuclei (denoted as protons here), the surplus of these protons toward those in the energetically higher level is relatively small, due to thermal effects. The ratio of the number of protons in the lower energy level to those in the higher energy level can be calculated with Boltzmann statistics (Boltzmann constant $k_B = 1.381 \cdot 10^{-23} JK^{-1}$)to

$$\frac{N_{+1/2}}{N_{-1/2}} = exp\left(\frac{\Delta E}{k_B T}\right) = exp\left(\frac{\gamma \hbar B_0}{k_B T}\right)$$

With a typical humanoid body temperature of $T = 310K$ and $B_0 = 1.5T$ the surplus in the lower energy level is only ≈10 ppm. However, for one mole of water, 10 ppm equals about $6 \cdot 10^{18}$ protons, which is enough for a

measurable effect. The surplus of protons in the lower energy level results in a net magnetization of:

$$M_0 = \frac{N}{V}\frac{I(I+1)\gamma^2\hbar^2 B_0}{3k_B T} = \frac{N}{V}\frac{\Delta E}{2k_B T}\mu_z$$

The number of protons N in the volume V is an important value in MRI referred to as proton density or spin density ρ.
In the equation for the magnetization most parameters are constant. This includes the temperature T as well as the proton density ρ. Therefore, higher magnetization in a certain probe can only be achieved by an increase in magnetic field strength B_0. Within the range of clinically relevant field strengths and temperatures (with the high temperature approximation $\hbar\omega_L << k_B T$), the magnetization of a probe is linearly dependent on B_0. Considering the high natural abundance and the dependency of M_0 on the gyromagnetic ratio γ, the water proton is the most significant nucleus for clinical MRI.

2.1.4 Reflection

The basics of magnetic resonance can be described by two physical theories: quantum mechanics and classical electrodynamics. While the quantum mechanical description is more fundamental, most of the interactions between the sample and the electromagnetic fields can be vividly explained in the classical picture, in particular for clinical MRI, which is most often performed on non-interacting, spin 1/2 nuclei. In the classical picture, magnetic moments of identical nuclei in a certain volume are summed up to a magnetization vector $\vec{m}$. Magnetization vectors of chemically or magnetically different nuclei can finally form the net magnetization $\vec{M}$ of the certain volume. The interactions of this net magnetization vector with the electromagnetic fields can be depicted by a simple vector equation [Fey57]. The time dependent evolution of the magnetization is then described by the phenomenological Bloch equations.

2.1.5 Magnetization in the Rotating Frame

It is convenient to describe the motion of a magnetization vector in a rotating frame rather than in the Cartesian laboratory frame. The rotating frame provides simplifications and more depicting representation of the

interaction between precession and application of time varying magnetic fields for excitation. In general, a vector $\vec{p}_{lab}(t)$ can be expressed in a frame rotating around the z-axis with ω by

$$\begin{bmatrix} p_{lab,x} \\ p_{lab,y} \\ p_{lab,z} \end{bmatrix} = \begin{bmatrix} cos\omega t & sin\omega t & 0 \\ -sin\omega t & cos\omega t & 0 \\ 0 & 0 & 1 \end{bmatrix} \begin{bmatrix} p_{rot,x} \\ p_{rot,y} \\ p_{rot,z} \end{bmatrix}$$

With $\vec{\Omega} = -\omega\hat{z}$, the time derivative of $|\vec{p}_{lab}(t)|$ is then

$$\left(\frac{d\vec{p}_{lab}(t)}{dt}\right) = \left(\frac{d\vec{p}_{rot}(t)}{dt}\right) + \vec{\Omega} \times \vec{p}_{lab}(t)$$

The precession of a magnetization vector can be written in the laboratory frame

$$\left(\frac{d\vec{m}_{lab}(t)}{dt}\right) = \vec{m} \times \omega_L\hat{z}$$

and in the rotating frame

$$\left(\frac{d\vec{m}_{rot}(t)}{dt}\right) = \vec{m} \times \omega_L\hat{z} - \vec{\Omega} \times \vec{m} = (\omega_L - \omega)\vec{m} \times \hat{z}$$

Thus, in a frame rotating with the Larmor frequency, i.e., $\omega = \omega_L$, the precession of a magnetization vector in the laboratory frame is reduced to a stationary vector. On the other hand, the last equation can be rewritten to

$$\left(\frac{d\vec{m}_{rot}(t)}{dt}\right) = \gamma\vec{m} \times B_0 + \vec{m} \times \vec{\Omega} = \gamma\vec{m} \times \left(\vec{B}_0 + \frac{\Omega}{\gamma}\right)$$

where the effective magnetic field in the rotating frame is

$$\vec{B}_{eff} = \vec{B}_0 + \frac{\Omega}{\gamma}$$

Introducing the radio frequency excitation, the effective magnetic field $\vec{B}_{eff}$ can be considered a superposition of the external magnetic field B_0 and a second magnetic field B_1.

2.1.6 Radio Frequency Excitation

In order to generate a measurable signal in MRI, the magnetization has to be tipped away from its alignment parallel $\vec{B}_0$ toward the transverse

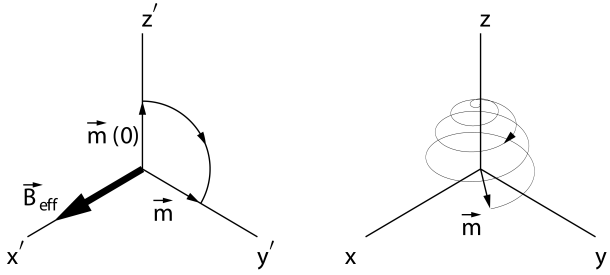

Figure 2.2: Motion of a magnetization vector $\vec{m}$ in the effective magnetic field $\vec{B}_{eff}$. In the rotating frame (left), the magnetization vector precessing with the frequency of the frame is simply tipped on the $y^{'}$-axis. In the laboratory frame, the same magnetization vector is spiraling down (right).

xy-plane. This can be achieved by use of an additional magnetic field $\vec{B}_1$ which is applied for instance on the x-axis of the rotating frame. Therefore, the additional magnetic field $\vec{B}_1$ has to be synchronized so that its x-component is static in a frame rotating with ω_L. A circularly polarized field, as the effective component of a linear polarized field, rotating with an angular frequency ω satisfies this condition and can be written as $\vec{B}_1 = B_1 \left(\hat{x}_{lab} cos\omega t - \hat{y}_{lab} sin\omega t\right)$ which is simplified in the rotating frame to $\vec{B}_1 = B_1 \hat{x}_{rot}$. The precession of a magnetization vector ω_1 in $\vec{B}_{eff}$ is then

$$\left(\frac{dm_{rot}(t)}{dt}\right) = \vec{m} \times \left[\hat{z}(\omega_L - \omega)\right] + \hat{x}_{rot}\omega_1 = \vec{\gamma} \times \vec{B}_{eff}$$

with $\vec{B}_{eff} = \left[\hat{z}(\omega_L - \omega) + \hat{x}_{rot}\omega_1\right]/\gamma$. In the special case, when the RF-frequency matches the frequency of the rotating frame, the equation of motion of the magnetization vector becomes

$$\left(\frac{dm_{rot}(t)}{dt}\right) = \omega_1 \vec{m} \times \hat{x}_{rot}$$

The application of such a RF-field lets the magnetization vector precess around the x-axis in the rotating frame. The motion of the components of

the magnetization vector are

$$\begin{aligned} m_{x,rot}(t) &= m_{x,rot}(0) \\ m_{y,rot}(t) &= m_{y,rot}(0)cos\omega_1 t + m_{z,rot}(0)sin\omega_1 t \\ m_{z,rot}(t) &= -m_{y,rot}(0)sin\omega_1 t + m_{z,rot}(0)cos\omega_1 t \end{aligned}$$

If the $\vec{B}_1$ field is switched only for a certain time τ, which is then called a RF-pulse, the magnetization vector is tipped from the thermal equilibrium $M_0\hat{z}$ toward the transverse plane. The tipping angle α_{FA} is commonly referred to as flip angle and can take any value from 0° to 360°. The flip angle is connected with $\vec{B}_1$ by $\alpha_{FA} = \gamma B_1 \tau$ which implies that for a fixed amplitude $||\vec{B}_1|| = B_1$ the flip angle is proportional to the duration τ of the RF-pulse.

2.1.7 Longitudinal Relaxation

The magnetization can be divided in a parallel and a transverse component with regard to the static magnetic field $\vec{B}_0$. For longitudinal relaxation, only the parallel component is of interest. In thermal equilibrium, the magnetization is fully aligned with $\vec{B}_0$ so that $\vec{M}_0 = M_0\hat{z}$. After being excited by a RF-pulse, the magnetization parallel to $\vec{B}_0$ is M_0 which can be zero for a flip angle $\alpha_{FA} = 90°$ or $M_z = -M_0$ for an inversion pulse with $\alpha_{FA} = 180°$. In any case, after a certain time the magnetization parallel to $\vec{B}_0$, or longitudinal magnetization, approaches the equilibrium magnetization M_0 again. In doing so, the magnetization has to dump the additional energy, gained by the RF-pulse, to leave the excited level. The additional energy is absorbed by the manifold of tissue in the excited volume, commonly referred to as lattice. The rate of change of $M_z(t)$ is proportional to the difference $M_0 - M_z$ and can be written as

$$\frac{dM_z}{dt} = \frac{1}{T_1}(M_0 - M_z)$$

with a proportionality constant T_1, or spin-lattice relaxation time, which is tissue dependent. The differential equation can be solved yielding the evolution of the longitudinal magnetization in an exponential form

$$M_z(t) = M_z(0)e^{-t/T_1} + M_0(1 - e^{-t/T_1})$$

with the equilibrium magnetization M_0 and the initial magnetization $M_z(0)$ after the application of the RF-pulse. The definition of T_1 reflects

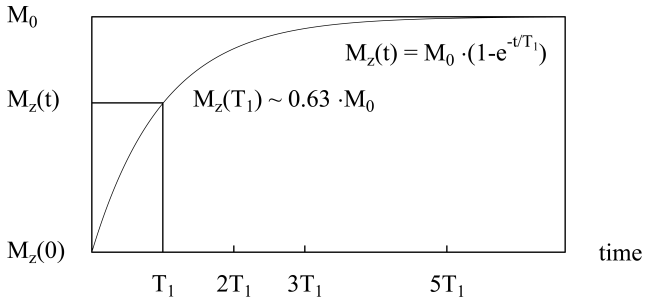

Figure 2.3: Regrowth of the longitudinal magnetization after being excited with an 90°-pulse. The longitudinal magnetization reaches $\approx 0.63M_0$ at the T_1-relaxation time. For $5T_1$, the equilibrium magnetization M_0 is proverbially reached.

the time, when $M_z(T_1) \approx 0.63M_0$ after being excited by a 90°-pulse. The time when the longitudinal magnetization reaches thermal equilibrium again is often estimated to $5T_1$.

2.1.8 Transverse Relaxation

By application of a RF-pulse with $\alpha_{FA} = 90°$, the magnetization $\vec{M}_0 = M_0\hat{z}$ is tipped into the xy-plane, so that the transverse component $\vec{M}_{xy} = M_0\hat{x}$ is at its maximum and aligned with the x-axis for instance. In an ideal case with an absolutely homogeneous magnetic field, the transverse magnetization would remain in this alignment with decreasing magnitude over time, due to transverse relaxation. However, the local magnetic field that affects a magnetization vector is a combination of the external magnetic field and the magnetic fields generated by neighboring nuclei known as spin-spin interactions. With different local magnetic fields for the single magnetization vectors, it results from the equation of the Larmor frequency that they precess with different frequencies. In the rotating frame, the individual magnetization vectors fan out and the transverse magnetization, i.e., the vector sum of the single magnetization vectors, decreases with time. This process is called dephasing in MRI. The decay rate of the transverse magnetization can be expressed as

$$\frac{d\vec{M}_{xy}}{dt} = -\frac{1}{T_2}\vec{M}_{xy}$$

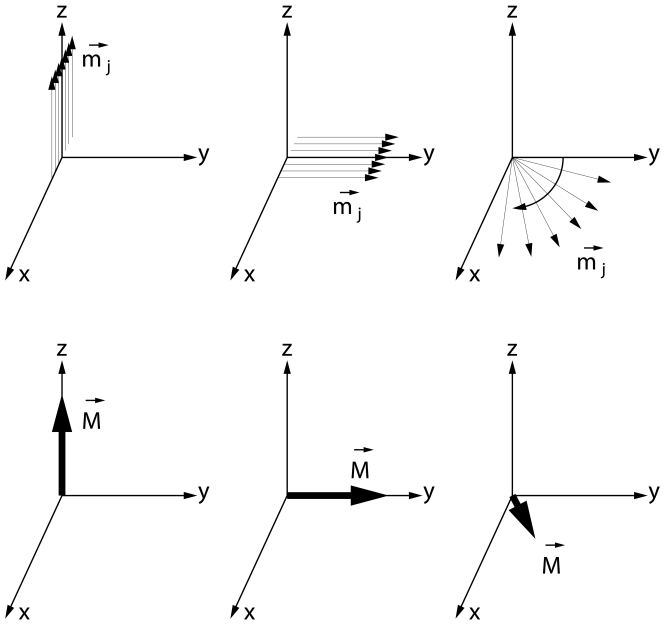

Figure 2.4: Before the application of the RF-pulse, the magnetization and the single magnetization vectors $\vec{m}_j$ are aligned with the z-axis. The RF-pulse tips the magnetization on the y-axis. Immediately after the end of the RF-pulse, the single magnetization vectors get out of phase due to spin-spin interaction. Hence, the magnetization decreases.

introducing T_2 as the spin-spin relaxation time. The solution of this equation reveals the exponential relation

$$\vec{M}_{xy}(t) = \vec{M}_{xy}(0)e^{-t/T_2}$$

The definition of T_2 reflects the time, when $\vec{M}_xy(T_2) \approx 0.37\vec{M}_{xy}(0)$. Additional to the influence of the neighbors on the local magnetic field, other disturbances can affect the precession frequency of the magnetization vectors. Summed up in the term field inhomogeneities, possible reasons can be because of MR scanner construction or by artificial humanoid components. In contrast to spin-spin interactions, which are time dependent, field inhomogeneities are most often static. Therefore, field in-

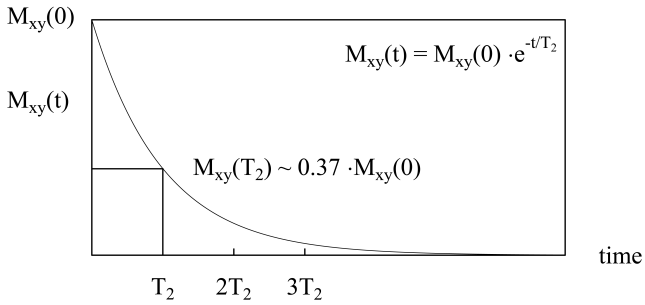

Figure 2.5: Decay of the transverse magnetization after the application of an RF-pulse. At the time T_2, 63% of $M_{xy}(0)$ have decayed.

Tissue	**Fat**	**Blood**	**CSF**	**GM**	**WM**	**Liver**	**Muscle**
T_1 [ms]	250	1200	4500	950	600	490	900
T_2 [ms]	60	200/100	2200	100	80	40	50

Table 2.2: T_1- and T_2-relaxation times of different tissues. For venous blood T_2 reduces because of deoxygenation of the hemoglobin.

homogeneities are recoverable with certain imaging sequences (neglecting diffusion effects), whereas dephasing effects due to spin-spin interactions are not. In the presence of field inhomogeneities a total relaxation time can be defined as

$$\frac{1}{T_2^*} = \frac{1}{T_2} + \frac{1}{T_2'}$$

with $T_2^{'}$ including the decay rate due to the field inhomogeneities. Some relaxation times of different human tissue are given Table 2.2.

2.1.9 Bloch Equations

The longitudinal and transverse relaxation effects of the magnetization in the presence of a static magnetic field can be combined to a vector equation

$$\frac{d\vec{M}}{dt} = \gamma\vec{M} \times \vec{B}_0 + \frac{1}{T_1}(M_0 - M_z)\hat{z} - \frac{1}{T_2}\vec{M}_{xy}$$

This empirically vector equation, known as Bloch equation, is the fundamental basis in MRI for the description of relaxation processes. In the

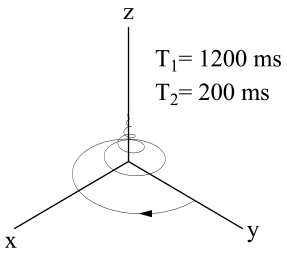

Figure 2.6: Combined regrowth of the longitudinal magnetization and decay of transverse magnetization in the laboratory frame for arterial blood.

rotating frame, the Bloch equation can be solved to

$$\begin{aligned} M_x(t) &= e^{-t/T_2}(M_x(0)cos\Delta\omega t + M_y(0)sin\Delta\omega t) \\ M_y(t) &= e^{-t/T_2}(M_y(0)cos\Delta\omega t - M_x(0)sin\Delta\omega t) \\ M_z(t) &= M_z(0)e^{-t/T_1} + M_0(1 - e^{-t/T_1}) \end{aligned}$$

with the assumption that the duration of the RF-pulse is short so that no relaxation occurs during excitation and $\Delta\omega$ as the difference between the rotation frequency of the frame and the precession frequency of the magnetization.

2.1.10 Signal Detection

With the magnetization in the transverse plane, rotating around the z-axis, a signal can be acquired in a coil based on Faraday's law of induction. Considering the magnetization as a bar magnet, its rotation generates a time depending magnetic flux, when the axis of rotation is not aligned parallel with the elongation of the magnet. The time dependent magnetic flux can induce an electromotive force in a coil. The electromotive force tends to counteract the time dependent flux which is known as Lenz's law resulting in

$$emf = -\frac{d\Phi}{dt}$$

The principle of induction is widely used for conversion of mechanical work into electricity, i.e., a generator.

In MRI, the induced electromotive force or voltage in a coil is proportional to the magnitude of the magnetization as a result of the excitation pulse and the sensitivity of the coil at the position of the magnetization. The induced voltage in the coil as the signal from the rotating transverse magnetization has to be recorded by two channels to define a signal magnitude and a signal phase unambiguously. The signal is therefore measured in a complex form, i.e., a real part corresponding to the x-axis and an imaginary part corresponding to the y-axis, which is demodulated by the rotating frame frequency. With the complex signal, stored in a matrix defined by the imaging gradients, an image can be reconstructed by Fourier-transformation.

2.2 Types of Magnetism

A magnetic field can be described by two physical quantities: The magnetic flux density B and the magnetizing field H. In vacuum B and H are proportional

$$B = \mu_0 H$$

with the proportionality constant μ_0 as the vacuum permeability ($\mu_0 = 4\pi \cdot 10^{-7} NA^{-2}$). By introducing material in the magnetizing field, the material is magnetized and changes the magnetic flux density according to its magnetization capability to

$$B = \mu_0 (H + M)$$

The magnetization M of the material can be written in terms of H

$$M = \chi_m H$$

introducing χ_m as the magnetic susceptibility, which has a constant value for a specific material. Defining further the relative permeability μ_r as

$$\mu_r = 1 + \chi_m$$

the relation between B and H in a material can be written as

$$B = \mu_0 (H + \chi_m H) = \mu_0 (1 + \chi_m) H = \mu_0 \mu_r H$$

The reaction of a material toward an external magnetic field, thus the magnetic susceptibility, depends on its atomic structure. In particular the atomic electron shell governs the influence of the material on the external magnetic field. Depending on the occupation of the atomic electron shell, the material can decrease or increase the magnetic field.

2.2.1 Diamagnetism

The weakest form of magnetism called diamagnetism is inherent to all materials. Diamagnetism can only be observed in materials with filled atomic electron shells. Atomic diamagnetism can be explained in a classical model with the circular motion of electrons in a magnetic field. The magnetic moment $\mu_e$of an electron in absence of an external magnetic field can be expressed by the induced current I around the area A defined by the radius of the circular loop r to $\mu_e = IA = I\pi r^2$. With the angular velocity of the electron ω_0 and its charge $-e$ ($e = 1.602 \cdot 10^{-19}C$) and mass m_e ($m_e = 9.109 \cdot 10^{-31}kg$) it follows

$$\mu_e = -\frac{e\omega_0 r^2}{2m_e} = -\frac{e}{2m_e}L$$

with the angular momentum $L = m_e r^2 \omega_0$. In an external magnetic field, the angular velocity of the electron is modified to $\omega = \omega_0 + \omega_L = \omega_0 + |\gamma|B_0$. The change of the angular momentum due to the external magnetic field in dependence of the electron's moment of inertia I_m is $\Delta L = I_m \omega_L = m_e r^2 \omega_L$ resulting in a change of the magnetic moment of

$$\Delta\mu_e = \gamma \Delta L = \gamma r^2 m_e |\gamma| B_0 = -\frac{e^2 r^2}{4m_e} B_0$$

Considering two electrons with opposite angular velocities, the magnetic moment without the magnetic field is compensated and the resulting induced magnetic moment in a diamagnetic material becomes

$$\mu_{dia} = -e^2 r^2 B_0 / 2m_e$$

Replacing the classical radius r with the quantum mechanical probability density $\langle r \rangle^2$ and supposing that the magnetization M equals the number of atoms n (with z electrons) multiplied by the magnetic moment μ_{dia}, the susceptibility of a diamagnetic material can be expressed by

$$\chi_{dia} = \frac{\mu_0 M}{B_0} = -\frac{\mu_0 n Z e^2}{6m_e} \langle r \rangle^2$$

As a consequence, materials with diamagnetic susceptibility decrease the magnetic field with the susceptibility being dependent on the probability density which increases for atoms with electrons in higher shells.

2.2.2 Paramagnetism

Materials with an unpaired electron have a magnetic moment which is the basis for paramagnetism. Without an external field, the magnetic moments in the material are randomly distributed, due to degenerate energy levels, resulting in a vanishing net magnetization. When brought into an external magnetic field, the degenerate energy level splits into multiple energy levels

$$E_j = -\vec{\mu}_e \vec{B} = m_j g \mu_B B_0$$

depending on the total angular moment J. The probability of occupancy p_j for electrons in the different energy levels is given by Boltzman's statistics

$$p_j = \frac{e^{-E_j/k_B T}}{\sum_j e^{E_j/k_B T}}$$

resulting in a mean magnetic moment in the direction of the external magnetic field of the material $\langle \mu_{para} \rangle = \sum \mu_j p_j$. Introducing the Brillouin-function $B_j$with

$$B_j(x) = \frac{2J+1}{2J} coth\left(\frac{(2J+1)x}{2J}\right) - \frac{1}{2J} coth\left(\frac{x}{2J}\right)$$

being dependent on the total angular momentum quantum number J, which can be derived by Hund's rules, and $x = gJ\mu_B B/k_B T$, the magnetization M of a paramagnetic material of n magnetic moments can be written as $M = n\langle \mu_{para} \rangle = ng\mu_B J B_j(x)$. Assuming a low external magnetic field B_0. as used in MRI, and clinical relevant temperatures T≈310 K, B_j can be approximated to $B_j(x) = ((J+1)x)/(3J)$ resulting in a magnetization of

$$M = ng^2 \mu_B^2 \frac{J(J+1)}{3k_B T} B_0$$

The susceptibility of a paramagnetic material is then, dependent on the temperature and the number of effective Bohr magnetons $p = g\sqrt{J(J+1)}$,

$$\chi_{para} = \frac{\mu_0 M}{B_0} = \frac{\mu_0 n p^2 \mu_B^2}{3k_B T}$$

As a consequence, paramagnetic materials increase the applied magnetic field. The influence of diamagnetic effects in paramagnetic materials can be omitted, since it is much smaller than the paramagnetic effect. Especially high paramagnetic values can be observed in rare earth elements like gadolinium or terbium, where the total angular moments result in high values for p≈10.

2.2.3 Ferromagnetism

In addition to paramagnetic effects, in some materials with unpaired electrons a spontaneous microscopic magnetization can occur in absence of an external magnetic field. This ferromagnetic effect can only be observed in three elements (iron, cobalt, and nickel) or in most of their alloys at room temperature. An explanation of ferromagnetism involves magnetic moments of electrons in neighboring atoms of the material. Instead of an anti-parallel alignment of these electrons, as predicted by classical electrodynamics through repulsion, it is energetically preferable for the electrons to align their magnetic moments parallel to each other. The reduction of the repelling energy that allows a parallel alignment can be derived in quantum mechanics from an exchange interaction of electrons in adjacent atoms when their orbitals overlap. In ferromagnetic materials, atoms can form large areas with parallel aligned magnetic moments called magnetic domains. The dimension of these domains is often in the range of micrometers, resulting in a manifold of magnetic domains in a macroscopic sample. In a virgin ferromagnetic material, the magnetic domains are randomly aligned canceling out each other so that the net magnetization of a macroscopic sample is zero. Although, the development of magnetic domains requires energy, which is stored in walls, separating the magnetic domains, this energy is lower than the energy that would be required to maintain a macroscopic magnetic field. If a ferromagnetic material is brought into an external magnetic field, the single domains are all aligned with the direction of the external field. In this state, the material is fully magnetized, resulting in a saturated magnetization. The saturation magnetization is much larger than the magnetization of a paramagnetic material, and is not increased at higher field strengths. Depending on the type of ferromagnetic material, the saturation magnetization can remain stable even if the external magnetic field is removed. This behavior which is called remanence is typical for hard iron and leads to a dependence of the magnetization on the external field known as hysteresis. This implies, that the magnetization of a ferromagnetic material is not linear related to an external field and a susceptibility value cannot be defined. In general, the ferromagnetic properties of a material are dependent on temperature. If a ferromagnetic material is heated above a certain temperature (Curie temperature) the spontaneous magnetization is destroyed by thermal energy. The Curie temperature of iron and cobalt is around 1000 K and for nickel about 600 K. Losing its ferromagnetic order, the material becomes para-

Material	**CuZn37**	**Zn**	**Tissue**	**Blood (A)**
χ_V $[10^{-6}]$ SI	-16.65	-15.7	-11.0 to -7.0	-10.06
Material	**Cu**	**Water**	**Blood (V)**	**Ti**
χ_V $[10^{-6}]$ SI	-9.63	-9.05	-6.62	182

Table 2.3: Magnetic susceptibility values (volume susceptibility in SI) for several interesting materials.

magnetic resulting in a significantly lower magnetization in an external field compared to the ferromagnetic saturation magnetization. In principle, heating is also a possibility to remove the remanent magnetization of a permanent magnet.

2.2.4 Ferrimagnetism

A special case of ferromagnetism can be observed in materials with a spinel structure. The general structure of a spinel can be notated as AB_2O_4 where A and B are metallic atoms or ions. Inside the crystal structure of the oxygen atoms, A and B occupy free tetrahedral and octahedral spaces forming crystal sub structures. In both sub structures, the magnetic moments are aligned parallel, whereas the sub structures themselves are aligned anti-parallel. A net magnetization, which is lower than the net magnetization of a ferromagnetic material, results from a different number of atoms occupying the single sub structures. Nonetheless, magnetic domains separated by domain walls are formed in these materials, which are called ferrimagnetic. The principal ferrimagnetic material with the largest net magnetization, which is also important in MRI, is magnetite $(Fe^{2+}(Fe_2^{3+}O_4)$.

2.2.5 Ferrofluids

Ferro- and ferrimagnetic materials can be used to generate ferrofluids. When such a material is reduced in size, it is possible to create a particle that consists of a single magnetic domain. Typical sizes of those particles are in the nanometer scale, with a particle radius of about 10 nm resulting in about 10^5 molecules per particle. The particles possess a permanent magnetic moment which is significantly larger than a magnetic moment of an equally sized sample of paramagnetic material. The single particles have to be coated to prevent flocculation through magnetic forces or chem-

ical interactions. A ferrofluid is obtained by bringing the coated particles in a suitable carrier fluid. In an external field, ferrofluids create a strong net magnetization which is saturated at relative low field strengths. In absence of an external field, the net magnetization is destroyed by thermal energy. Thus, ferrofluids show practically no remanence at room temperature and their magnetic properties are similar to paramagnetic materials at very low temperatures. This behavior of ferrofluids is therefore called superparamagnetism. Some susceptibilities which are of interest in MRI are given in Table 2.3.

2.2.6 Susceptibility Effects of Small Spherical Particles in an External Magnetic Field

Spins in a certain volume experience a local magnetic field which is a superposition of the external magnetic field and induced magnetic fields due to magnetic susceptibility in their vicinity. Considering superparamagnetic particles as small spheres, the local magnetic field can be calculated from the general formulation of a dipole field given by the Biot-Savart law. The magnetic dipole moment of a homogeneous sphere with a magnetization M and the radius a can be written as $\vec{m}_{tot} = (4\pi/3)a^3 M_0 \hat{z}$. The superposition of the external magnetic field $\vec{B}_0 = B_0\hat{z}$ and the induced magnetic field of the sphere at a position r with $r > a$ is then

$$\vec{B}_{out}(\vec{r}) = B_0\hat{z} + \frac{\mu_0}{4\pi}\frac{3(\vec{m}_{tot}\hat{r})\hat{r} - \vec{m}_{tot}}{r^3}$$

Assuming a constant field inside the sphere

$$\vec{B}_{in} = \mu_0\mu_r\vec{H} = \frac{1+\chi}{\chi}\mu_0 M\hat{z}$$

the constant magnetization can be calculated for appropriate boundary conditions, i.e., a continuous field across the surface of the sphere, to $\vec{M} = (3\chi B_0)/(\mu_0(3+\chi))$. The total magnetic field outside of the sphere in a polar coordinate system is obtained by replacing the dipole moment $\vec{m}_{tot}$ with the magnetization $\vec{M}$

$$\vec{B}_{out} = B_0\left(\hat{z} + \frac{\chi}{3+\chi}\left(\frac{a}{r}\right)^3(3cos\Theta\hat{r} - \hat{z})\right)$$

where the second addend in the brackets is the induced field change by the sphere. Since the induced magnetic field strength decreases with distance

and changes with the angle, spins in a certain volume experience different local magnetic fields. This results on one hand in frequency offsets and on the other hand reduces the T_2^*-relaxation time of the volume due to dephasing.

2.3 Imaging

2.3.1 Imaging Gradients

The Larmor frequency of a spin is linearly proportional to its position when a linear magnetic gradient field is present. The addition of the homogeneous, static, external magnetic field and a magnetic gradient in z-direction applied for a certain time yields

$$B_z(z,t) = B_0 + zG(t) = B_0 z + \frac{dB_z(t)}{dz}$$

The additional field $zG(t)$ alters the Larmor frequency linearly with z and G

$$\omega_G(z,t) = \gamma z G(t)$$

During the application of the gradient field the spins precess with different frequencies, resulting in a phase difference toward their neighbors (with a different z-position) if the field is switched off

$$\Phi_G(z,t) = -\int_0^t dt^{'} \omega_G(z,t^{'}) = -\gamma z \int_0^t dt^{'} G(t^{'})$$

The signal of a transverse magnetization with the spin density $\rho(z)$ induced in a receive coil is given by

$$s(t) = \int dz \rho(z) e^{i\Phi_G(z,t)}$$

where the phase is determined by the linear gradient field. Introducing the spatial frequency $k = k(t)$ with

$$k(t) = \gamma \int_0^t dt^{'} G(t^{'})$$

the z-dependence of the phase leads to

$$s(k) = \int dz \rho(z) e^{-i2\pi kz}$$

This expression is the basis for MRI pointing out that the signal $s(k)$ is the Fourier transform of the spin density. Extending the 1D equation to all three spatial dimensions with a set of three orthogonal gradients yields

$$\begin{aligned} s(k_x, k_y, k_z) &= \int\int\int dx\ dy\ dz\ \rho(x, y, z) e^{-i2\pi(k_x x + k_y y + k_z z)} \\ &= F[\rho(x, y, z)] \end{aligned}$$

In order to reconstruct an image, the whole k-space have to be filled with data points. Therefore, the gradients have to be active between excitation of the magnetization and readout. For a 2D image, the k-space can also be reduced to 2D by slice selective excitation. With a slice-selection gradient in z-direction the precession frequency of the spins becomes

$$f(z) = f_0 + \gamma G_z z$$

with $f_0 = f(z = 0)$. To excite a slice with a thickness of Δz, the RF-pulse has to satisfy the resonance condition for the spins in the slice. A RF-pulse with a boxcar excitation profile in the frequency domain, i.e., unity for frequencies in Δz and zero otherwise, has the shape of an infinitely long sinc-function in the time domain. A realistic RF-pulse is a time-truncated version of the sinc-function generating a imperfect boxcar excitation profile. The width of the frequencies Δf excited by the pulse is called bandwidth and is given by

$$BW_{RF} \equiv \Delta f = \gamma G_z \Delta z$$

The slice thickness TH is therefore

$$TH = \frac{BW_{RF}}{\gamma G_z}$$

Obviously, the slice-selection gradient has to be switched during the application of the excitation pulse to be effective. After the slice-selection, the 2D k-space is filled with data line by line. The selection of the line is performed by the phase encoding gradient. This gradient is linear along the y-direction for instance, and is switched after the RF-pulse has ended. The magnetization accumulates a phase, dependent on the y-position and the duration τ of the gradient. The encoded phase can be written in k-space terms as

$$k_y(G_y) = \gamma G_y \tau_y$$

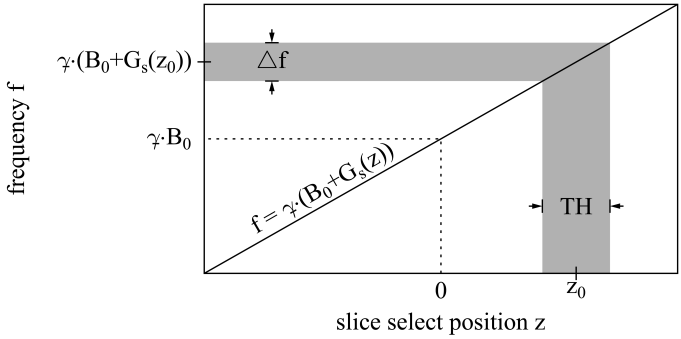

Figure 2.7: An additional gradient in z-direction results in a dependence of the precession frequency on the position along the slice select axis. A slice region of the thickness Δz is excited by a pulse with a bandwidth $BW = \Delta f$.

The amplitude of the phase encoding gradient G_y is varied in a step like fashion from one acquisition to the next, resulting in a separation of lines in k-space of

$$\Delta k_y = \gamma \Delta G_y \tau_y$$

After the selection of a specific line in k-space, the line is filled with data sampled during the application of the read gradient along the x-direction. The acquisition of the signal in the presence of the read gradient yields the Fourier transform of the spin density of the sample. If the read gradient is switched during a time Δt, the data points are sampled with an interval of

$$\Delta k_x = \gamma G_x \Delta t$$

For the acquisition of a 3D data set, the slice selective excitation of the 2D acquisition scheme can be supplemented by another phase encoding step in the z-direction. The acquisition of a 3D data set has many advantages. The slice thickness can be greatly reduced and the slice profile is improved. The acquisition of multiple slices increases the signal-to-noise ratio, whereas a higher possible resolution reduces signal loss due to T_2^* dephasing. On the other hand, the acquisition time is increased according to $TA(3D) = N_y N_z TR$, where N_y and N_z are the numbers of phase encoding steps along the y- and z-direction and TR is the repetition time, compared to $TA(2D) = N_y TR$ for a 2D acquisition.

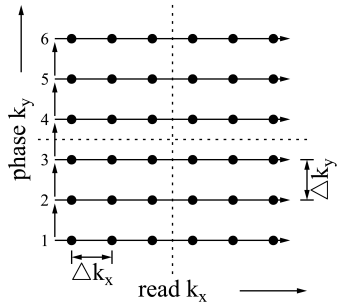

Figure 2.8: Filling of an Cartesian sampled k-space with data points. The phase encoding gradient defines the row that is filled with data points during the read gradient is active. After the first acquisition, the phase encoding gradient is decreased or increased defining another row until the k-space is completely filled.

2.3.2 Sequences

The switching of RF-pulses and gradients in a specific manner is summarized by the term sequence. There is a huge variety of sequences, comparable to the particle zoo, which generate images with different weightings, used by the radiologist to discriminate and identify tissues. Most of the sequences utilize the generation of an echo for the data acquisition. The echo allows for the acquisition of negative and positive frequency k-space points. The way the echo is created can differ fundamentally, however, two main sequence types can be identified. Some important definitions for the description of sequences are:

- Repetition Time (TR): time in ms between two RF-excitation pulses or time between the acquisition of two k-space lines, respectively.
- Echo Time (TE): time span in ms from the center of the RF-excitation pulse to the center of the generated echo.
- Readout Bandwidth (BW): Defines the range of frequencies sampled during the readout in Hertz per pixel and influences the duration of the readout gradient.

In general, T_1-weighted images are achieved by choosing TR to be similar to the shortest T_1 time of the examined tissues while reducing TE to a min-

imum (minimizing T_2 or T_2^*-relaxation effects). Proton density weighted images are achieved by reducing TE for the same reasons, but maximizing TR in order to minimize T_1-relaxation effects.

2.3.3 Gradient Echo

In gradient echo imaging sequences the echo is generated by switching of a bipolar gradient. A 2D gradient echo sequence starts with an excitation pulse with a variable flip angle α_{FA} simultaneous to a slice selection gradient (amplitude G_S, duration τ_{RF}). Immediately after the pulse and the slice selection gradient a rephasing gradient is switched to compensate for the induced phase shift by the former. The rephasing gradient mostly has the amplitude $-G_S$ but only half of the duration of the slice-selection gradient $1/2\tau_{RF}$. Additionally to the rephasing gradient, the phase encoding ($G_{P,max}$, τ_P) and the readout prephase gradient are switched. In terms of the k-space, the readout prephase gradient sets the starting point of the acquisition to the left side of k-space, thus allows for the acquisition of negative frequency k-space points. The prephase gradient has in principle the same properties as the slice rephasing gradient, i.e., negative amplitude $-G_R$ and half duration $1/2\tau_S$ of the following readout gradient with G_R and τ_S. During the readout gradient at the time $1/2\tau_S$ the dephasing effect of the prephase gradient is compensated

$$\int G_{RO}(t)dt = 0$$

thus the spins are in phase and generate the echo at TE. This echo formation is only valid for stationary spins. After the readout gradient is switched off, the sequence is repeated starting with the excitation pulse after TR. The only change in the second run of the sequence is the amplitude of the phase encoding gradient which is then $G_{P,max} - \Delta G_P$. Images acquired with gradient echo techniques are susceptible to field inhomogeneities resulting in a T_2^*-weighting. If the flip angle α_{FA} is chosen small, TR can be reduced according to Ernst's angle $\alpha_{Ernst} = arccose^{-TR/T_1}$ leading to a fast image acquisition commonly known as fast low-angle shot (FLASH).

2.3.4 Spin Echo

In spin echo imaging sequences the echo is generated by an additional RF-pulse in most cases a 180° pulse. Similar as the gradient echo sequence, the

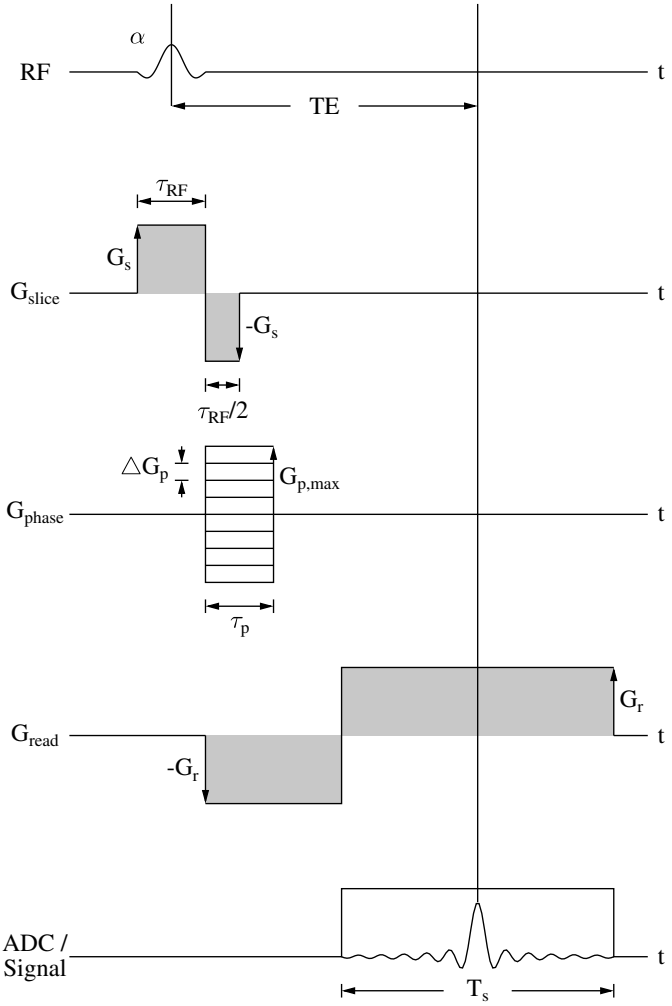

Figure 2.9: Diagram of a typical 2D gradient echo sequence. During excitation, the slice encoding gradient G_S is active. Immediately after the excitation pulse has ended, the slice rephasing gradient, the phase encoding gradient, and the readout dephaser are switched simultaneously. These gradients can be superimposed without influencing each other. This results in a reduced TE.

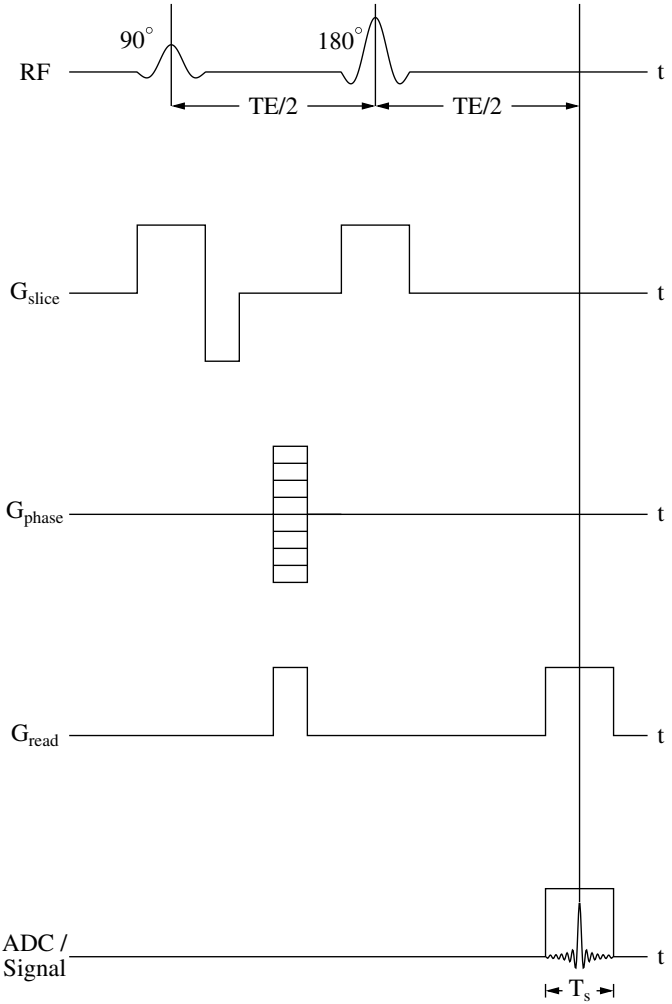

Figure 2.10: Diagram of a typical spin echo sequence. At the time $TE/2$ the 180° refocusing pulse is applied. The refocusing pulse rephases the spins at TE and invalidates effects from static field inhomogeneities. Thus, the spin echo experiment is capable of measuring T_2 relaxation times. Instead of a single 180° refocusing pulse several pulses can be used to accelerate acquisition.

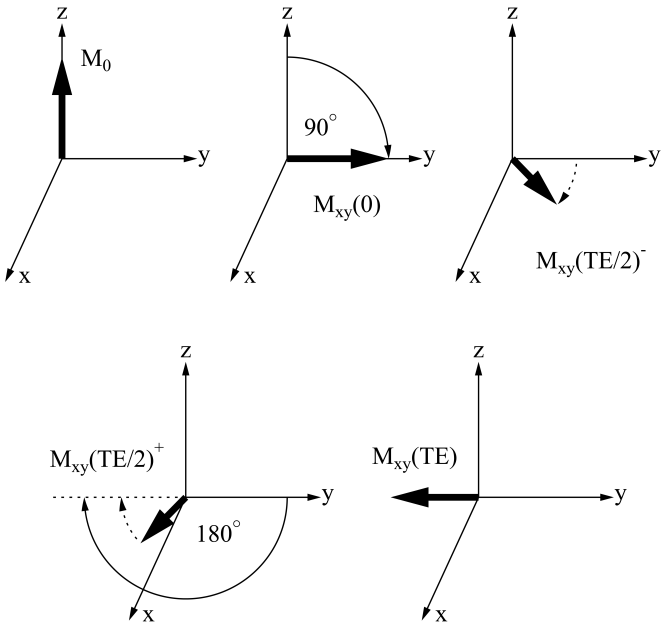

Figure 2.11: Generation of a spin echo. At the beginning of the sequence the magnetization is aligned with the static magnetic field along the z-axis. The 90° pulse flips the magnetization on the y-axis. In the time between the excitation and the refocusing pulse, the magnetization decreases due to local field inhomogeneities. The 180° refocusing pulse flips the magnetization again, so that the slower precessing spins achieve an advance. After a second time period $TE/2$, the phase values of the all spins are rephased at TE forming an echo.

spin echo sequence starts with an RF-excitation pulse and a simultaneously switched slice selection gradient. When the RF-excitation pulse is switched off, the slice rephasing gradient, as well as the phase encoding and read dephasing gradients are switched. At the time $TE/2$, the second RF-pulse and in most cases an additional slice selection gradient are switched. After a further time span of $TE/2$, i.e., at the echo time TE, the echo generated by the second RF-pulse is acquired with a readout gradient. The echo formation of the spin echo sequence can be explained in five steps. Before the application of the first RF-pulse, the spins are orientated along the z-axis. The 90° pulse flips the spins on the y-axis. During the time span between the first and the second RF-pulse, the single spins are exposed to different local magnetic field. The single spins get out of phase and the magnetization decreases. The phase Φ of a spin located at $\vec{r}$ for $0 < t < TE/2$ can be expressed as

$$\Phi(\vec{r}, t) = -\gamma \Delta B(\vec{r}) t$$

The second RF-pulse with 180° flips the spins a second time, for instance around the x-axis. Those spins which experience a lower local magnetic field now have a phase advance compared to the faster precessing ones, i.e.,

$$\Phi(\vec{r}, TE/2^{+}) = -\Phi(\vec{r}, TE/2^{-}) = \gamma \Delta B(\vec{r}) t$$

Since only the phase of the spins was inverted but not the direction of rotation, the spins continue to precess with the frequency defined by the local magnetic field. For $t > TE/2$ the phase of the spins is then

$$\begin{aligned} \Phi(\vec{r}, t) &= \Phi(\vec{r}, TE/2^{+}) - \gamma \Delta B(\vec{r})(t - TE/2) \\ &= -\gamma \Delta B(\vec{r})(t - 2TE/2) \\ &= -\gamma \Delta B(\vec{r})(t - TE) \end{aligned}$$

At the echo time TE, the spins are therefore all in phase again unaffected by local magnetic field inhomogeneities (when diffusion is neglected).

Chapter 3

Positive Contrast Imaging of Magnetically Labeled Cells

3.1 General Remarks on Positive Contrast Imaging

In stem- and immune-cell therapy, cells with special functionalities are given to the patient. These cells are meant to migrate in the body to their destination and accomplish a certain task. A successful therapy includes monitoring of the cells during therapy and in follow-up examinations. Among the three main clinical imaging modalities, MRI is the natural choice for this task. In contrast to computed tomography, the main advantages of MRI are the lack of ionizing radiation, the freedom of slice orientation and the manifold of image weightings. In contrast to ultrasound imaging, MRI offers higher resolutions and more than superficial images. However, the cells have to be prepared before they can be visualized by MRI. One way to do that is to label the cells prior to administration with a magnetic marker. The marker has to have two properties: First, its susceptibility (or relative permeability) has to differ from the background susceptibility. Second, the marker material has to be non-toxic in reasonable doses. A material with these properties is magnetite,

a mineral composed of iron and oxygen. Magnetite in its natural form is ferrimagnetic but can be processed to small particles coated by carboxydextran to become superparamagnetic. Such particles are commonly known as superparamagnetic iron oxide particles (SPIO).
SPIO particles are used in clinical MRI as contrast agent for tumor imaging for example in the liver. There, the particles are intravenously injected in the patient. Because of their small size, the particles are free to travel through the body. After being recognized by the Reticuloendothelial System, the particles are sequestered by phagocytic cells in the liver [Sta88]. These phagocytic or Kupffer cells are part of the healthy liver parenchyma, whereas tumors of the liver often lack Kupffer cells. The accumulation of the SPIOs in the healthy liver parts strongly reduces their signal intensity in an appropriate imaging sequence, resulting in highlighted areas of the pathological parts [Wan01]. Low concentrations of SPIO particles result in a dephasing effect in the microscopic scale [Yab98, Pin06a], while an increased concentration can even lead to inhomogeneities in the macroscopic scale [Yab98, Zie05]. In this case, the SPIO particles are used as a negative contrast agent.
For monitoring of magnetically labeled cells, it is, however, more desirable to identify the cells as hyperintensities in the resulting image, i.e., positive contrast. This can help to discriminate magnetically labeled cells from other low signal areas like connective tissue or partial volume effects [Cun05]. Using the characteristic field distortion in the vicinity of the particles, these areas can be highlighted against the particle free background with appropriate techniques.

3.2 Techniques

In the last years, different approaches to positive contrast imaging (PCI) of magnetically labeled cells have been proposed. The different PCI techniques can be separated into two branches: Sequence modifications and post-processing techniques. PCI techniques based on sequence modifications use special gradient switching schemes or frequency selective excitation or saturation pulses to suppress or excite the homogeneous background or the spins in the vicinity of the SPIOs, respectively.
A relative simple but nonetheless effective technique for PCI was described by Seppenwoolde et al. in 2003 called "The White Marker Phenomenon" [Sep03]. They considered the presence of a SPIO particle, or a param-

agnetic marker in general, as an additional gradient being active in its vicinity [Fra88, Rei97]. Dependent on the angle toward the main magnetic field, the additional gradient was either adding or subtracting to the imaging gradients. In their work, the readout dephasing gradient was chosen to be smaller than necessary for a conventional sequence. In regions where the additional gradients of the paramagnetic markers added to the reduced readout dephasing gradient to form the full gradient required for an echo, the pixels had normal signal intensity but appeared highlighted against the background where no additional gradients were apparent. This technique was further specialized for SPIOs [Man06] and for the reduction of partial volume effects [Sep07].
Another refinement of "The White Marker Phenomenon" called SIRMA (SIgnal Response MApping to dephasing) was presented in 2010 by Franconi et al. [Fra10]. They generated susceptibility maps by evaluating susceptibility induced shifts in the image domain. They collected a series of dephased images and assessed the signal intensity profiles pixel-by-pixel as a function of the dephasing gradients. In these profiles, susceptibility affected pixels could be identified, because the signal response profile maximum was shifted compared to non-affected pixels. The resulting susceptibility gradient map was calculated from the sign and the magnitude of the shifts. A major drawback of the technique, however, is the incapability of 3D imaging.
In 2005, Cunningham et al. showed that PCI of SPIO labeled cells is possible by use of frequency selective excitation [Cun05]. They used the additional gradient, cast by the labeled cells, to selectively excite and refocus a narrow frequency band of surrounding tissue. The frequency offset and the bandwidth, thus the excited frequencies around the cells, were the key parameters for this technique. They were capable of displaying a relative low number of cells whilst a complete suppression of the background tissue was accomplished.
However, both approaches, the gradient rephasing and the frequency selective excitation, suffer from a severe drawback: It is not possible to image both parts of the dipole field, i.e., the negative and the positive gradient lobe or frequency shift, simultaneously. Therefore, only half of the shifted frequencies in the vicinity of the labeled cells can be imaged with these approaches. A second drawback is the mandatory prior knowledge of the expected frequency shift or the number of labeled cells, respectively. This is necessary for the adjustment of the reduced readout dephaser and the excitation frequency. Otherwise imaging has to be repeated.

Another possibility to exploit an induced gradient in the vicinity of SPIO particles was described by Kim et al. [Kim09]. Instead of altering the dephasing gradient of a sequence, they shifted the 180° pulse of a spin echo sequence by a certain time without adaption of the readout window. The subtraction of the shifted acquisition from a spin echo reference image yields PCI in areas of susceptibilities [Par88].
The drawback of highlighting only half of the shifted pixels by use of incomplete gradients or frequency selective excitation can be overcome by frequency selective saturation. In 2007, Stuber et al. developed a jack of all trades sequence capable of visualizing labeled stem cells by use of an on resonant water saturation and simultaneous fat suppression [Stu07]. The actual excitation pulse was preceded by two inversion pulses and a frequency selective excitation of the on resonant water protons. The inversion pulses were used to invert the fat protons twice. The on resonant water protons and the off resonant water protons were inverted once, and due to a longer longitudinal relaxation time, reverted in the direction of the equilibrium magnetization by the second inversion pulse. At this time, the on resonant water protons were saturated by the frequency selective saturation pulse which did not affect the off resonant water protons. The latter were then excited by the actual pulse generating the only visible signal in the image. The degree of the background suppression was dependent on the bandwidth and the flip angle of the saturation pulse. This approach is capable of detecting the negative and the positive frequency shift and can be used with spin echo and gradient echo imaging sequences. The two inversion pulses for the suppression of the fat, however, require a relatively long preparation time, making this technique inefficient for coverage of larger areas.
A further frequency selective technique for PCI exploits a special characteristic of steady-state free precession (SSFP) sequences. In general, SSFP sequences belong to the gradient echo sequences, without the transverse magnetization being spoiled after the readout. Instead, the remaining transverse magnetization is used for the following sequence run. The interesting point about the SSFP sequences is that the generated signal is dependent on the frequency (of a pixel) and the used flip angle [Car58]. For high flip angles, on resonant frequencies are excited with a maximum, whereas off resonant frequencies are partly or completely suppressed. In contrast, this behavior is reverted for smaller flip angles. The feasibility for the detection of magnetically labeled cells by adjustment of the flip angle was shown by Dharmakumar et al. [Dha06, Dha07]. One striking

feature about SSFP sequences is the high signal per measuring time ratio, allowing short examination times.
A combination of frequency selective excitation and incomplete gradients on the basis of a SSFP sequence was independently proposed by Koktzoglou [Kok07] and Bieri [Bie07]. The sequences were not only run with a low flip angle for excitation of the frequency shifted parts but also one of the imaging gradients was dephased. With the dephased gradient being compensated in the vicinity of the SPIO particles (or other sources of susceptibility induced gradients), the unbalanced SSFP sequence became balanced. This resulted in a huge increase of signal compared to the remaining tissue. The advantage here is again the acquisition speed of the images as well as an improved homogeneous background suppression compared to SSFP sequences without dephasing gradients. Therefore, this technique is suitable for PCI of larger accumulations of magnetically labeled cells or monitoring of interventional devices in almost real time.
The drawback associated with sequence modification techniques is that the more successful the homogeneous background is suppressed the less anatomic details are visible. Sequence modification techniques generating high positive contrast therefore require a second scan to obtain an anatomic reference dataset [Liu08]. Obtaining the reference dataset with similar sequence parameters effectively doubles examination time, which is generally undesirable. Also, comparison of sequentially acquired images might suffer from artifacts due to tissue or patient motion in the time between acquisitions of images [Zho10].
These drawbacks can be overcome by post-processing techniques. Post-processing for the visualization of SPIO particles is most often performed by use of gradient echo acquisitions. In gradient echo sequences, local field distortions are directly visible in the magnitude images as areas with low signal intensities, because of a decreased local T_2^*-relaxation time. In the corresponding phase image, the local field distortions are displayed as phase variations. However, the spatial image domain is not the first choice for post-processing techniques. Since the local field distortions result in variations of the Larmor frequencies of the affected pixels, post-processing is preferably performed in the frequency domain or k-space. One of the first works exploiting the shifted frequencies in k-space was published in 1992 by Posse [Pos92]. In that work, a sliding window function was applied on the k-space data suppressing data points outside of the window. The reconstruction of the k-space points that were not suppressed by the window function resulted in images in which structures with frequency shifted

contributions were highlighted against the non-shifted background. This approach allowed for quantitative evaluation of shifted frequencies and their spatial localization in the sample. However, the resolution of the resulting images was reduced depending on the size of the window function, so that high accuracy in frequency determination was achieved at the cost of low image quality.
The same approach was used by Bakker et al. [Bak06], where positive contrast images with normal resolution were reconstructed from a high resolution gradient echo acquisition.
A further approach using a sliding window filter function for the detection of local field inhomogeneities was presented by Lai et al. [Lai96]. However, instead of filtering in the frequency domain, the complex image in the spatial domain and the magnitude image were filtered, respectively. Positive contrast was achieved by subtracting the magnitude of the complex filtered image from the filtered magnitude image. The non-commutivity between the operations filtering and calculating the magnitude resulted in positive contrast around structures inducing magnetic field inhomogeneities. The resulting commutator filter images also showed a reduced resolution.
In 2008, Dahnke et al. reported for another post-processing technique called "Susceptibility Gradient Mapping" (SGM) [Dah08]. The echo shift in k-space was evaluated from a 3D gradient echo dataset. Short-term Fourier transformation was applied on a small subset of voxels. The shift of the maximum in the resulting k-space was measured for all three directions of the 3D dataset to assess the field distortions generated by labeled cells. Positive contrast was achieved by calculating the magnitude of the sum of the shifts in each direction. In areas with labeled cells, the magnitude of the shifts was larger compared to homogeneous areas without labeled cells. Since the SGM technique also uses a sliding window function, the resolution of the positive contrast image is reduced. Due to multiple Fourier transformations the computation is relatively time consuming making this technique unsuitable for PCI with the patient in the scanner [Var11].
A post-processing technique similar to SGM was reported by Zhao et al. [Zha11]. However, instead of calculating the susceptibility map from k-space shift, gradient echo phase images were used. This "Phase Gradient Mapping" (PGM) technique showed high sensitivity for SPIO particles in phantom studies.

3.3 Motivation

Most of the described techniques for PCI have certain drawbacks dependent on how the positive contrast is achieved, i.e., sequence modification or post-processing. A very general drawback with sequence modifications is the modification itself. The problem can be that the modification might not be reproducible by other research groups or clinics due to different MR-scanner soft- and hardware that prohibit such modifications. Another problem with modified sequences is that only a positive contrast image is acquired at a time. Dependent on the quality of the homogeneous background suppression, anatomical structures can be suppressed as well. Then, a second anatomical image has to be acquired resulting in a longer measurement time. The combination of two images can also lead to misregistration due to motion of the subject between the two acquisitions. For post-processing algorithms, one severe drawback can be computation time of the resulting images. For clinical use of a post-processing algorithm, it is desirable that the computation time is not longer than instantaneous. Thus, calculation of a complete dataset should be possible in few seconds even with an external personal computer.
In this thesis, two post-processing techniques for the visualization of magnetically labeled cells with positive contrast were developed. Both techniques are based on conventional gradient echo acquisitions.
The first technique utilizes a slightly modified SWI post-processing algorithm for background suppression and highlighting of the labeled cells. Raw-data of a conventional gradient echo dataset is filtered to achieve a homogeneous phase image in regions without strong, localized field alterations. A mask image is calculated from the phase image, which is then multiplied by the magnitude image. In the resulting image, magnetically homogeneous parts of the sample are suppressed by the mask and areas near the labeled cells appear highlighted.
The second technique is also based on filtering of a raw-data image. However, the effect of the filter is directly evaluated in the magnitude image. Further post-processing steps are taken to automatically suppress homogeneous areas in the image while highlighting magnetically labeled cells. Both techniques are capable of displaying low aggregations of magnetically labeled cells while requiring little computation time.

3.4 Positive Contrast with Susceptibility Weighted Imaging

3.4.1 Introduction

Whenever a sample or subject is placed in an MR scanner, the homogeneity of the static magnetic field is disturbed due to the magnetic properties of the inserted material or tissue. Inhomogeneities of the static magnetic field result in different Larmor frequencies of the spins, defined by the Larmor equation

$$\omega_L = \gamma B$$

These inhomogeneities can affect image quality and the R_2^*-relaxation rate, which is one of the physical bases of tissue contrast in MRI. Field inhomogeneities can be classified as macroscopic or microscopic [Yab98]. Macroscopic field inhomogeneities are variations of the field in dimensions larger than a single pixel. They arise as large scaled susceptibility differences in the sample or subject, like tissue-air interfaces. Microscopic inhomogeneities are field distortions in molecular or cellular dimensions that are much smaller than the pixel size. These tissue specific inhomogeneities give information about structure and function of the tissue of interest, for example in functional MRI (fMRI) [Oga90a] or examinations of the trabecular bone structure [Sch96b]. The tissue specific relaxation constants can be changed by administration of paramagnetic or superparamagnetic contrast agents in order to improve MR contrast. SPIO particles can be used as contrast agents for MRI of the liver.
Here, a positive contrast technique that is based on the SWI technique developed by Haacke and Reichenbach [Haa04] is presented. The SWI method utilizes not only the magnitude image but makes use of the information from the phase image of a gradient echo dataset as well. A mask is generated from the phase image, which is multiplied by the magnitude image, resulting in the SW image. The original idea of the SWI technique was to further suppress the signal from venous vessels in the brain achieving a higher contrast. Several reports showing the sensitivity of SWI to even weaker susceptibilities have been published [Seh05, Rau05, Seh06, Sed08a, Sed08b]. Due to their paramagnetic property [Oga90b], veins produce similar field inhomogeneities and signal voids as SPIO particles. However, their geometry is usually different. By changing the properties of the phase mask, the tissue surrounding iron oxide particles could be

highlighted against the homogeneous tissue. The algorithm for SPIO particles was tested on an agar phantom containing different concentrations of labeled cells and an ex-vivo bovine liver.

3.4.2 Material and Methods

Field Alterations caused by SPIOs

SPIO particles, in this case Resovist (SHU 555 A, Bayer Schering Pharma AG, Berlin, Germany), consist of a core of ferucarbotran coated with carboxydextran. The average diameter of the iron core is ≈5 nm, the average diameter of the coating is ≈63 nm as stated by the manufacturer. When placed in an external magnetic field, the magnetic moments of the particles generate a strong magnetic field perturbation due to their high susceptibility. The particles lack remanent magnetization when the external magnetic field is terminated, since they can be regarded as thermodynamically independent, single-domain particles [Wan01]. The field perturbation ΔB_z of a magnetic dipole with respect to the z-axis is given by the dipole equation

$$\Delta B_z(r, \Phi) = \frac{p_m}{4\pi r^3}(3cos^2\Phi - 1)$$

Here, p_m is the magnetic moment of the particle, r is the distance from the dipole center, and Φ is the angle with respect to the main field parallel to the z-axis. In gradient echo imaging, this field perturbation leads to signal voids in the area of the dipole field, due to a shortened T_2^*-relaxation time. In spin echo imaging, the effect of the dipole field of larger particle agglomerations, based on the distortions in spatial encoding, is visible but not massive.

Common Approaches to SWI

The original SWI method proposed by Haacke and Reichenbach [Haa04] was designed to improve contrast between veins and tissue in the human brain. The basis is a 3D flow-compensated gradient echo sequence. In order to generate the SW image, both the magnitude and the phase image are utilized. Therefore, the phase image is high-pass filtered [Wan00] to remove the low spatial frequency components of the background field. For suppression of the signal from the veins, a phase mask with following

characteristic is created:

$$\begin{aligned} \phi(x) < 0 \quad &\rightarrow \quad f(x) = \frac{\phi(x) + \pi}{\pi} \\ \phi(x) \geqq 0 \quad &\rightarrow \quad f(x) = 1 \end{aligned}$$

Here, $\phi(x)$ is the phase of a certain pixel $(-\pi, \pi]$ and m is the number of multiplications. Pixels with a phase of $-\pi$ will be completely suppressed and those with a value between $-\pi$ and zero will be only partly suppressed. This phase mask $f(x)$ then takes on values between zero and unity. The magnitude image $\rho(x)$ is then multiplied several times m by the phase mask $f(x)$ to create the SW image

$$\rho(x)_{SWI} = f^m(x)\rho(x)$$

SWI of SPIO Effects with Positive Contrast

A straightforward method for the generation of positive contrast in the vicinity of susceptibility variations is to replace the original phase mask of the SWI algorithm. The objective of the new phase mask is to suppress the homogeneous spins with phase values around zero while conserving intensities of pixels with a certain phase value in the resulting image. Three phase masks with different shapes were implemented. The characteristics of the phase masks are described with the following parameters:

- Δ: the upper threshold defines the range of the partly suppressed phase values. Absolute phase values larger than Δ are given the mask value 1.
- δ: the lower threshold defines the range of completely suppressed phase values. Absolute phase values below δ are given the mask value 0.
- m: number of phase mask multiplications.

The three implemented phase masks were:

- Step Function mask:

$$\begin{aligned} |\phi(x)| \geqq \Delta \quad &\rightarrow \quad f(x) = 1 \\ |\phi(x)| < \delta \quad &\rightarrow \quad f(x) = 0 \\ \delta < |\phi(x)| < \Delta \quad &\rightarrow \quad \left(\frac{-1}{\delta - \Delta}(|\phi(x)| - \Delta) + 1 \right)^m \end{aligned}$$

The step function mask completely suppresses all phase values smaller than the lower threshold, giving them the mask value 0. Phase values larger than the upper threshold are given the mask value 1, leaving the magnitude value in the resulting image unchanged. Phase values between the upper and the lower threshold gain a linear dependent mask value between 1 and 0 for m=1.

- V-shaped mask:

$$\begin{aligned} |\phi(x)| \geqq \Delta &\rightarrow f(x) = 1 \\ |\phi(x)| < \delta &\rightarrow f(x) = \left| \frac{\phi(x)}{\Delta} \right|^m \end{aligned}$$

The V-shaped mask completely suppresses only the phases with the value 0. Between 0 and Δ, the function rises linearly with the phase for m=1. Phase values above the upper threshold gain the mask value 1, so that the magnitude in the resulting image is unchanged. The V-shaped mask is a special case of the step function mask for δ=0.

- Hanning mask:

$$\begin{aligned} |\phi(x)| \geqq &\rightarrow f(x) = 1 \\ |\phi(x)| < \Delta &\rightarrow f(x) = \left(1 - \frac{1}{2} \left(1 + cos \left(\frac{2\pi |\phi(x)|)}{2\Delta} \right) \right) \right)^m \end{aligned}$$

The Hanning mask leaves all pixels with a phase value above the upper threshold unchanged. Between 0 and Δ, the phase values are weighted with a cosine function, ranging from 1 near the upper threshold to complete suppression at the phase value 0.

The characteristics of the phase masks can be changed by multiplying the magnitude image more than once by the specific phase mask. Then the mask values do not rise linearly, in the case of the step function and the V-shaped mask or with a cosine function, in case of the Hanning mask, but rise according to the power of m of the particular function. This results in a broader suppression of phase values around the homogeneous phase 0. By taking the absolute values of the phases, all three masks are symmetrical to the phase value 0, so both the negative parts as well as the positive parts of the dipole field around the susceptibilities participate in the resulting magnitude image.

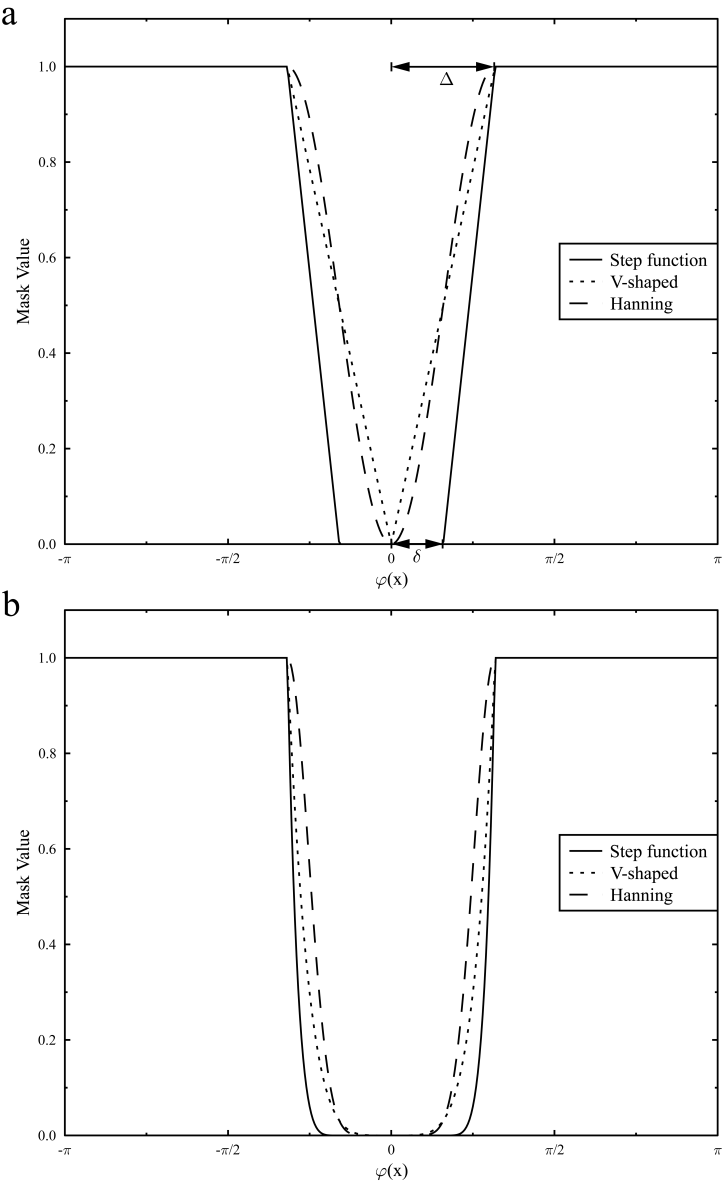

Figure 3.1: The three implemented phase masks for Δ=1 and δ=0.5 with m=1 (a) and m=5 (b). The suppressed area around the homogeneous phase $\phi(x)$=0 increases with m. The phase values range from $-\pi$ to π.

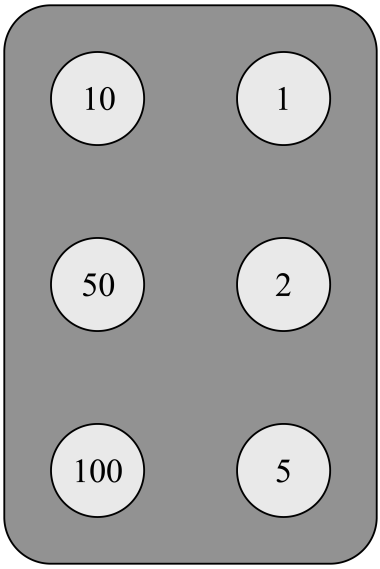

Figure 3.2: Qualitative sketch of the distribution of the labeled cells in the agar phantom. Cell numbers are in thousands. The cells were inserted in wells with a volume of 20 µL. Iron content per cell was 37 pg.

Cell Phantom

SPIO-labeled human melanoma cells (SK-Mel28, average cell size ≈20 µm) were used as a cell model. The cells were cultured in RPMI Medium (Invitrogen, Karlsruhe, Germany) supplemented with 10% fetal bovine serum and 1% penicilin-streptomycin at 37°C in a humidified atmosphere of 5% CO2 and 95% air in an incubator (Heraeus, Hanau, Germany). The cells were grown in flat-bottom flasks and labeled by incubation with Resovist. The incubation time was 18 h, and the iron concentration in the culture medium was 200 µg Fe per mL. Different numbers of approximately $1 \cdot 10^3$, $2 \cdot 10^3$, $5 \cdot 10^3$, $1 \cdot 10^4$, $5 \cdot 10^4$, and $1 \cdot 10^5$ SPIO-labeled cells were homogeneously suspended in 20 µL of agar gel (volume concentration agar per buffer (PBS, Invitrogen) 1% (Sigma-Aldrich, Taufkirchen, Germany)). Assuming a homogeneous distribution of cells throughout the samples, the preparation resulted in a concentration of N=50, 100, 250, 500, 1000, and 2000 SPIO-labeled cells per µL of gel. The arrangement of the different cell concentrations in the agar phantom is shown in Fig.3.2.

Bovine Liver

A 10 cm x 20 cm part of an ex-vivo bovine liver was used as a tissue model to demonstrate the feasibility of the post-processing algorithm for further applications in vivo. A capillary with length 32 mm and volume 9 µL was filled with 0.3 µL Resovist (≈1 mm). The remaining volume of the capillary was filled with water. The resulting SPIO-water solution in the capillary had an iron concentration of ≈0.9 µg per µL. The capillary was sealed at both ends to prevent the solution from leaving the capillary during the measurements. The capillary was then inserted in the liver.

Measurements

All measurements were performed on a 1.5 T Siemens whole body system Vision Sonata (Siemens, Erlangen, Germany). The agar gel phantom and the bovine liver were placed in the extremity coil of the manufacturer. The T_1-relaxation time of the agar gel was found out to be 2000 ms. Imaging parameters were: TR=70 ms, flip angle=14°, field of view=128 x 128, matrix size=256 x 256, slice thickness=3 mm, averages=10, acquisition time (TA)=3 min. For the imaging of the liver, the flip angle was increased to 30°, due to the shorter T_1-relaxation time of about 400 ms.
BW and TE were variable sequence parameters for the measurements. TE was varied in the range of 20-50 ms in steps of 15 ms. BW was varied from 30 Hz/Px over 100 Hz/Px to 200 Hz/Px, where 30 Hz/PX was the lower hard limit for the conventional gradient echo sequence. An additional dataset with TE=10 ms and BW=100 Hz/Px was acquired for the bovine liver measurements in order to match clinically used TEs.
The post-processing parameters of the phase masks for the acquired images were varied as follows: Δ=0.02-0.26 in steps of 0.08 for the agar phantom and Δ=0.5-2 in steps of 0.5 for the bovine liver as well as m=1, 3, 5, and 10. For the calculations of the relative contrast, the threshold Δ was varied from 0 to 0.1 in steps of 0.01 and the number of multiplications m from 0 to 10 in steps of 1.
For calculation of T_2^*-maps comparable to results from SWI imaging, a multi gradient echo sequence with 12 monopolar echoes and BW=300 Hz/Px was applied. TEs were TE1=5.4 ms and δTE=5.6 ms for all following echoes. All other parameters, including TA, were the same as for the SWI gradient echo acquisitions.

Quantitative Assessment of Pixels with Positive Contrast

The number of positive contrast pixels versus cell concentration was counted, dependent on sequence parameters, TE and BW, and mask parameters, Δ and m for the V-shaped mask. For the determination of pixels with positive contrast, the threshold was adjusted to the mean gray value plus two times standard deviation (as measured in a homogeneous region of interest (ROI) without iron labeling). The number of pixels with higher intensities in this ROI, divided by its size, was taken as a correction factor, representing the percentage of statistical error. For each cell concentration, the number of positive contrast pixels (with intensity above the threshold, subtracted by the correction factor) was evaluated. The total number of positive pixels inside and outside the well was counted.

3.4.3 Results

3.4.3.1 In-vitro Agar Phantom

Sequence Parameter Dependence

The phase difference between the spins near SPIO particles and the homogeneous parts is a linear function of TE. The induced dipole field of a small particle concentration generates lower frequency alterations in the tissue. In this case, an evaluable phase difference requires a long TE. By increasing TE, the dimension of the highlighted areas near the particles increases as well. On the other hand, the short T_2^*-relaxation time at the site of the particles leads to a decreased intensity in the resulting image. The larger concentrations are then depicted as dipole shaped rings.
In Fig.3.3 (top row), the influence of TE on the positive contrast is demonstrated for the agar phantom. The V-shaped mask was used for post-processing to visualize the dependence of the sequence parameters. TE is increased from 20 ms (a) to 50 ms (c) in steps of 15 ms. At TE=20 ms, the smallest concentration of SPIO labeled cells is not visible. By increasing TE, this concentration becomes slightly visible as bright spots at TE=35 ms (b). At TE=50 ms (c), all cell concentrations have achieved a clearly visible grayscale value. At all TEs, the homogeneous agar is suppressed. The parameters for these images were Δ=0.1 and m=5 and BW=30 Hz/Px. For comparison, a corresponding T_2^*-map is shown in Fig.3.3(d). At the site of the higher concentrations, i.e., more than 5000

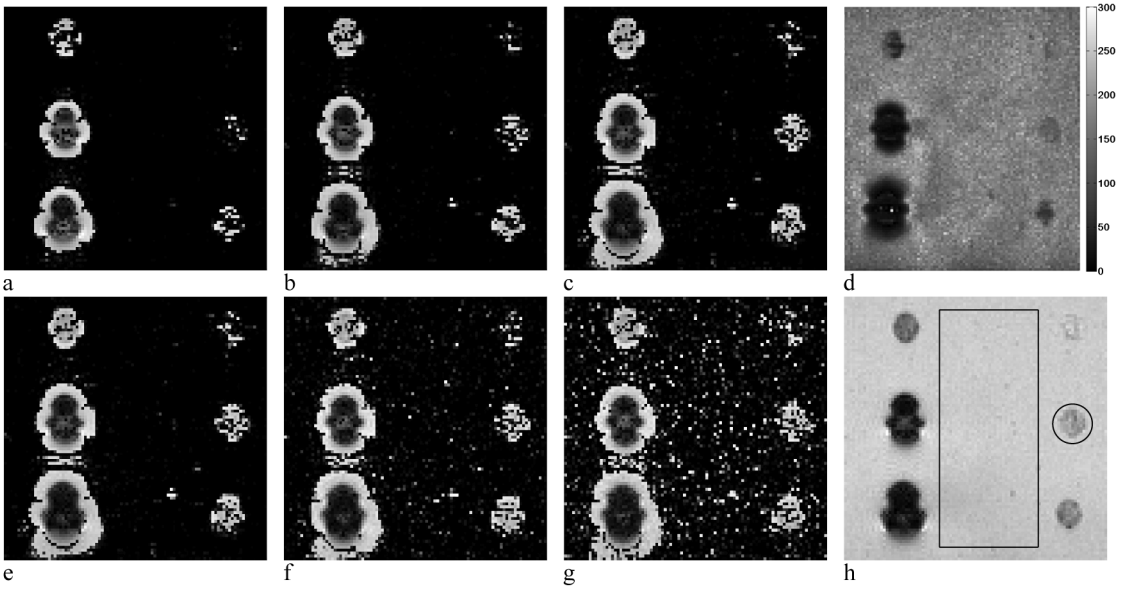

Figure 3.3: Sequence parameter dependence of the positive contrast. For TE=20 ms (a), the lowest cell concentration is not visible. By increasing TE to 35 ms (b) all concentrations give a bright grayscale value, which becomes more apparent at TE=50 ms (c). A higher BW results in an increase of noise in the image. A corresponding T_2^*-map is given in (d). At BW=30 Hz/Px (e) the homogeneous agar is suppressed, at BW=100 Hz/Px (f) the noise arises as bright spots, and reduces the contrast between the smallest concentration and the agar noticeably at BW=200 Hz/Px (g). The magnitude image of the agar phantom is shown in (h) for TE=50 ms and BW=30 Hz/Px. The box depicts the ROI for the homogeneous agar, the circle the ROI for the 2000 cells.

cells, the relaxation times are significantly reduced. On the other hand, for the two lowest SPIO concentrations, T_2^* decrease is relatively small, and a clear identification of particles is difficult, even in a homogeneous agar medium.
BW is directly linked to the noise in an MR image. A narrow BW leads to a low noise signal, whereas a high BW results in a significant noise signal. A noise pixel with a large phase offset and additionally a relatively high magnitude will therefore be visible as a bright spot in the resulting image. In Fig.3.3 (bottom row), the effect of an increased noise through higher BWs is shown. BW is 30 Hz/Px (e), 100 Hz/Px (f), and 200 Hz/Px (g). At the narrowest BW in (e), the homogeneous part of the agar is completely free of bright spots. These arise at BW=100 Hz/Px in (f) and lead to a decreased contrast between the labeled cells and the agar in (g) at 200 Hz/Px. Here, TE was 50 ms, the mask parameters were Δ=0.1 and m=5. A regular magnitude image of the agar phantom with BW=30 Hz/Px and TE=50 ms is shown in figure part (h).

Mask Parameter Dependence

A small number of multiplications results in an incomplete suppression of the phase values between 0 and Δ, and δ and Δ for the step function. With an increase of multiplications, the suppressed area of phases around the phase value 0 is broadened. The phase values are then multiplied by the power m of the particular function. For a boundary value of m toward infinite, all three masks gain the characteristic of a boxcar function, leading to a complete suppression of phases between 0 and Δ.
The dependence of the positive contrast on m for the single masks is shown in Fig.3.4 (step function mask=top, V-shaped mask=middle, Hanning mask=bottom). The number of multiplications is: m=1 (a), m=3 (b), m=5 (c), and m=10 (d), with Δ=0.1 and δ=0.02. Since the grayscale values from the homogeneous parts of the sample are relatively high in (a), the image shows no positive contrast around the labeled cells. For m=3, the homogeneous parts are mostly suppressed leading to an acceptable positive contrast. In (c), the bright spots in the homogeneous agar have completely vanished and the contrast is best possible. However, by choosing m too high, significant parts around the SPIO particles are suppressed as well (d).
The threshold Δ specifies the phase value where the mask function reaches 1. Phase values above Δ have the mask value 1, phase values below Δ

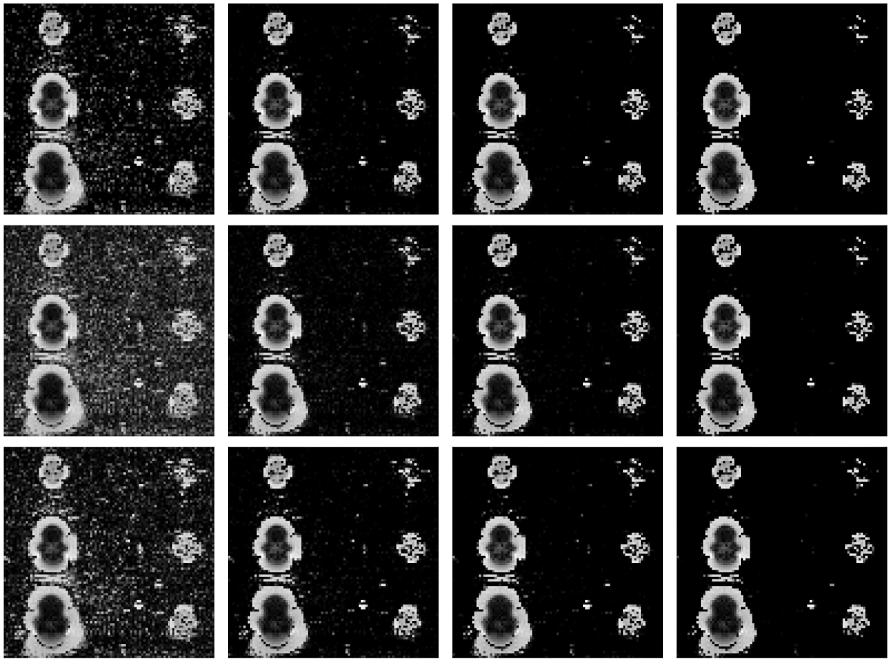

Figure 3.4: The dependence of the number of multiplications for the step function mask (top row) the V-shaped mask (middle row) and the Hanning mask (bottom row) is shown, for m=1 (a), m=3 (b), m=5 (c), and m=10 (d). The differences between the masks can be seen best for the smallest concentration. The V-shaped and the Hanning mask generate higher grayscale values, but the step function mask better suppresses the homogeneous background.

are partly or completely suppressed, depending on the function and the number of multiplications. In Fig.3.5, the signal dependence concerning the threshold Δ for the single masks is demonstrated with m=5. For the step function mask, a lower threshold of δ=0.02 was used. Choosing Δ too small leads to an increase of highlighted pixels in the homogeneous parts and therefore to a decrease in contrast. However, a high value of Δ results in a suppression of pixels around the smaller concentrations of labeled cells. In Fig.3.5(a), the threshold Δ is 0.02 increasing in (b) to 0.1, in (c) to 0.18, and finally to 0.26 in (d). For Δ=0.02 (a) the pixels of the homogeneous parts are not suppressed, leading to a negative contrast around the SPIOs. In (b), the homogeneous agar is almost completely dark and in the vicinity of the different cell concentrations pixels are highlighted, resulting in a noticeable positive contrast. By increasing Δ in (c) and (d), the suppression of the homogeneous agar is improved, however, the bright parts around the smallest concentration of SPIOs vanish as well.
The mean intensity values around the 2000 cells per 20 µL and the homogeneous agar gel for the different phase masks are shown in Fig.3.6. By increasing m, the values decrease to a limit defined by the boxcar function for m toward infinite. The intensity of the agar reaches the minimum of 0 for m=5. Here, the intensity values around the cells for the three different masks are in the range of 1000. The Hanning mask generates the highest values for both the cells and the agar, the step function the lowest. The intensity values for the V-shaped mask lie between. A similar result can be seen with an increase of the threshold, however, the limit for the values for Δ toward π is 0. The intensity values for the homogeneous agar are completely suppressed for Δ=0.1. Thus, increasing the threshold above 0.1 leads to a decreased contrast in the resulting image.
The dependence of the relative contrast

$$C_{rel} = \frac{S_C - S_A}{S_C + S_A}$$

for Δ ranging from 0.01 to 0.1 in steps of 0.01 (with m=5, δ=0.02) and for m=1 to 10 in steps of 1 (with Δ=0.1, δ=0.02) are shown in Fig.3.7. S_C is the intensity around the cell concentrations with 2000 cells and S_A the intensity of the homogeneous agar. The sequence parameters were TE=50 ms and BW=30 Hz/Px. The diagram reflects what can be seen in Fig.3.4 and Fig.3.5: a best possible contrast of 1 is achieved for Δ=0.1 and m=5, with marginal differences for the single masks.

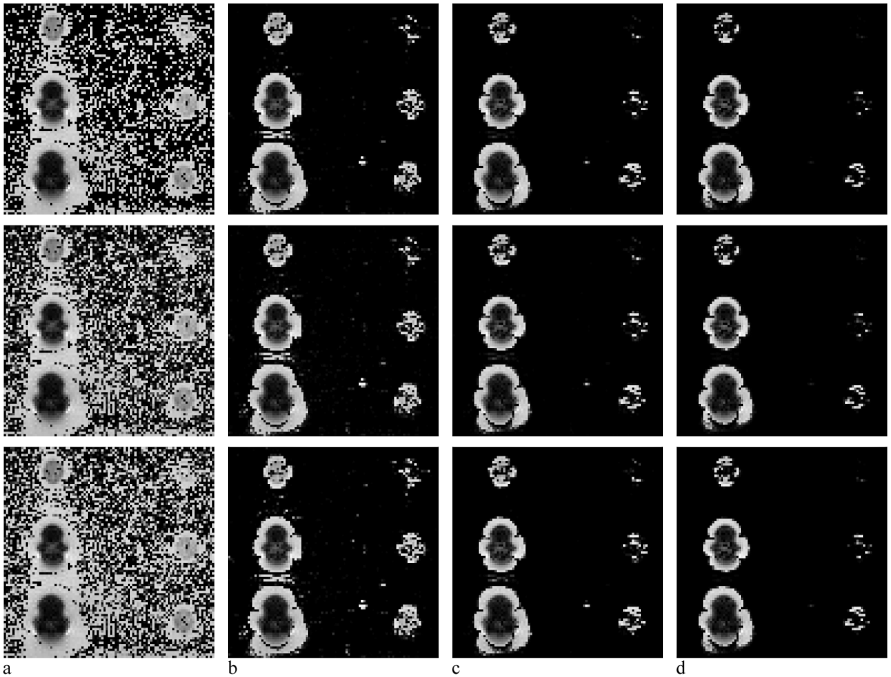

Figure 3.5: The dependence of the threshold for the step function mask with δ=0.02 (top row) the V-shaped mask (middle row) and the Hanning mask (bottom row) is shown, for Δ=0.02 (a), Δ=0.1 (b), Δ=0.18 (c), and Δ=0.26 (d). In (a), the threshold is chosen so small, that no positive contrast is generated. In (b), the homogeneous part is completely suppressed for the step function mask and almost complete for the V-shaped and Hanning mask. Further increase of the threshold leads to partly or completely suppression of the smaller concentrations (c) and (d).

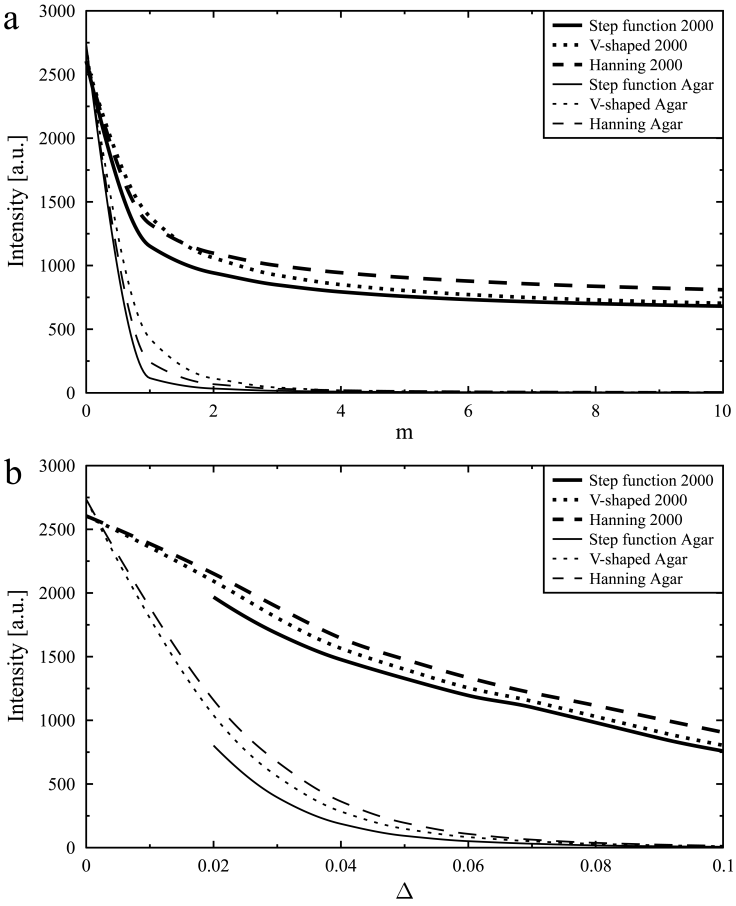

Figure 3.6: Mean intensity values of a ROI around the 2000 cells and the homogeneous agar, for increasing m (a) and increasing Δ (b). Complete suppression of the background is reached for m=5 and Δ=0.1.

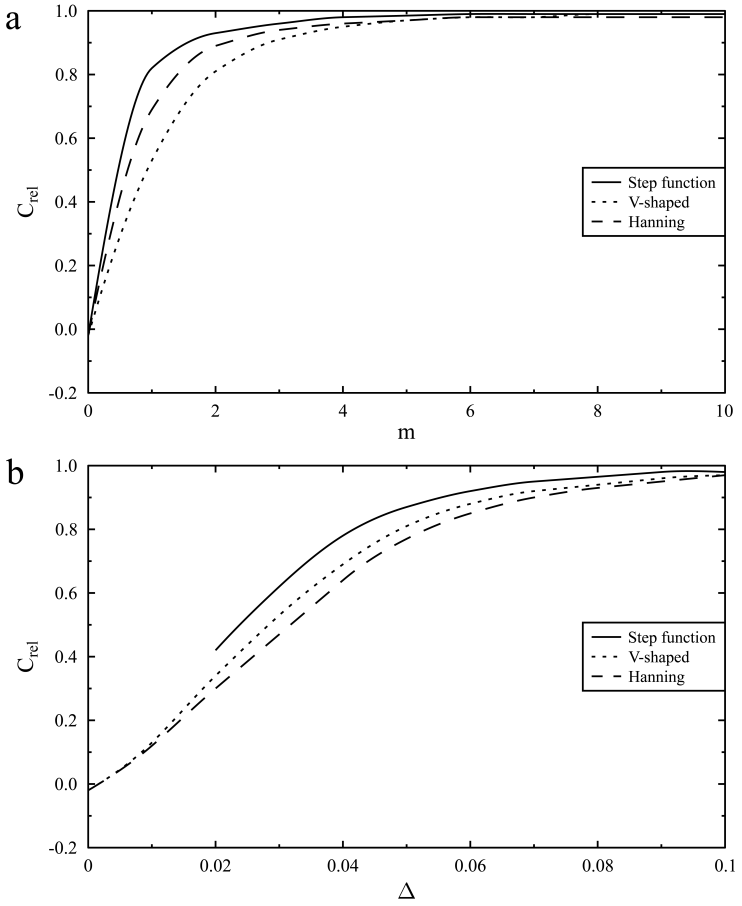

Figure 3.7: Calculated contrast between the 2000 cells and the background for variable m (a) and variable Δ (b). The step function mask reaches maximum contrast C_{rel}=1 for slightly lower values of m and Δ in comparison to the V-shaped and the Hanning mask.

Number of Pixels with Positive Contrast versus Cell Concentration

By increasing parameters m and Δ, Fig.3.8(a, b), the number of positive pixels rises up to a maximum, which is reached later for larger cell concentrations. The number of detected pixels remains constant for further increasing m and Δ, however, the intensity values decrease significantly. The maximum number of positive pixels for all concentrations is reached for values of m=5 and Δ=0.13, which are 44, 90, 113, 127, 401, and 610 pixels for concentrations of 1000, 2000, 5000, 10000, 50000, and 100000 cells per 20 µL, with an area of the wells of approximately 100 pixels. The sequence parameters were TE=50 ms and BW=30 Hz/Px.
Fig.3.8(c, d) show the effects of variable TE (BW=30 Hz/Px) and BW (TE=50 ms) on the number of positive pixels (with fixed parameters m=5 and Δ=0.1). For longer TEs, the number of detected pixels increases, in particular for lower concentrations. Here, the gain in positive pixels is up to 30%, comparing the values for TE=20 ms with TE=50 ms. For the higher concentrations, the relative gain is smaller, due to pronounced signal dephasing at the site of the wells. Fig.3.8(d) demonstrates the benefit of a narrow BW for the detection of positive contrast pixels. The statistical noise increases for higher BWs, so that the detected number of pixels is decreased to 40% for the lowest concentration, if BW is increased from 30 Hz/Px to 200 Hz/Px.

3.4.3.2 Ex-vivo Bovine Liver

Sequence Parameter Dependence

In Fig.3.9, the dependence of increasing TE and BW on the positive contrast in the bovine liver are shown. The sequence parameters were TE=20 ms for different BWs, and BW=100 Hz/Px for different TEs. By increasing TE from 10 ms in (a) to 20 ms in (b) to 35 in (c) and 50 ms (d), the dimension of the highlighted area increases. Since the liver is an ex-vivo model, additional signal from air inclusions in the tissue and especially in the blood vessels arise as positive contrast values for higher TEs. The intensity around the capillary is decreasing noticeably with increasing TE. Since the liver has a much shorter T_2^*-value than the agar phantom, a TE of 50 ms is too long to get a satisfactory signal amplitude in the magnitude image and therefore a high grayscale value in the SW image. However, the effects of the Resovist loaded capillary are clearly visible at shorter TEs

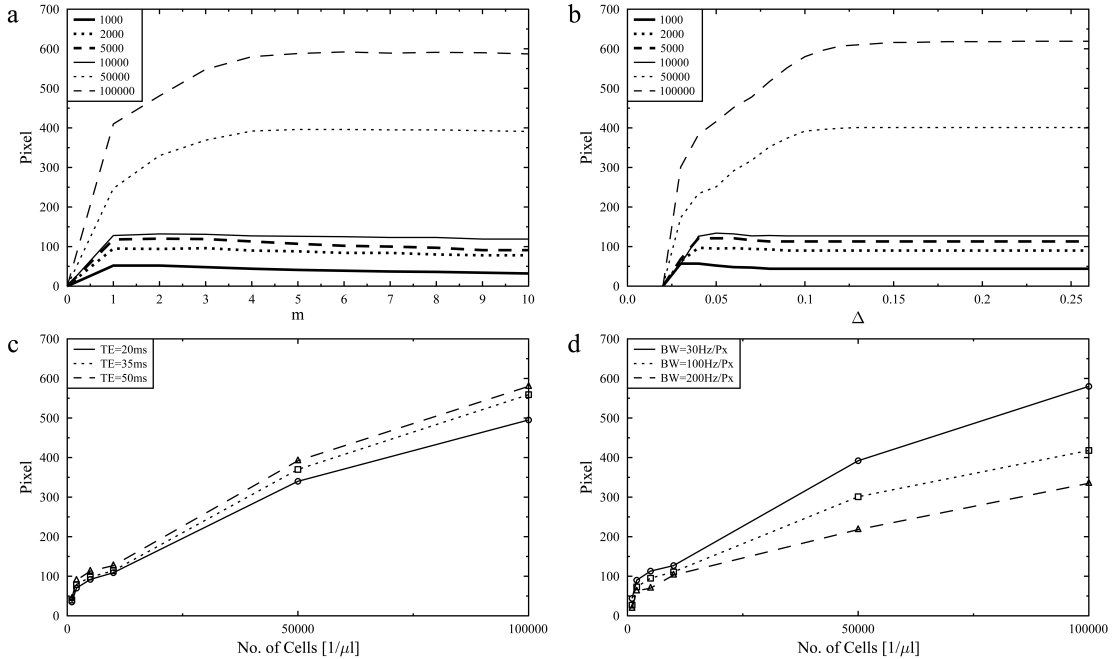

Figure 3.8: Number of positive contrast pixels detected for variation of m (a), and Δ (b) for TE=50 ms and BW=30 Hz/Px, and measurements with different TEs (c) and BWs (d) for m=5 and Δ=0.1.

and distinguishable from the suppressed homogeneous tissue.
The influence of BW (e-g) in the liver images shows similar results as in the agar phantom. An increased noise uptake for higher BWs in the homogeneous tissue is visible. The mask parameters for the V-shaped mask were Δ=0.2 and m=5. In addition, a magnitude image of the liver for TE=20 ms and BW=30 Hz/Px is shown in (h). In the positive contrast images, the SPIO loaded capillary could be clearly distinguished from the homogeneous tissue and from the air inclusions, whereas in the magnitude image the capillary can hardly be found.

Mask Parameter Dependence

The dependence of the positive contrast on the mask parameters Δ and m for the V-shaped mask is demonstrated in Fig.3.10. The threshold was varied from 0.5 to 2 in steps of 0.5 (with m=5) and the number of multiplications was varied for m=1, 3, 5, and 10 (with Δ=1). The sequence parameters were TE=10 ms and BW=100 Hz/Px. The positive contrast increases noticeably from m=1 (a) to m=5 (c) and remains mostly unchanged for a higher number of multiplications. By increasing the threshold value Δ, the intensity of the homogeneous tissue decreases. However, even for a threshold of 2, some unwanted bright spots are visible. These spots arise again from air inclusions in the tissue. By further increasing the threshold, most air inclusions are removed in the resulting image but then significant parts of the capillary vanish as well.

3.4.4 Discussion

The efficiency of suppressing the homogeneous signal while achieving high grayscale values around the SPIO particles is shown. All three mask functions show a good potential for positive contrast imaging. The Hanning mask shows the highest grayscale values around the SPIO particles, but it also leads to the highest values for the homogeneous parts, through incomplete suppression. The V-shaped mask has lower values around the cells, but it suppresses the homogeneous parts slightly better. The best suppression is achieved with the step function mask, however, it has also the lowest intensity around the labeled cells. The relative contrast for all three mask functions is 1 for best possible chosen mask parameters. For further applications in vivo, an incomplete suppression of the homogeneous background could be necessary. With a careful adjustment of the mask

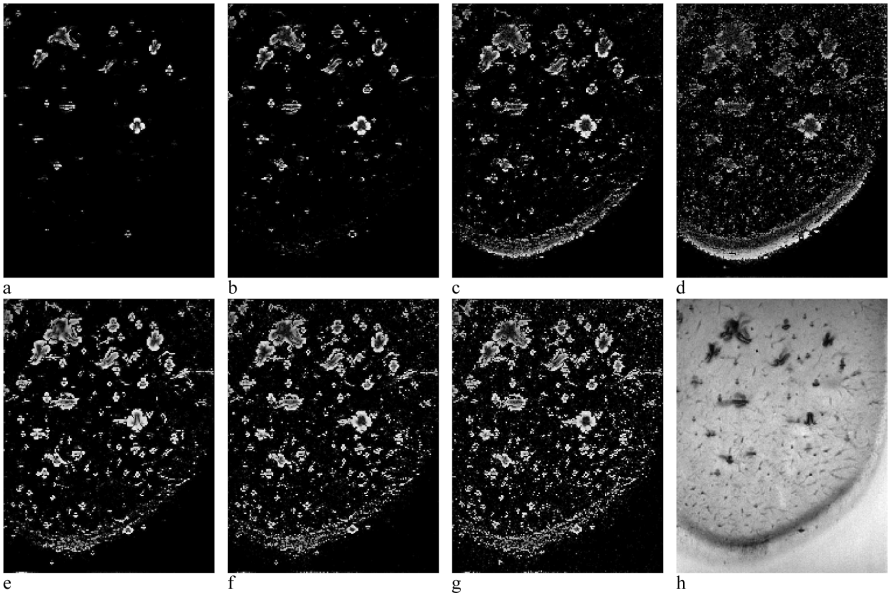

Figure 3.9: Images of the bovine liver acquired with BW=100 Hz/Px and TE=10 ms (a), 20 ms (b), 35 ms (c), and 50 ms (d). Mask parameters for the V-shaped mask were Δ=0.5 and m=5. With increasing TE the contrast between the capillary and the background decreases. Dependence of the contrast on the BW is shown for BW=30 Hz/Px (e), 100 Hz/Px (f), and 200 Hz/Px (g) with TE=20 ms and Δ=0.2 and m=5. In the magnitude image (TE=20 ms, BW=30 Hz/Px) of the bovine liver (h), the capillary is not distinguishable from the air inclusions.

Figure 3.10: Images of the bovine liver showing the mask parameter dependence with the V-shaped mask for TE=20 ms and BW=30 Hz/Px. In images (a-d), the threshold Δ is increased from 0.5 to 2 in steps of 0.5 with m=5. The number of multiplications m is increased according to m=1 (e), m=3 (f), m=5 (g), and m=10 (h) with Δ=1.

parameters not only the highlighted SPIO particles could be seen, but also parts of the anatomy, which leads to an advanced localization of the cells. The relative contrast between labeled cells and the homogeneous agar areas, and between the SPIO loaded capillary and the liver tissue, respectively, depends on two sequence parameters, TE and BW, and two mask parameters, the threshold and the number of multiplications. By choosing these parameters suitable for the measured object, the relative contrast can be maximized. This was demonstrated by the agar-phantom and the ex-vivo bovine liver. For positive contrast imaging of other objects or subjects, these parameters have to be chosen appropriate to the situation. Here, all sequences were tested with a minimum TE of 20 ms in order to compare the results to each other. This was the shortest TE achievable for a BW=30 Hz/Px. With slightly higher BWs, e.g., 100 Hz/Px the minimum TE ≈7 ms.

An important aspect of this method is its relative simplicity. Where other positive contrast techniques use additional saturation or excitation pulses or other modifications of the sequence, which may have a negative influence on TA or imaging quality, the presented method is based on a conventional gradient echo sequence. Additionally, whereas frequency selective saturation or excitation techniques require a precise adjustment of the water proton frequency, the SWI based technique is insensitive toward an inaccurate shim or inhomogeneities of the magnetic field. This is accomplished by the phase filter procedure, which removes the low spatial frequency components, independent of the absolute frequency. Furthermore, the imaging parameters for the gradient echo sequence can be chosen without any restriction. However, a narrow BW and a longer TE are recommended. An advantage of this technique in comparison to off-resonance excitation and incomplete rewinder gradients is that both parts of the SPIO signal, the negative and the positive dipole distortions, can be measured simultaneously. The reason for that is the symmetrical phase mask. This leads to increased grayscale values around the SPIO labeled cells.

All measurements were performed with a matrix size of 256 and a field of view of 128 pixel, resulting in a resolution of 0.5 mm x 0.5 mm. This seemed to be a good compromise between structural resolution and noise uptake due to larger matrix size. In higher resolution images, the larger matrix size would act as an additional dwell of noise in the homogeneous tissues.

Multi-echo gradient echo images were recorded and corresponding T_2^*-maps were derived. Those T_2^*-maps showed a clear identification of high SPIO

concentrations, whereas small concentrations were hardly detected, since a high BW was necessary for T_2^*-mapping. The high BW in multi-echo sequences led to relatively noisy T_2^*-maps, and the variation of T_2^*-values in homogeneous areas is larger than the effect of a reduced relaxation time due to small particle concentrations. By comparing the T_2^*-map with the resulting images from the modified SWI technique, the latter shows improved identification of particles. Furthermore, the SWI based technique allows improved detection of single pixels with positive contrast, as demonstrated in Fig.3.3(a-c) for a large range of TEs. In this series of images, the same pixels are constantly detected with positive contrast.

3.4.4.1 Limitations

In theory, even very small phase differences between SPIO particles and homogeneous tissue could be distinguished with the algorithm of the SWI method. Practically, the limit for this technique is defined by the inhomogeneities of the tissues around the particles as well as the inhomogeneity of the magnetic field and the excitation profile of the coil.
In the agar phantom, the threshold was 0.1 and the well with a concentration of 1000 cells per 20 µL could be visualized with a complete suppression of the homogeneous parts. However, in the bovine liver, the phase offset in the homogeneous parts of the tissue was much larger, so that the threshold had to be increased to 0.5 for a complete suppression of the homogeneous tissue. By comparing the iron content in the capillary with the iron content in the agar phantom, the whole capillary has an iron equivalent of about 230000 cells. With a slice thickness of 3 mm for the acquired images of the liver, the equivalent number of cells in the slice is approximately 23000. However, the dimension of the highlighted area around the capillary gives rise to a significant lower detection limit for this technique.

3.4.4.2 Applicability for in-vivo Imaging

For further application of the proposed SWI based technique in vivo, some points have to be considered: The narrow BW, mandatory for a low noise image, might lead to pronounced chemical shift artifacts between water and fat. This problem can be overcome by increasing BW. Unfortunately this adaptation leads to more noisy images and decreased sensitivity. Frequency selective saturation pulses are not recommended since frequency-shifted signals from tissue in the labeled area are also suppressed. Which strategy is best for in-vivo imaging in respect of sensitivity towards small

particle concentrations, has still to be evaluated for different types of tissue. Regarding the mask parameters Δ=0.25 and m=4 are expected to be suitable start values for complete suppression of homogeneous tissue, as shown by initial tests on volunteers. Cell concentrations between 2000 and 5000 cells per 20 µL should be resolvable. To reduce artificial effects of tissue elements with short T_2^*-values and a high phase dispersion, e.g., connective tissue or air inclusions, a threshold could be defined that eliminates low signal intensities. This threshold would not affect intensities in the area of small SPIO concentrations.

3.4.5 Conclusion

The feasibility of generating positive contrast around iron labeled cells by use of a SWI technique is demonstrated. Different post-processing algorithms were tested for specific conditions, which can be implemented with little effort on the scanner, or on an external PC. The gradient echo sequence has complete variability in all parameters and allows rapid imaging with high sensitivity to small concentrations of SPIO labeled cells. This method was tested on an agar phantom and an ex-vivo bovine liver, but clinical applications for immune- and stem-cell tracking seem promising.

3.5 Positive Contrast with k-space Filtering

3.5.1 Introduction

MRI is a powerful tool to non-invasively monitor the migration of cells labeled with magnetic particles such as SPIOs [Wei97, Zha00, FG03, Hin03, Bul09]. Due to the superparamagnetic character of the iron-oxide particles, a dipole field is generated in their vicinity, when placed in the magnetic field B_0 of an MR scanner [Sch96a]. This field superimposes the relatively homogeneous B_0 field in most tissue types, leading to a shift and a broader distribution of the Larmor frequencies of the proton spins in the affected area, according to the Larmor equation.
In conventional gradient echo images, broadening of the distribution of Larmor frequencies results in reduced effective transverse relaxation times T_2^* of the spins in the vicinity of the particles, visible as signal voids [Bow02, Pin06b]. In cell tracking studies, this negative contrast of the labeled cells is often not distinguishable from tissue with low proton density. An improved visualization of labeled cells can be achieved by utilizing their physical properties to generate positive contrast, thus conserving the signal around the cells, while suppressing the unaffected areas.
In this part, a post-processing technique is introduced, which is based on a straightforward filter algorithm, applied to the raw-data of a gradient echo acquisition. An inverse Hanning filter with variable size is utilized to suppress central parts in k-space, while conserving the outer areas. The application of the filter results in the highlighting of pixels affected by a magnetic field gradient against homogeneous pixels. The image reconstructed from the filtered raw-data is further processed to remove statistical noise, thus increasing contrast. Therefore, a threshold is computed from a ROI in the area of the homogeneous tissue, which cuts off low intensities. The remaining intensities in the resulting image are then the k-space shifted pixels around the labeled cells, represented as areas with positive contrast. The feasibility of the technique is shown by an agar phantom containing different concentrations of magnetically labeled cells and by in-vivo images of the human head in the absence of labeled cells.

3.5.2 Material and Methods

Iron-oxide nanoparticles, placed in an external magnetic field, generate a dipolar magnetic field [Yab94]. The field perturbation ΔB_z of a magnetic

dipole orientated along the z-axis is given by the dipole equation [Sch96a]

$$\Delta B_z(r,\Phi) = \frac{\Delta\chi B_0}{3}\left(\frac{a}{r}\right)^3 (3cos^2\Phi - 1)$$

Here, $\Delta\chi$ is the susceptibility difference between the particle and the surrounding tissue, a the particle radius, r the distance from the particle center, and Φ the angle with respect to the main field B_0 parallel to the z-axis. The dipole field of the particles superimposes the relatively homogeneous B_0 field in native tissue, which leads to shifted Larmor frequencies in the vicinity of the particles according to the Larmor equation

$$\omega_L = \gamma B_{eff}$$

with γ the gyromagnetic ratio and the effective local magnetic field strength B_{eff}. In a magnitude image of a gradient echo sequence, the shifted frequencies and the resulting phase offsets are visible as signal voids, where the degree of extinction is dependent on the distance and the concentration of the nanoparticles [Bow02, Pin06a]. Here, the signal voids cannot be distinguished from native low signal tissue, which makes the magnitude image an inappropriate tool for the uncorrupted detection of SPIO particles. However, in the k-space of a Cartesian sampled gradient echo sequence, the influence of the superimposing dipole field can be directly evaluated. The dipole field generates additional fixed background gradients during data acquisition [Fra88, Rei97], and therefore leads to a positive or negative shift of the echo in k-space. The resulting echo of a region affected by the dipole field is moved from the k-space center, where the homogeneous spins are situated, toward the edges [Pos92], depending on the strength of the dipole field and TE. This effect is a fundamental of gradient echo imaging, therefore an exact derivation can be found in most basic magnetic resonance textbooks [Haa99].

3.5.2.1 Simulation of k-space Shifts

The distribution of the shifted echoes in k-space is illustrated by a qualitative simulation to clarify the feasibility for the application of the inverse Hanning filter. A spherical region with modified susceptibility and a diameter of 1 pixel is placed in the center of a homogeneous background. The magnetic field distortion of the sphere, given by the dipole equation, is calculated for each pixel. The calculated field is used as the input for the phase image, considering Larmor frequency and TE. An image with the

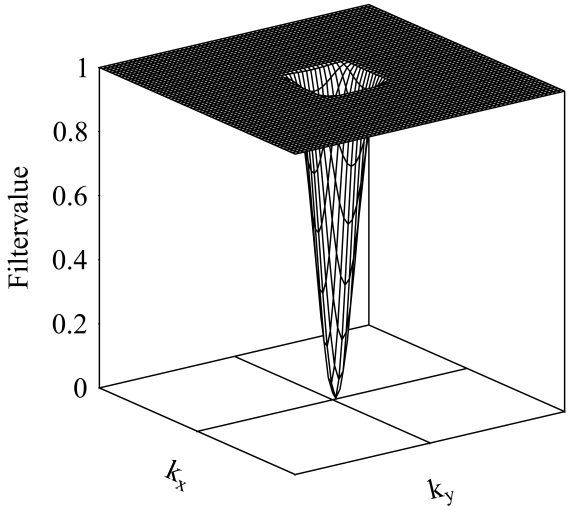

Figure 3.11: Inverse Hanning filter with a size of 40 over a 384 x 384 k-space matrix resulting in a partly suppression of the central 80 x 80 k-space points.

same size as the phase image containing solely the value 1 is taken as the magnitude image, thus neglecting relaxation effects and noise. Magnitude and phase image are utilized to generate a complex image. The simulated k-space is acquired by inverse Fourier transformation of the complex image.

3.5.2.2 Filter Characteristics

The knowledge of the position of the echoes in k-space can be used to create a raw-data filter that suppresses areas with homogeneous magnetic field distribution in the resulting image, while conserving the intensity of the shifted echoes. Two important points have to be kept in mind when using a raw-data filter: First, the filter function has to be smooth to avoid Fourier transformation artifacts in the resulting image. Second, the filter must not completely suppress raw-data points, because this would lead to a decreased resolution. Especially the outer raw-data points have to

be conserved by the filter function, because not only most of the noise is acquired here but also crucial structural information. A filter function that satisfies these conditions is an inverse Hanning filter. The Hanning filter is a cosine-shaped, symmetrical window function, which reaches values between 0 at the edges and 1 in the center. Filter values outside the window are set to 0, thus cutting off the periodical filter function. By subtracting the filter values from unity, the desired properties are achieved. Then, only the central raw-data point that contains solely intensity information is completely suppressed, while the information of all other k-space points is used for the reconstruction of the filtered image, although with a decreased intensity, depending on the size of the filter. Inverse Hanning filtering in k-space is shown in Fig.3.11, for a matrix size of 384 and a window or filter-size of 40. A filter-size of 40 results in a partly suppression of the central 80 x 80 k-space points. The filtered image provides high signal intensities in areas with distinct background gradients and low intensities in magnetically homogeneous parts. However, this image includes two different sources of unwanted intensities: First, the noise situated at the k-space edges, which belongs mostly to the parts of the image, where no tissue is apparent, i.e., statistical noise. The second source is visible in areas with a nearly homogeneous field, resulting from an incomplete suppression of the central area of the k-space.

3.5.2.3 Calculation of the Cut Off Threshold

Since the inverse Hanning filter is not capable of suppressing the homogeneous echoes completely, the remaining intensities in the homogeneous parts of the measured object have to be removed in the filtered magnitude image to improve contrast. This can be done by defining a cut off threshold that sets all intensity values below this threshold to zero while the intensity values above remain unchanged. This operation is feasible, because for an adequate filter-size the remaining intensities in the homogeneous parts of the filtered image are lower than the intensities in the vicinity of the labeled cells.
The first step for automatic determination of a suitable threshold is the sampling of the unfiltered magnitude image and the filtered image in rectangular or quadratic ROIs. Second, the statistical noise, i.e., areas where no tissue is apparent, has to be removed to avoid false detection of the homogeneous ROI in the following steps. Therefore, the mean intensity values of the ROIs in the unfiltered magnitude image are evaluated and

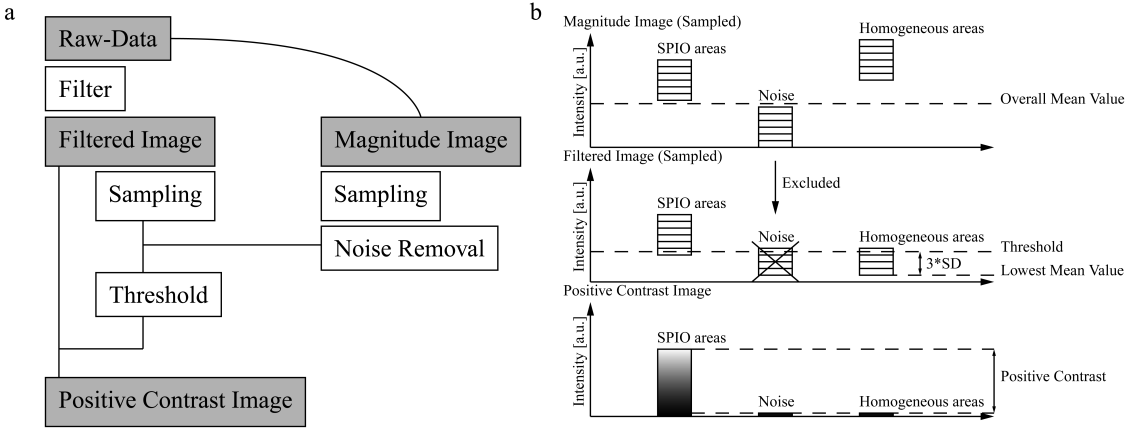

Figure 3.12: Flowchart of the post-processing steps (a). In (b), the intensities of the three interesting fractions in arbitrary units during the post-processing algorithm are qualitatively shown. In the sampled magnitude image, the homogeneous areas have the highest and image parts with statistical noise have the lowest intensities. The regions affected by susceptibility alterations are between. The ROIs containing noise are excluded for further calculation by calculating the overall mean value of the image. Then the lowest intensity in the filtered image can be assigned to the homogeneous ROI. ROIs affected by susceptibility alterations are highlighted in the filtered image. The threshold is calculated from the homogeneous ROI in the filtered image. The final image is then provided with the threshold resulting to an improved contrast between SPIO areas and the homogeneous background.

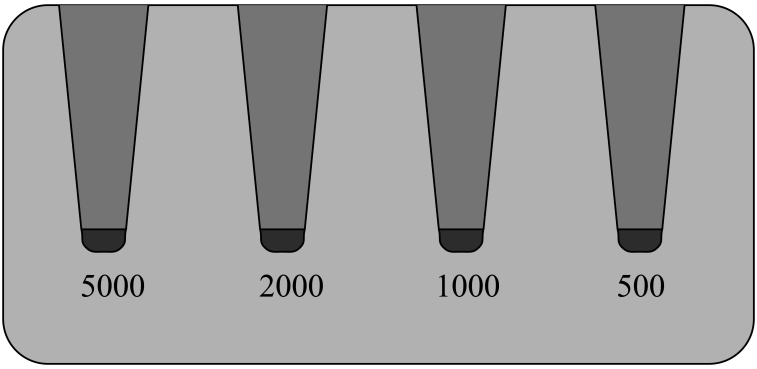

Figure 3.13: Arrangement of the labeled cells in the agar phantom. The cell concentration per µL is the number of cells divided by the volume of the wells which is 20 µL.

compared to a reference defined as the overall mean value of the whole magnitude image. ROIs, containing statistical noise, with mean values lower than the reference are memorized for the next step. The third step is the evaluation of the ROIs in the filtered image. Since the raw-data filter is designed to suppress the homogeneous image parts, these can be assigned to the regions in the filtered image with the lowest intensities after exclusion of the ROIs containing statistical noise. Therefore, the cut off threshold is defined as the lowest mean plus three times standard deviation value found in any of the ROIs, bearing in mind that in a Gaussian distribution, the mean plus three times standard deviation window contains 99.7% of the values. The unsampled filtered image is then provided with the calculated cut off threshold. The removing of all intensity values lower than the threshold, results in an image, where the labeled cells are highlighted and the homogeneous parts are completely suppressed. A flowchart of the complete post-processing steps is given in Fig.3.12. A sampled filtered image as used for the calculation of the threshold is shown in the results section (Fig.3.16b).

3.5.2.4 Cell Preparation and Phantom

SPIO labeled human melanoma cells (SK-Mel28) were used as a cell model. The cells were cultured in RPMI Medium (Invitrogen, Karlsruhe, Germany) supplemented with 10% fetal bovine serum and 1% penicillin-strep-

tomycin at 37°C in a humidified atmosphere of 5% CO2 and 95% air in an incubator (Heraeus, Hanau, Germany). The cells were grown in flat-bottom flasks and labeled by incubation with Resovist. The incubation time in the culture medium was 18 hours at an iron concentration of 200 µg Fe per ml. Cell numbers of $5 \cdot 10^2$, $1 \cdot 10^3$, $2 \cdot 10^3$, and $5 \cdot 10^3$ were homogeneously suspended in 20 µL of a gelatine gel (volume concentration gelatine per buffer (PBS, Invitrogen) 8% (Sigma-Aldrich, Taufkirchen, Germany)). The preparation resulted in a concentration of 25, 50, 100, and 250 SPIO labeled cells per µL of gel with an average iron content per cell of 30.5 pg.
The phantom consisted of a rectangular shaped plastic box (length=12 cm, height=6 cm, width=6 cm) which was filled with agar (volume concentration agar per buffer 1% (Sigma-Aldrich)). A stamp was used to produce conical shaped cavities during the solidification of the agar. The liquid cell-gelatine solution was placed at the bottom of the cavities. The phantom was rested until the cell-gelatine solution had solidified and the cavities finally were filled with agar. The arrangement of the different cell concentrations in the agar phantom is shown in Fig.3.13.

3.5.2.5 Sensitivity

The sensitivity of the algorithm to the detection of labeled cells is evaluated by counting the number of positive detected pixels for different concentrations. Each concentration is encircled with a ROI in any slice of the 3D dataset where labeled cells are apparent. A pixel is counted positive, if the intensity value is higher than the threshold of the regarded slice. The final amount of positive pixels for each concentration of cells is the sum of the positive detected pixels of the single slices. The sensitivity, defined as the ratio between positive pixels and inserted cells per concentration, is evaluated.

3.5.2.6 Experimental Setup and Sequence Parameters

Measurements were performed on a 3 T whole body system Trio (Siemens Healthcare, Erlangen, Germany). The agar gel phantom was placed in the eight-channel knee coil of the manufacturer. Considering the narrow BW, the effect of a fat-saturation pulse on the detection of the labeled cells was assessed. The sequence without the preparation pulse is hereafter referred to as regular (Reg) and the fat-saturated sequence as FS. The imaging parameters of the 3D gradient echo sequences were: TE=20.7 ms and 34.4

ms, TR=58 ms, flip angle=25°, BW=30 Hz/Px, 70 Hz/Px and 100 Hz/Px, resolution 0.25 x 0.25 x 0.5 mm^3, slices=24, averages=1, TA=9 min. Additionally, a 3D gradient echo dataset with TE=21.7 ms was acquired for the calculation of a field map, i.e., ΔTE=1 ms. Head images of a healthy volunteer (no labeled cells) with fat suppression and flow compensation were acquired, by use of a twelve-channel head coil of the manufacturer with parameters: TE=27.6 ms, TR=68, flip angle=25°, BW=30 Hz/Px, resolution 0.5 x 0.5 x 1 mm^3, slices=24, averages=1, TA=10 min.

3.5.3 Results

3.5.3.1 Simulation of k-space Shifts

The simulated k-space images with a k-space size of 384 x 384 are shown in Fig.3.14, for susceptibility differences of the sphere of 5 (a) and 50 (d) times 10^{-6} toward the background and for TE=20.7 ms. For the smaller susceptibility (a), the echoes are concentrated around the center of k-space. Indeed, most of the echoes are situated in the central k-space point. Increasing susceptibility, results in a shift of echoes from the center toward the edges of k-space (d). After application of the Hanning filter (filter-size 40), the central parts of k-space, i.e., the homogeneous magnitude intensities, are suppressed, whereas outer k-space regions are unaffected (b, e). This results in an enhancement of echo shifted intensities against the homogeneous background in the filtered image. Since the echo shift in k-space is dependent on the phase offset, the effect is more dominant for TE=34.4 ms (c, f). The bottom row shows subtracted k-space images for the lower (g) and the larger susceptibility (h), and the difference of the larger and smaller susceptibility (i).

3.5.3.2 Determination of the Optimum Filter-size

The filter-size was increased from 1 to 192, i.e., half of the matrix size, in steps of 1 to determine the optimum size of the raw-data filter. For each filter-size, the filtered magnitude image was reconstructed. In the filtered images, each deposit of labeled cells and a homogeneous area in the agar were encircled with a ROI. The mean values of the five ROIs were evaluated and assigned to the filter-size for TEs of 20.7 ms and 34.4 ms (Fig.3.15). The measure for the optimum filter-size was the evolution of the mean intensity values of the homogeneous ROI in the filtered image. For increasing filter-sizes up to 30 (short TE) or 40 (long TE), a strong

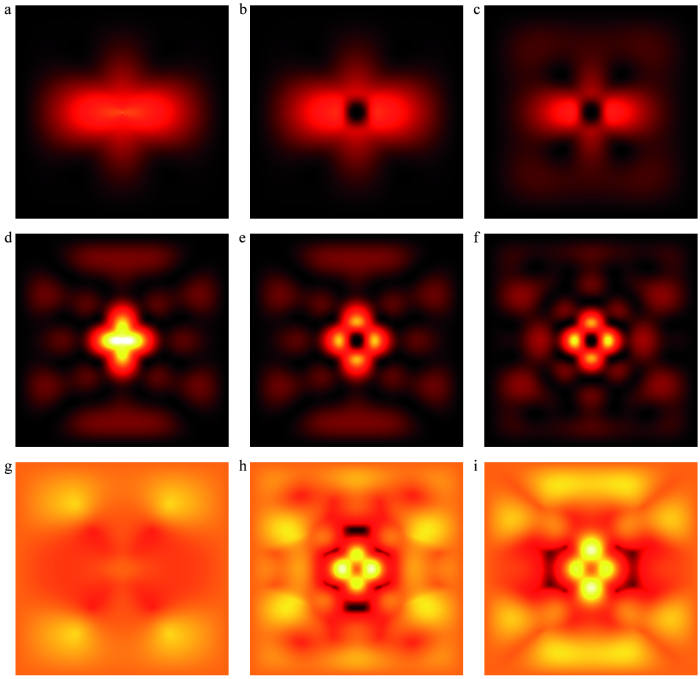

Figure 3.14: Simulated k-spaces for susceptibility differences of 5 (a) and 50 (d) times 10^{-6} toward the background and TE=20.7 ms. A larger difference in susceptibility results in an increased echo shift in k-space. For visualization, high intensities as in the central k-space point are cut off. Application of the Hanning filter suppresses central parts of k-space (b,e). For TE=34.4 ms, the echo shift increases (c,f). Images (a-f) are scaled similar in arbitrary units. Difference images (with filter) are shown for the long TE minus the short TE for susceptibility difference of 5 (g) and 50 (h), and for the subtraction of the larger by the smaller susceptibility (i). Higher susceptibility differences and longer TEs result in larger k-space shifts of the echoes.

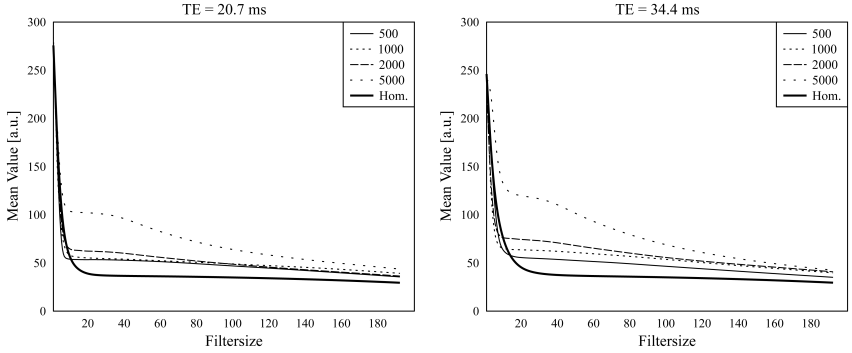

Figure 3.15: Evolution of the mean value of ROIs containing the cell concentrations and in the homogeneous area with increasing filter-size for TE=20.7 ms (left) and TE=34.4 ms (right). The mean values around the cells are higher than the mean value in the homogeneous area. For a filter value above 40, the mean values of the homogeneous areas remain mostly unchanged for both TEs.

decrease of mean values can be observed. They remain mostly unchanged for filter-sizes beyond. At these sizes, the signal of the homogeneous parts of the image is suppressed to the maximum by the filter, depending on TE. For further processing, the filter-size of 40 is used, which shows good suppression for both TEs. The mean values of the ROIs containing the labeled cells and also non-echo shifted pixels, show similar evolution as the homogeneous ROI. However, they tend to cease at a significant higher intensity level, due to the shifted echoes in k-space. The difference of the mean intensities between the ROIs around the labeled cells and the homogeneous ROI offer room for the application of the cut off threshold, where the difference is higher for the longer TE, because of a larger phase offset resulting in a larger echo shift.

3.5.3.3 Determination of the Cut Off Threshold

The magnitude and the filtered image, with the previously determined filter-size of 40, were divided into ROIs each 12 x 12 pixels in size. The magnitude image and the corresponding sampled filtered image are shown in Fig.3.16(a,b). The automatically detected ROI with the lowest mean plus three times standard deviation value is marked by an arrow. This

Figure 3.16: Magnitude image of the phantom (a) and sampled filtered image (b) with the automatically detected ROI used to define the threshold marked. The intensities in the sampled image are scaled to visualize the homogeneous ROI. In (c), the filtered image of the whole phantom is shown. The edges of the box are highlighted, due to the susceptibility difference between air and agar. However, inside the phantom, the homogeneous parts are suppressed.

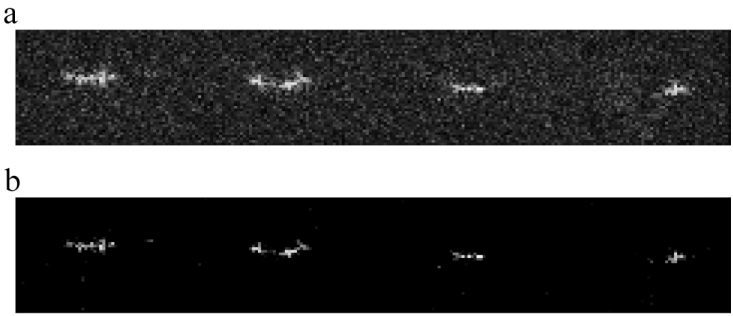

Figure 3.17: Filtered image of one slice of the cell concentrations (5000, 2000, 1000 and 500 cells from left to right) before (a) and after (b) application of the threshold. The threshold removes noise in the homogeneous parts while leaving the intensities of the echo shifted pixels unchanged, thus increasing contrast.

ROI was used to define the value for the cut off threshold. The ROIs containing statistical noise, i.e., outside of the phantom box, were excluded by assigning them the maximum value of 1. In the sampled image, the ROIs in the region of the labeled cells have higher intensity values, due to a higher mean value and standard deviation, compared to the homogeneous parts. The assumption that the homogeneous ROI has the lowest threshold value is proved by the determination of the optimum filter-size, as seen in Fig.3.15. The coefficient of variation of the calculated thresholds for the 24 slices is only 0.029. This shows that the algorithm constantly detects homogeneous areas with similar thresholds values in all slices of the 3D dataset. Additionally, the filtered image of the same slice without the application of the threshold is shown (c). Here, highlighted pixels are also visible at the edges of the box, which are inevitable with susceptibility sensitive post-processing. However, regions not affected by labeled cells are suppressed and not disturbed by low frequent phase oscillations.
The effect of the threshold for the contrast in the filtered image is shown in Fig.3.17. In the filtered image the labeled cells are visible, but the contrast between them and the homogeneous agar is low. After application of the threshold, the homogeneous agar is almost completely removed with only few remaining highlighted pixels. Moreover, the pixels containing labeled cells are not affected by the threshold, which leads to a maximum relative contrast of 1.

3.5.3.4 Number of Positive Detected Pixels and Sensitivity

The same ROIs as for the determination of the filter-size were used to count the number of positive detected pixels generated by the labeled cells for the different BWs and TEs. In every slice, where labeled cells were apparent, the pixels in the appropriate ROI with intensities higher than the threshold were counted. The influence of the fat-saturation pulse on the number of positive pixels is compared with the results of the regular sequence. The sum of positive detected pixels for each concentration is shown in Fig.3.18. The number of positive detected pixels rises almost linearly for the three lower concentrations. In contrast, the number for the largest concentrations is lower than expected with a linear dependency of positive detected pixels with cell concentration. Since a pixel is counted as positive, if its intensity value is higher than the threshold, an increased amount of labeled cells in one pixel will still result in only one positive counted pixel in the absence of a macroscopic dipole field. Thus, the number of detected pixels is limited by the inserted cell volume and the imaging resolution. A longer TE leads to an increase in detected pixels, because of a longer dephasing time of the spins and therefore a larger shift in k-space. Since the noise in the homogeneous areas of the agar is increasing with BW, the calculated threshold rises and pixels with a lower intensity are suppressed in the resulting image, leading to a decreased number of positive detected pixels.
In Table 3.1, the sensitivity as well as the influence of the saturation pulse on the number of positive detected pixels are shown.
The sensitivity is a criterion of how many cells have to be apparent in one pixel to detect the pixel with positive contrast, assuming a homogeneous distribution of labeled cells. It shows that for lower concentrations an average of less than 4 cells per pixel can be detected with a BW=30 Hz/Px and a TE=34.4 ms. For the largest concentration, this value rises to 9 cells per pixel for the same reason mentioned above. Shortening TE to 20.7 ms reduces the sensitivity to 5 cells per pixel and 10 cells per pixel for the largest concentrations, respectively. The number of detectable cells per pixel decreases for all concentrations with higher BWs. For the comparison of the fat-saturated and the regular sequence with TE=20.7 ms, the ratio of positive detected pixels is given. Comparing the number of detected pixels for the regular sequence and the sequence with additional fat-saturation, the saturation pulse lowers the amount of pixels only slightly by about 3-9%.

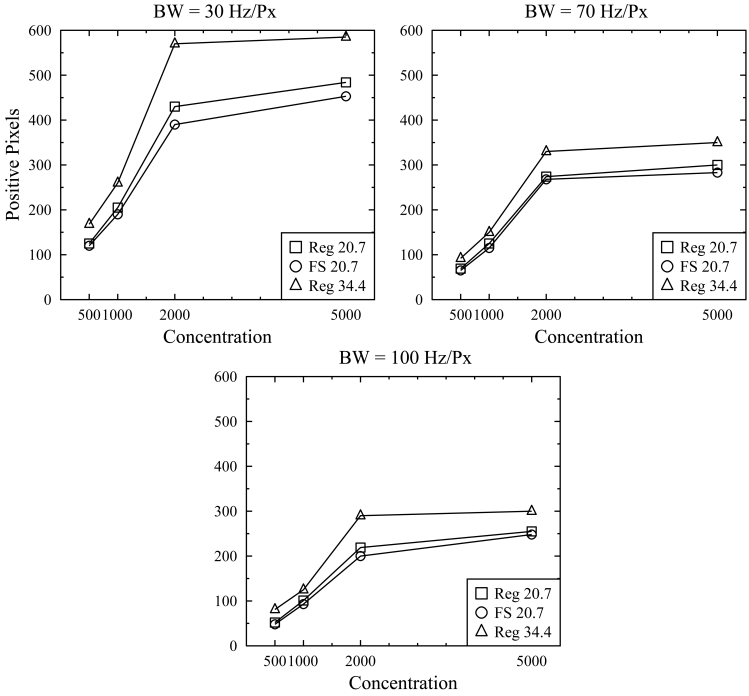

Figure 3.18: Number of positive detected pixels for each concentration and different BWs for the regular (square) and the fat-saturated (circle) sequence with TE=20.7 ms, and for the regular sequence with TE=34.4 ms (triangle). The fat-saturation lowers the number of positive pixels only slightly. The highest number of positive pixels is acquired with BW=30 Hz/Px and TE=34.4 ms.

BW		500	1000	2000	5000
30 Hz/Px	TE 20.7 Reg	4.0	4.9	4.7	10.3
	TE 34.4 Reg	3.0	3.8	3.5	8.5
	TE 20.7 FS	4.2	5.3	5.1	11
	Ratio Reg / FS	0.95%	0.92%	0.92%	0.94%
70 Hz/Px	TE 20.7 Reg	7.2	8.0	7.3	16.7
	TE 34.4 Reg	5.4	6.7	6.1	14.3
	TE 20.7 FS	7.7	8.7	7.5	17.7
	Ratio Reg / FS	0.94%	0.92%	0.97%	0.94%
100 Hz/Px	TE 20.7 Reg	9.6	9.9	9.1	19.6
	TE 34.4 Reg	6.2	8.0	6.9	16.7
	TE 20.7 FS	10.4	10.8	10	20.2
	Ratio Reg / FS	0.92%	0.92%	0.91%	0.97%

Table 3.1: Sensitivity in apparent cells per pixel for positive detection of the pixel (assuming a homogeneous distribution of cells) and ratio of positive detected pixels for the regular and fat-saturated sequence.

3.5.3.5 Maximum Intensity Projection (MIP)

With the generated positive contrast of the labeled cells, a maximum intensity projection over several slices is feasible. In Fig.3.19, MIPs over 10 slices where any concentration is apparent are shown. In the MIP for TE=20.7 ms and BW=30 Hz/Px (a) all concentrations are displayed with positive contrast, while the surrounding agar is completely suppressed only leaving a fraction of remaining intensities based on the definition of the threshold value (0.3%). As already shown in the number of the positive detected pixels, the application of a fat-saturation pulse does not decrease significantly the detection of any of the concentrations (b). More positive pixels are detected by increasing TE to 34.4 ms (c). BW is increased to 70 Hz/Px (d) and 100 Hz/Px (e) with TE=20.7 ms. Here, the number of positive detected pixels is smaller, because of an increasing threshold, due to a more noisy homogeneous area. Still, all concentrations are visible and can be discriminated. In Fig.3.19 (f), the resolution of the gradient echo sequence was decreased to 0.5 x 0.5 x 0.5 mm^3 with TE=20.7 and BW=100 Hz/Px to mimic clinical relevant resolution and TA. This leads to a loss in sensitivity, in terms of detectable cells per pixel. On the other hand the detected pixels appear brighter since signal-to-noise and consequently contrast is increased. Generally more noisy pixels are visible in the MIPs due to the larger number of slices used, because false detected

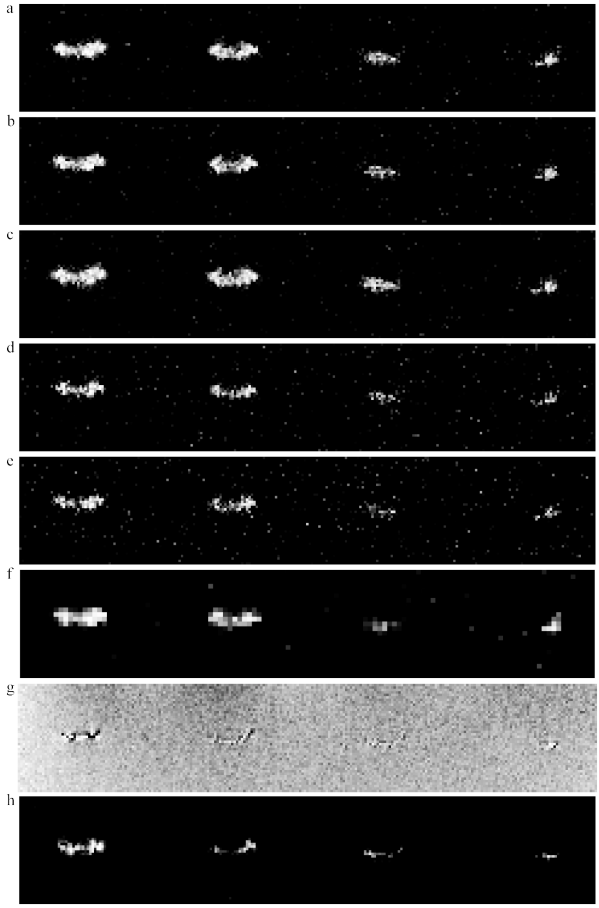

Figure 3.19: Resulting images for TE=20.7 and BW=30 Hz/Px for the regular (a) and the fat-saturated sequence (b). The fat-saturation decreases the number of positive detected pixels marginal. With a longer TE of 34.4 ms (c), more positive pixels are detected compared to (a). Increasing BW to 70 Hz/Px (d) and 100 Hz/Px (e) increases the calculated threshold resulting in fewer detected pixels compared to (a). When changing resolution to 0.5 x 0.5 x 0.5 mm^3 (with TE=20.7 ms and BW=100 Hz/Px), the number of positive pixels decreases, however, contrast improves (f). Calculated field map (ranging from -3 to 3 µT) of one slice of the dataset (g) and corresponding positive contrast image of the same slice with the filter algorithm (h).

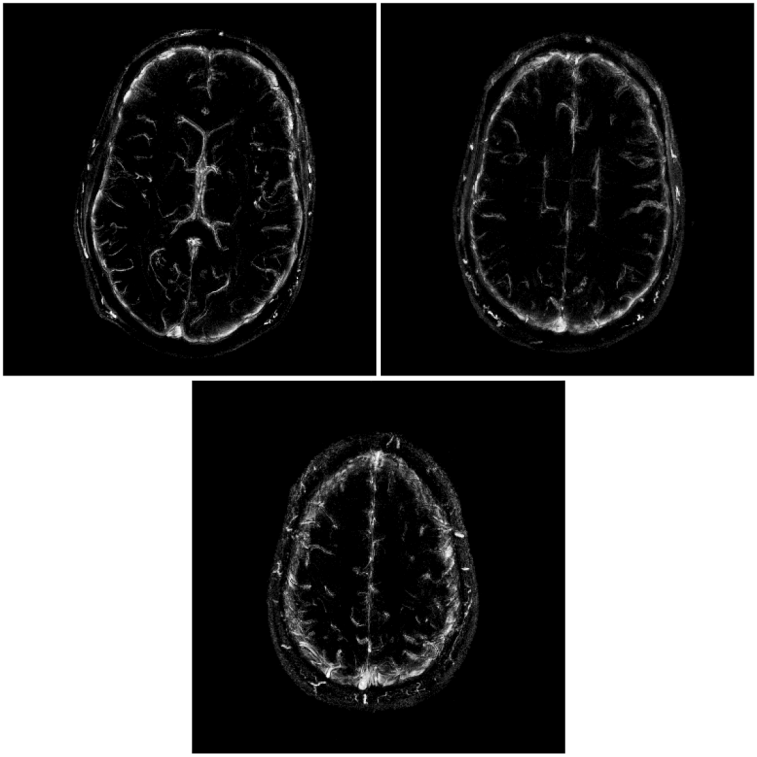

Figure 3.20: MIPs over six slices in different regions of the brain. The homogeneous areas are completely suppressed, while parts of the venous system are highlighted, due to susceptibility differences.

pixels sum up as well. However, the contrast between the labeled cells and the homogeneous areas is still high. Comparing the field map (g) and the positive contrast image (h), both images depict the same pixels as affected by the labeled cells. In the field map, large scaled field variations are visible, arising from the rectangular geometry of the box (bright regions at the left and right side) and the uneven surface of the agar (dark regions at the top). In the positive contrast image, these field variations are suppressed by the filter and the threshold.

3.5.3.6 In-vivo Imaging

3D datasets of the brain were acquired to show the suppression of homogeneous regions by the presented technique in-vivo in the absence of labeled cells. The raw-data was processed in the same way as the phantom images, i.e., the post-processing parameters were unchanged. Three resulting thin-slice MIPs (each over six slices) in different regions of the brain are shown in Fig.3.20. Here, the homogeneous cerebral tissue is completely suppressed by the algorithm. Remaining highlighted structures belong to the venous system of the brain. The difference in susceptibility between the venous blood and the cerebral tissue leads to similar echo shifts in k-space as magnetically labeled cells. Differentiation between labeled cells and veins is achievable due to the elongated course of the veins compared to a generally bulked structure of labeled cells. The resulting positive contrast of the veins shows the feasibility of the presented algorithm in the absence of labeled cells.

3.5.4 Discussion

In contrast to earlier published techniques [Sep03, Cun05, Dha06, Stu07, Kim09, Pat11, Bak06, Dah08, Fra10, Zha11], the aim of this work was to detect small concentrations of SPIO labeled cells in the absence of a macroscopic dipole field. Here, the detection is based on the altered properties of a pixel containing labeled cells, i.e., frequency, phase offset, and the resulting k-space shift. Thus, small concentrations of cells are displayed with positive contrast at the site inserted, rather than detect the dipole field in their vicinity.
The presented data show a high sensitivity of this technique for the detection of labeled cells. For lower concentrations, pixels containing less than 4 cells could be detected and discriminated against the homogeneous parts. This is a good result for the used resolution and hardware compared to earlier published works [FG03, Dod99, Lew00].
The optimum size of the raw-data filter was assessed through the evolution of the mean value in a homogeneous region of the phantom. Here, the homogeneous mean value reached a minimum at a filter-size of 40, which is in good coincidence with the filter-size used for SWI [Haa04]. The optimum filter-size is influenced by the magnetic character of the measured object or subject, the chosen TE and by the homogeneity of the used coil.
At first sight, the phantom used here seems to be a relative homogeneous

structure, which is indeed not the case. Due to the rectangular geometry of the box, the transition between air and agar produced large scaled distortions throughout the whole phantom [Lue85, Hol94]. In general, these distortions are more severe than possible distortions generated by the human anatomy, e.g., the susceptibility of bones [Sch94]. On the other side, a larger filter would reduce the intensities of the labeled cells, which would lower the amount of positive detected pixels after application of the threshold. Therefore, the experimentally found filter-size can be used for further applications in vivo for TEs up to 35 ms. For TEs shorter than 20 ms, in the case of large cell concentrations and increased BWs, or TEs longer than 35 ms, the filter can be easily adapted to match the expected susceptibility difference and TE. However, a filter-size of 40 will not lead to Fourier transformation artifacts in the filtered image since the transition of the function is smooth [Bri88], which has to be considered for smaller filters. By application of a filter with an optimum size, the homogeneous echoes situated in the k-space center and moreover the slightly shifted echoes, due to large scaled inhomogeneities, are suppressed in the filtered image. Thus, this technique is insensitive to shimming issues in contrast to frequency selective approaches [Cun05, Stu07] and compensates low frequent field oscillations.

For the determination of the threshold, the magnitude and the filtered image were sampled into ROIs with 12 x 12 pixels in size. This resulted in 1024 ROIs with 144 pixels each, which was sufficient for the calculation of a reliable mean value and a significant standard deviation. By choosing the size of the ROIs too large, possible tissue specific inhomogeneities like tissue transitions, vessels or connective tissue could increase the threshold and reduce the amount of positive pixels. On the other hand, larger concentrations of labeled cells could be imaged in more inhomogeneous backgrounds. Since the presented technique is designed to detect labeled cells with high resolution, the matrix size of the image should in any case be large to allow the sampling with ROIs of this size.

The sampling of the magnitude image and the evaluation of the mean values is necessary to remove the noise in the filtered image. It also ensures that the lowest values in the filtered image can be assigned to the most homogeneous area. Therefore, the overall mean value of the magnitude image was calculated and ROIs with lower intensities were assigned to noise, which worked for the used phantom. For images with smaller contributions of noise, possible problems could be overcome by additional evaluation of the standard deviation in the phase image, which can easily

be computed from the raw-data or by active contour algorithms.
Monitoring of the automatic detection of the homogeneous ROIs showed that the algorithm constantly found a sensible area in all slices. Regarding an increasing filter-size, the algorithm found different ROIs for small filter-size up to 15, as a result of the incomplete suppression of the large scaled agar-air transition artifacts. However, further increasing led to a constant detection of the same ROI.
The presented technique is based on a gradient echo sequence with a long TE for a sufficient phase evolution and a narrow BW. Other parameters of the sequence provide an opportunity for variation to adapt the algorithm to a specific subject or object. However, the narrow BW, necessary for the detection of small concentrations of labeled cells and for the reduction of statistical noise, could lead to unwanted chemical shift artifacts, especially in the area of fat-water transitions in human tissue. To keep the appearance of these artifacts small, the application of a fat-saturation pulse was tested with the phantom. It was shown that the influence of the saturation pulse on the detection of labeled cells was small. The loss in positive pixels compared to the regular sequence was below 10%. Since a higher BW would result in an increased threshold and therefore would lead to a more severe loss in positive detected pixels, the use of a fat-saturation pulse for a further application of the presented technique in vivo, in addition to an in-phase TE, seems preferable.
A higher concentration of labeled cells with a significantly shorter T_2^* will not be detected as positive intensity at the place inserted, instead the magnetic dipole field will be highlighted. A better localization of higher concentrations can be achieved by a reduction of TE, however, at the cost of the detection of lower concentrations. Additionally, for higher concentrations possible distortions in read direction have to be considered, which have to be compensated by higher BWs [Bos03].
As the results from the in-vivo imaging of the head show, not only labeled cells but also other sources of susceptibility alterations can be imaged with positive contrast. Low signal tissue and noise are excluded in the resulting image by the raw-data filter and the application of the cut off threshold, respectively. Thus, the ambiguity of hypointensities in a negative contrast image can be avoided with the presented positive contrast technique. A clear distinction of susceptibility alterations, like labeled cells or venous vessels, is possible.
A reduction of the resolution results in a lower sensitivity so that more labeled cells have to be apparent in a voxel for an echo shift in k-space.

However, it is still possible to visualize single k-space shifted pixels with positive contrast as shown in Fig.3.19. Thus, for in-vivo imaging with larger fields of view, a compromise between sensitivity and TA has to be found. On the other hand, lower resolutions result in higher signal-to-noise ratio, thus improving contrast.
Post-processing was carried out with a Hanning filter, because it is the most commonly used filter type in MRI. However, other filter functions are possible, but a precise investigation in the effects of different filter types would require a phantom with a more distinct distribution of labeled cells. One possible approach to the quantification of susceptibility effects is field mapping, as shown in Fig.3.19. Therefore, a second dataset with ΔTE=1 ms was acquired and the phase differences were calculated. The resulting field map showed field variations in the same pixels that were detected with the filter algorithm, at the cost of a doubled TA. On the one hand, a field map allows quantitative evaluation of field differences. On the other hand, large scaled inhomogeneities complicate an automatic detection of labeled cells, since the field varies over the image and a general field value cannot be defined.
A post-processing technique capable of detecting echo shifted pixels qualitatively and quantitatively is susceptibility gradient mapping (SGM) at the cost of image resolution and visualization of small susceptibility gradients [Dah08]. Recently, an improvement of SGM maintaining image resolution was introduced (SUMO) showing better detection of titanium prostate seeds compared to SGM [Var11]. However, as stated in their work, both SGM and SUMO are relatively time consuming techniques compared to a practically instantaneous computation for the presented algorithm ($<$0.5 s per slice). Therefore, the presented technique could be used during MR examinations for an accurate detection of labeled cells. If quantification is necessary, subsequent processing steps could then be taken on an external workstation, e.g., with SGM or SUMO by use of the same dataset.

3.5.5 Conclusion

A straightforward post-processing technique is presented, which is capable of detecting susceptibility alterations like magnetically labeled cells with positive contrast. Raw-data of a gradient echo sequence was processed with an inverse Hanning filter, suppressing homogeneous echoes in k-space. Post-processing steps were introduced, which remove statistical noise and find a homogeneous region in the object used to define a thresh-

old. Application of the threshold increases the contrast in the filtered image by cutting off low intensities. The sensitivity of this technique was shown on an agar phantom containing different concentrations of labeled cells. It was shown that 4 labeled cells per pixel can be detected and clearly discriminated from the surrounding agar with positive contrast. Initial testing in vivo with images of the brain showed complete suppression of homogeneous areas, while susceptibility differences were displayed with positive contrast. The presented technique allows unambiguous detection of regions affected by susceptibility and thus the discrimination of regions with natural low signal. Further applications in vivo other than the monitoring of labeled cells are conceivable.

3.6 General Discussion

It was shown that a reliable detection of iron-oxide loaded cells in a phantom and in ex-vivo tissue is feasible with the newly developed positive contrast techniques. The technique based on the SWI post-processing algorithms proved superior ability for the suppression of the background tissue in the presence of B_0 and B_1 field inhomogeneities. The filter technique, however, showed a higher sensitivity toward lower concentrations of labeled cells and was able to completely suppress weaker susceptibilities. Both techniques are based on gradient echo sequences allowing rapid image acquisition. The key sequence parameters are a relative long TE, i.e., strong T_2^*-weighting, and a narrow BW necessary for a high signal-to-noise ratio. An important factor for clinical usage of the developed techniques is not only TA of the image, i.e., the duration of the sequence, but also the duration of the post-processing. For both techniques the requirements on computational performance are low, so that even with a standard, vintage personal computer post-processing could be performed within a few seconds for a 3D dataset. The main difference between the two developed techniques is the way the raw-data filter is applied. In the SWI post-processing algorithm, the filter is used to generate smoothed phase images similar to the application of a high-pass filter. In the filter technique, the consequences of the filter application are directly evaluated in the magnitude image, without the processing of the phase image. The gray values in the filtered magnitude image are therefore linked to the frequency offsets in the raw-data image. On the one hand, this allows a fully automated procedure for the suppression of the homogeneous image parts and on the

other hand these post-processing steps can also be used for other than gradient echo imaging sequences, however, certainly with limited sensitivity. The focus of the developed techniques was the detection of iron-oxide labeled cells. Apart from localization, one major interest in cell tracking is the quantification of viable cells. However, this aim cannot be achieved by the assessment of local field inhomogeneities, which are used for the detection of cells in all publications so far. The reason is that the loading of single cells with iron-oxide is strongly irregular and results in different magnetic field patterns for cells with an identical iron-oxide uptake.

Chapter 4

Visualization of Interventional Devices

4.1 Introduction

In interventional MRI, reliable tracking of minimally invasive instruments is essential. Several approaches have been investigated, all showing specific limitations [Boc08, Kos08], and the search for improved methods is still going on [And12, Won00, Sha13, Woj10]. The most widely used technique for MR tracking of medical devices such as catheters or needles is based on susceptibility artifacts caused by the special material of the instrument, e.g., titanium [Lad96]. The magnetic field inhomogeneities in the vicinity of the device reduce T_2^*-time of the spins. Signal voids result in gradient echo images. As signal voids can also result from low proton density, iron deposits or deoxyhemoglobin or partial volume effects, the precision of instrument localization is limited. False spatial encoding due to locally disturbed imaging gradients is a further problem. In addition, the size of the artifact is defined by the material of the device and the sequence parameters. Size manipulation via the sequence parameters is limited by the demand of low influence on tissue contrast. A change of material can hardly be accomplished during examination.
Glowinski et al. [Glo97, Glo98] introduced a possibility for controllable artifact sizes by use of a special catheter. A cable at its surface was connected to an electric power supply. The modified catheter could easily be

depicted in gradient echo images due to the magnetic field inhomogeneities related to an applied current. A separation between the catheter's artifact and other low signal zones was achieved by subtraction of a current off image from a current on image. Adam et al. [Ada98] approved the technique in vivo.
In this chapter, a spin echo based technique, similar to that used by Joy et al. [Joy89] for the visualization of current paths in tissue (Current Density Imaging), is examined with respect to its potential for separation of susceptibility artifacts and artifacts induced by direct currents in a metallic conductor [Gra12]. The current is switched on only for a specific time period during the sequence, i.e., causes transient, local field inhomogeneities, which are connected to specific spin echo artifacts [Gra05, Woj11b]. Spin echo magnitude and phase images are evaluated. Since they are acquired simultaneously, a single scan is sufficient for reliable localization of the current carrying conductor.

4.2 Material and Methods

4.2.1 Theory

The magnetic susceptibility difference between metallic structures and the surrounding medium or tissue invokes local magnetic field inhomogeneities. They can be considered persistent during acquisition if motion is neglected and result in typical artifacts, depending on the imaging technique. Extent, shape, and depiction of the artifacts are not only determined by the susceptibility difference but also by the choice of sequence parameters. In gradient echo images, susceptibility artifacts depict as signal voids due to a reduced T_2^*-time (intra-voxel dephasing). In spin echo images, effects from spatial misregistration during excitation and readout become visible, since they are no longer superimposed by dephasing signal losses as is the case in gradient echo images. The extent of the artifacts can be manipulated within a certain range by the choice of sequence parameters, preferentially by TE and BW.
An alternative approach for the generation of image artifacts in MRI is by use of an electric current [Woj11a]. In contrast to susceptibility artifacts, the artifact induced by an electric current is controllable with amperage. An electric current in a conductor generates a concentric magnetic field as defined by Ampère's circuital law. The z-component of this concentric magnetic field, i.e., the component parallel to the static field B_0, is effec-

tive in MRI. If the electric current is constant during the sequence, the effective magnetic field of the current results in a persistent field inhomogeneity. Dephasing artifacts as well as misregistration during readout and distortion during slice encoding occur in analogy to susceptibility induced inhomogeneities. Constant current induced artifacts and susceptibility artifacts are therefore hardly distinguishable.
This problem can be solved by switching on the current only during definite time periods within the sequence. The effective magnetic field near such a triggered current results in transient, magnetic field inhomogeneities. The spins dephase in the vicinity of the conductor during the time period the current is applied [Ada98]. As a result, a small signal void is generated due to intra-voxel dephasing in gradient echo as well as spin echo magnitude images. However, in magnitude images the artifact caused by a transient current can still not be reliably distinguished from artifacts caused by persistent field inhomogeneities or from low signal tissue.
A separation of susceptibility artifacts or low signal tissue from triggered current artifacts can be achieved by assessing spin echo phase images. In contrast to gradient echo phase images, spin echo phase images in most cases bear hardly important information and they are rarely reconstructed. All spins, independent on magnetic field homogeneity, are completely rephased and a homogeneous image with uniform phase values results.
By application of a sequence triggered current, e.g., between RF-excitation and refocusing, spins in the vicinity of the conductor obtain a phase offset as a consequence of the current related additional magnetic field. As this field misses after the 180° RF-pulse, refocusing is not possible and the phase offset near the current is the only source of contrast in the spin echo phase image. In addition, if the current is switched on only at times when imaging gradients are inactive, false spatial encoding can be avoided.

4.2.2 Phantom

A piece of plastic tube with a diameter of 11 cm and a height of 10 cm was used as a holder for a cylindrical brass conductor (diameter 1.6 mm, length 120 mm, electrical conductivity ≈15 MS/m) and a titanium rod (diameter 1.3 mm, length 130 mm) (Fig.4.1). Brass (CuZn37) was used as conductor material because of its water equivalent magnetic susceptibility ($\chi_{SI} = -16 \cdot 10^{-6}$). The titanium rod served as a source for susceptibility artifacts ($\chi_{SI} = 180 \cdot 10^{-6}$). Holes were drilled into the plastic tube to

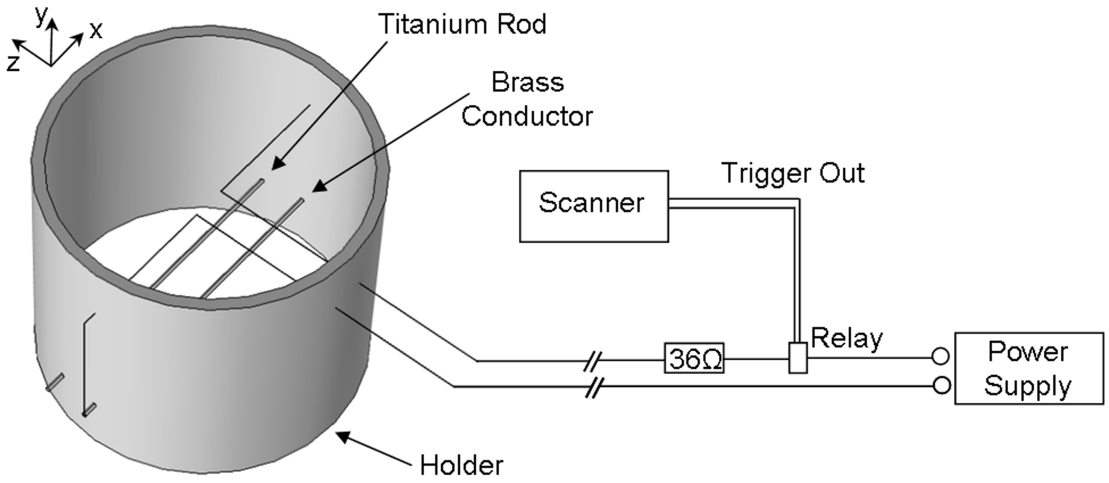

Figure 4.1: Sketch of the phantom setup and the electric network. The trigger output of the scanner switches the relay for sequence controlled current supply to the brass conductor. The setup avoids wire loops with large cross sections for RF-coupling during excitation pulses and resulting phase changes [Gra06]. Gradient switching induced currents are also avoided by placing the center of the vertical rectangular loop at the isocenter.

fix the conductor and the rod parallel to each other at a distance of 2.5 cm. Copper wires were soldered to both ends of the brass and attached to a cable, which was long enough to get connected to a 20 V power supply in a safe distance to the scanner. For electrical matching to the power supply, a 36 Ω resistor was attached in series to the brass conductor. For sequence triggered current switching, an electronic load relay was inserted into the current supply line. The control input of the electronic load relay was connected to the trigger output of the scanner. The switching speed of the relay was measured with a pulse generator and an oscilloscope to 0.1 ms. The plastic tube with the samples was placed in an acrylic glass box (20 cm x 20 cm), which was filled with 2.5 L of gadolinium doped water (electrical conductivity 0.05 S/m). The box was placed in the center of the scanner. Orientations of the conductor and the titanium rod parallel to the x-z-plane were investigated.

4.2.3 Sequences

A spin echo and a gradient echo sequence were modified to obtain a trigger signal at the external trigger output of the scanner (Fig.4.2). The duration of the trigger was fixed to 1 ms. In both sequences, the trigger was switched after the excitation pulse at times when imaging gradients were inactive. In the case of the gradient echo sequence, this was achieved by shortening of the readout dephasing gradient by 1 ms and simultaneously increasing the gradient's amplitude. In the spin echo sequence, a modification of the readout dephaser was not necessary, because a gradient free time period of 1 ms was available between excitation and refocusing for TEs longer than 15 ms. The trigger signal output was checked with an oscilloscope. The sequence parameters of the spin echo sequence were: TE=16 ms, TR=500 ms, BW=130 Hz/Px, slice thickness=5 mm, averages=1, matrix size=512 x 512 and 256 x 512, and field of view=256 x 256 mm^2 and 128 x 256 mm^2, for coronal and sagittal slice orientation, respectively. The same parameters were used for the gradient echo sequence except for TE, which was 10 ms. TA was 4:18 min for the coronal and 2:10 min for the sagittal slices.

4.2.4 Measurements

Measurements were performed with a 1.5 Tesla whole body scanner Vision Sonata (Siemens Healthcare, Erlangen, Germany) by use of the built-in

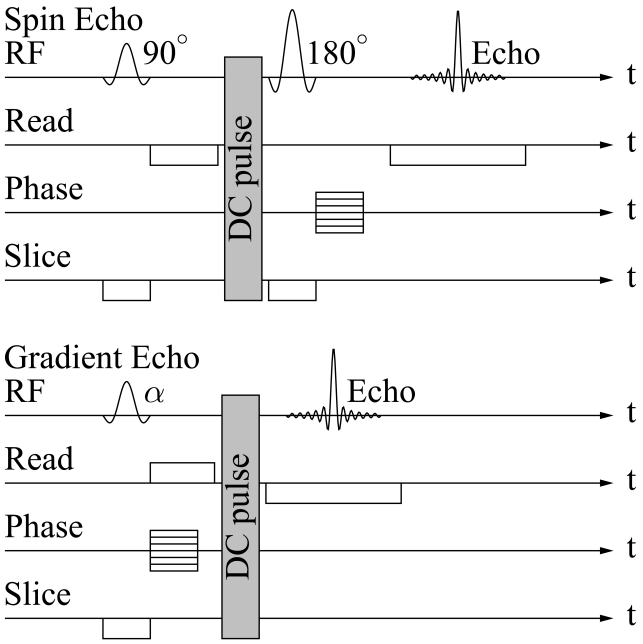

Figure 4.2: Sequence diagrams for the spin echo and gradient echo sequences with the timing of the sequence triggered DC pulses.

body coil. Spin echo imaging with coronal slices was performed (orientation of the conductor 90° to the static field) and compared to the corresponding gradient echo images. Images were acquired with a triggered current of 0.1 A, a constant current of 0.1 A, and with the current switched off. Three values of amperage (0.05 A, 0.15 A, and 0.25 A) were examined with both sequences (orientation 90°, sagittal slice) to show the controllability of the artifact size. For the investigation of the orientation dependency, the conductor was rotated around the y-axis. Spin echo images were acquired in coronal slice orientation as well as for slices oriented perpendicular to the conductor at half of its length. The conductor orientations were 0°, 30°, 60°, and 90° with respect to the direction of the main magnetic field. The amperage was 0.1 A.

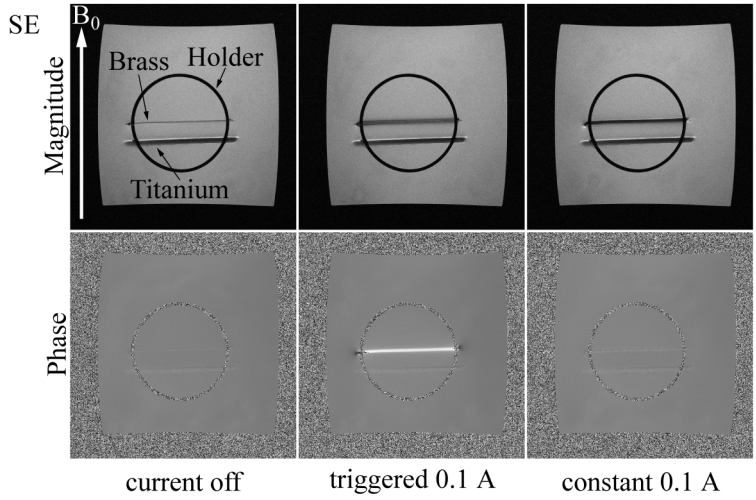

Figure 4.3: Coronal spin echo magnitude and phase images of the phantom without current, triggered current and constant current. In the first and latter, the conductor generates persistent field inhomogeneities. Spin dephasing can be reversed in spin echo technique. Neither the titanium needle nor the conductor is visible in the phase image. With triggered current, the transient field disturbance around the conductor becomes visible, allowing a distinct localization.

4.3 Results

Spin echo magnitude and phase images (value range from $-\pi$ to π) of the phantom with triggered, constant and without current are shown in Fig.4.3. Without current, the only source of contrast for depicting the conductor in the magnitude image is reduced mean proton density, i.e., water displacement. This results in slightly noisier pixels around the conductor in an otherwise homogeneous phase image. The application of a triggered current increases the signal void in the magnitude image around the conductor due to spin dephasing. In the phase image, the conductor becomes visible as a result of the additional, transient magnetic field in its vicinity causing an uncompensated phase offset of the spins. This phase offset is the only source of contrast in the spin echo phase image and allows for a distinct localization of the conductor. If the current is constant during the whole sequence, the artifact around the conductor is similar to the suscep-

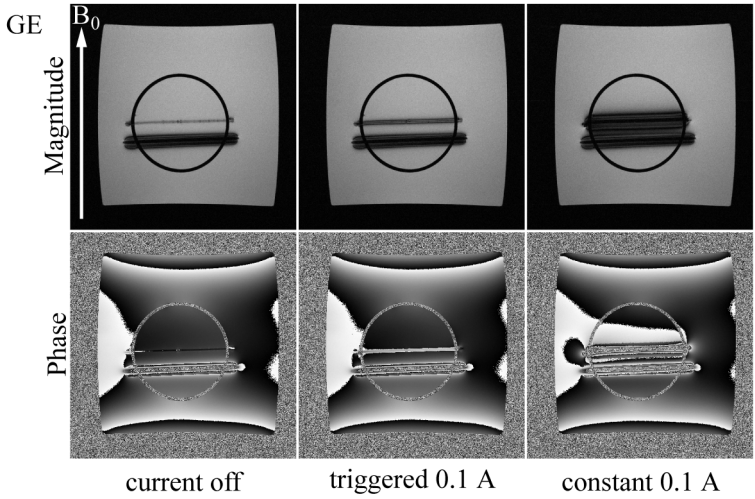

Figure 4.4: Coronal gradient echo magnitude and phase images of the phantom without current, triggered current and constant current. Because of its water equivalent susceptibility, without current, the conductor shows only small artifacts in the magnitude and the phase image. With triggered current, a phase offset is visible around the conductor. A distinct localization is not possible, because spin dephasing in the presence of persistent inhomogeneities, e.g., caused by the titanium needle, can not be reversed by the gradient echo sequence. Effects from persistent inhomogeneities stay superimposed.

tibility artifact of the titanium needle and the typical patterns of spatial misregistration occur in the magnitude images. The constant current is related to persistent local field inhomogeneities. Related dephasing can be reversed by the 180° RF-pulse of the spin echo sequence and phase effects are nulled in the phase image. Constant current as well as susceptibility induced magnetic field inhomogeneities have no effect on the spin echo phase images.

In Fig.4.4, gradient echo images of the same slice as in Fig.4.3 are shown. In the magnitude images without current, the conductor is again visible only because of locally reduced mean proton density. The corresponding phase image reveals phase variations due to persistent field inhomogeneities induced by imperfect shimming and by the titanium needle. With triggered DC, the size of the artifact around the conductor increases in the magni-

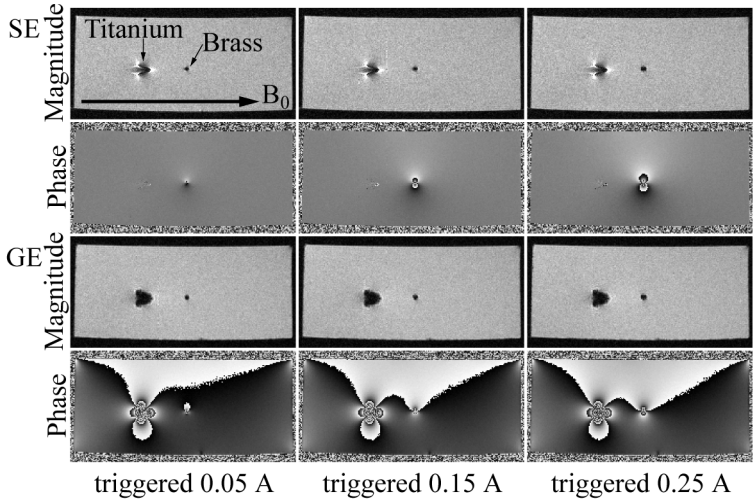

Figure 4.5: Artifacts generated by the triggered current in sagittal spin echo and gradient echo magnitude and phase images for different values of amperage. In the magnitude images, the artifact increases for both sequences because of intra-voxel dephasing, but relatively slightly. In the phase images, the effect of the amperage on the size of the induced artifact is more obvious. Discrimination between persistent and transient inhomogeneities is only possible in the spin echo phase images. In the gradient echo phase images, the phase offset around the conductor is superimposed to large-scale field inhomogeneities.

tude image and the phase offset becomes visible in the phase image. This observation is similar to that obtained in spin echo technique. However, distinct localization of the conductor is not possible, because the gradient echo sequence does not allow for differentiation between persistent and transient magnetic field distortions. The application of a constant current generates an artifact around the conductor, which is similar to the titanium needle's susceptibility artifact, in the magnitude image and in the phase image as well.
The amperage control of the triggered current artifacts is shown in Fig.4.5. Spin echo and gradient echo magnitude and phase images were acquired in sagittal orientation for better visualization. The titanium needle is visible in the magnitude images either as misregistration artifact or as signal void in spin echo and gradient echo imaging, respectively. In gradient echo

phase images, the typical dipole field related artifact is apparent. In the spin echo phase images, the titanium needle does not visualize, i.e., spin dephasing is completely reversed also in the inhomogeneous field zone near the needle. For the conductor, as a consequence of intra-voxel dephasing, the size of the artifact slightly increases with increasing amperage in both spin echo and gradient echo magnitude images. Compared to the artifacts in the magnitude images, the size of the phase artifact shows a stronger dependence on amperage. The shape of the artifacts reflects the effective magnetic field induced by the triggered current. Even with the lowest amperage used, visible phase offset values are obtained. Again, a distinct and reliable localization of the conductor is only possible in the spin echo phase image, where artifacts from persistent inhomogeneities, as present in gradient echo phase images, are suppressed completely by rephasing.
The orientation of the conductor with respect to the main magnetic field was varied to show the dependency of the spin echo phase artifact on the direction of current flow (Fig.4.6). For an orientation parallel to the static field (0°), the magnetic field of the conductor lacks a z-component. Accordingly, no phase offset is generated by the current. Minor phase changes must be attributed to RF-coupling effects. With a rotation of the conductor to 30°, the distinct phase offset becomes visible. Artifact extension and the value of the phase offset are comparable to the case of perpendicular needle orientation at the lower amperage of 0.05 A (Fig.4.5). For a rotation of 60°, artifact extension and the value of the phase offset around the conductor are very similar to that obtained for 90° orientation. The phase offsets in the lower images of Fig.4.6 were quantitatively evaluated along a vertical line through the position of the conductor (Fig.4.7).

4.4 Discussion

Application of sequence triggered direct currents through a conductor results in transient field inhomogeneities, which can be visualized as a phase offset not only in gradient echo phase images, but in spin echo phase images as well. The size of the phase offset artifact is controllable with amperage and dependent on the orientation of the conductor with respect to the static field. Especially in spin echo phase images, a distinct localization of the conductor is possible, because spin dephasing due to persistent inhomogeneities is completely reversed by the 180° RF-pulse. No background phase structure disturbs the localization of the current path. Also in vivo,

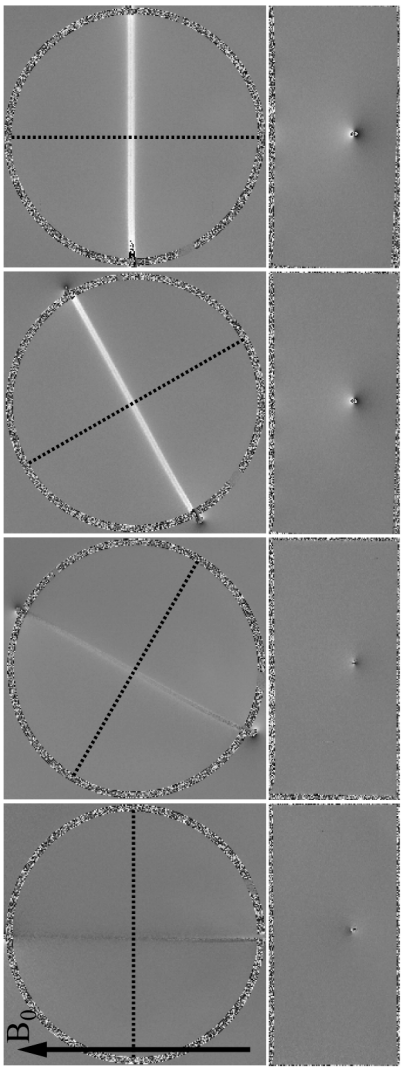

Figure 4.6: Spin echo phase images for different orientations of the conductor with respect to the main magnetic field. The imaging plane is coronal (upper images) and perpendicular (indicated by the dotted line) to the conductor (lower images). For parallel orientation (0°), the triggered current generates no phase offset. By rotation of the conductor to 30°, a phase artifact becomes visible. For an orientation of 60°, the size and value of the phase artifact is almost at its maximum as obtained for 90°.

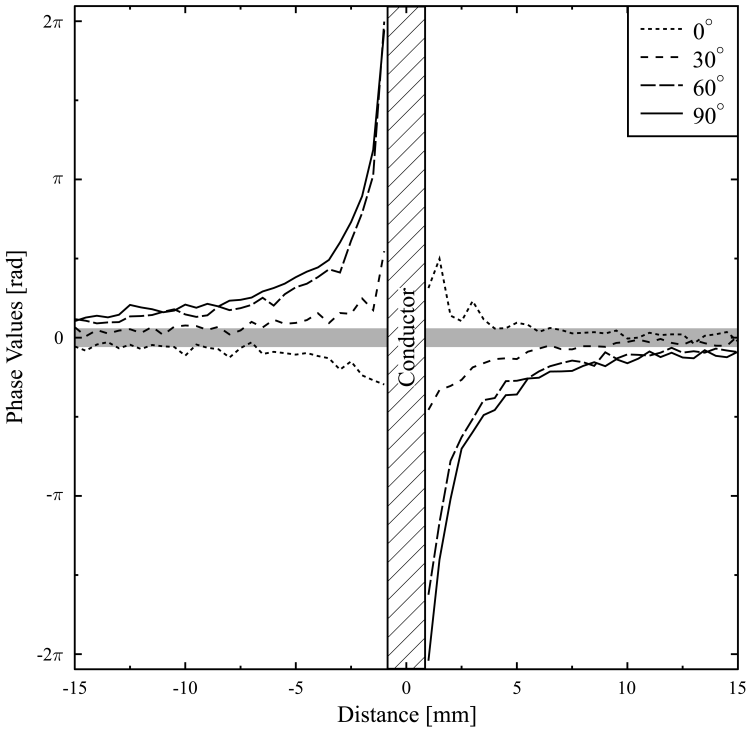

Figure 4.7: Quantitative evaluation of the phase values (unwrapped) from the measurements shown in Fig.4.6. For the orientations 90° and 60°, the theoretically expected inverse proportionality of the phase offsets to the distance from the conductor is confirmed. Despite the conductor generates no effective z-magnetic field for an orientation of 0°, a phase offset is visible, which originates from RF-induced currents. This was confirmed by measurements without triggered current application. RF-coupling must be expected to influence also the measurements for the 30° orientation. However, the phase offset generated by the triggered current dominates.

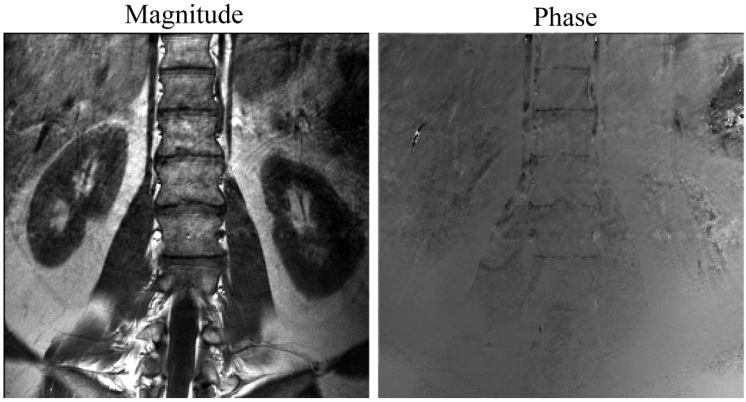

Figure 4.8: Coronal spin echo magnitude and phase image of the kidney region of a healthy volunteer. The refocusing of the spin echo sequence generates same phase values for the different tissues. Visible structures in the phase image originate from signal free areas (noise) or motion (blood flow). Sequence parameters were identical with the parameters of the in-vitro measurements except for in plane resolution which was 1 mm x 1 mm.

spin echo sequences generate homogeneous phase images (Fig.4.8). Evaluation of the phase values of the whole kidney in the left part of the image revealed a standard deviation of the phase of 0.21 rad (marked as a gray bar in Fig.4.7). The measured phase change in a distance of 1 mm from the conductor for 30° orientation and 0.1 A was 0.85 rad, i.e., clearly larger than this variance.

The acquisition of the phase image does not require extra scan time, since it can be reconstructed from the same raw data as the magnitude image. Geometrical resolution and field of view of both image types are identical being a perfect basis for further image processing. In a recent work of Anderson et al. [And12] the evaluation of phase information for instrument localization is proposed, too. However, they use the more complicated technique with micro RF-coils attached to the instrument and confine themselves to gradient echo imaging.

The observation of instrument movement in interventional MRI requires fast imaging and in general is done using gradient echo techniques. As described, for gradient echo techniques a background free localization of a transient visualization current in the phase image is impossible. However,

gradient echo techniques will also benefit from current based visualization. At first, even for an untriggered constant current, amperage can be varied and adjusted to influence artifact size for optimum instrument visualization, leaving sequence parameters and thus the image contrast untouched. The current can even be switched off completely making an instrument with a water equivalent susceptibility suitable for MR temperature monitoring [Bos05]. Working in triggered mode allows for undisturbed slice selection and readout gradients to avoid false spatial encoding near the instrument.

The possibility of taking influence on the artifacts independently and easily by the current with the instrument in place has lead to the suggestion of Glowinski et al. [Glo97, Glo98] to subtract a magnitude image acquired with current off from an image acquired with current on for the separation of the effects from the current. This technique could be refined using sequence triggered current application. Interleaved application, i.e., k-space line by k-space line, seams to be more advantageous compared to the acquisition of two consecutive images.

Signal loss due to dephasing in macroscopic field inhomogeneities, i.e., due to magnetic field variations on a scale comparable to the dimension of a voxel, depends on voxel size. There is basically no difference between susceptibility induced and current induced effects. For both cases, artifacts could be reduced with higher spatial resolution. The phase artifact generated by the triggered current in spin echo sequences depends on spatial resolution but is not influenced by variation of other imaging parameters. The triggered current in the spin echo sequence was applied in a gradient free time slot between excitation and refocusing. However, current switching during phase encoding or during readout pre-dephasing is also possible without compromising image quality [Sco92]. This would allow a more flexible choice of TE, in this case smaller than 16 ms, and the use of faster imaging sequences, which are more often applied in clinical imaging. The time period of current application, which was 1 ms in this case, could be reduced for faster sequences at simultaneously increased amperage. The modification of the sequence itself is relatively unproblematic, since elementary programming steps as well as the external trigger output are already implemented by the manufacturer in the software of most modern scanners.

It was shown that beginning with an angle of 30° with respect to the main magnetic field, the conductor could be visualized. Most MRI guided interventional procedures in the meantime use horizontal bore superconducting

magnets. For applications using needles, i.e., for biopsies or RF-ablation, it is not expected that angles of the conductor lower than 30° with respect to the main magnetic field are of importance. Thus, the angle dependency of the phase artifact seems unproblematic, especially because susceptibility artifacts as commonly used for interventional device tracking show a similar dependency on orientation.
However, for application of the described technique with needles in c-shaped magnets and for catheter applications in horizontal bore magnets, a more complex kind of conductor becomes necessary. Glowinski et al. [Glo97] have described several geometrical solutions for conductor arrangements, for which the current produces the necessary magnetic field z-component.
The presented technique for distinct localization of metallic conductors by use of sequence triggered direct currents could be a helpful tool for the tracking of interventional devices. The technique offers free choice of the sequence parameters and controllable artifact sizes. No additional acquisition is necessary in combination with spin echo sequences. Especially for cases in which the interventional device is already electrically connected to an external generator, such as given for RF-ablation, an implementation of this technique could be done easily.
The development of suitable applicators might be a little bit more challenging, especially for catheters, but seems to be worthwhile considering the shown advantages. Gradient echo visualization benefits clearly and the described spin echo phase based technique is estimated to allow for exact localization, especially in critical situations or for final instrument placement.

Chapter 5

Conclusions

In the last years, MRI has become a widely used technique for diagnostic imaging. The advantages of MRI are its excellent soft tissue contrast with the possibility to achieve a variety of image weightings and, in contrast to computed tomography, the absence of ionizing radiation. However, the way an image is generated in MRI gives rise to artifacts. Two major sources of artifacts are patient motion, especially breathing, and susceptibility differences. Whereas patient motion artifacts can be reduced by imaging in breath hold or imaging techniques, which compensate motion, susceptibility artifacts can prohibit diagnostics for example in the vicinity of metallic implants.
The alteration of the magnetic field near magnetic markers can also be used for diagnostic purposes. Local, induced field alterations, which are strong enough to be visualized with MRI but weak enough to maintain a local phenomenon, can be attached to living cells and monitored while migrating through the body. In Chapter 3 of this thesis, two methods for the visualization of magnetically labeled cells were presented. Both techniques are based on conventional gradient echo sequences. Post-processing steps were established that allowed for the generation of positive contrast in areas with susceptibility alterations with simultaneous suppression of the homogeneous background. In homogeneous tissue, as few as only four labeled cells could be identified with optimized post-processing and sequence parameters. In the absence of labeled cells, the developed techniques were able to detect venous vessels, which also possess a different susceptibility compared to the surrounding tissue, in a human brain. The main focus

during the development of the post-processing techniques was to achieve positive contrast near magnetically labeled cells while keeping computation time of the algorithm short. Furthermore, the post-processing algorithms should be applicable to conventional sequences. As a result, the whole processing steps took only a few seconds for a complete dataset on an external personal computer. For both techniques, cells were labeled with Resovist, a contrast agent developed for liver imaging. At the moment, Resovist is not available any more, but specialized contrast agents for cell labeling are being developed, which are smaller in size and could be better incorporated by the cells. As long as superparamagnetic markers are used for cell tracking with MRI, the presented post-processing algorithms are an option for the generation of positive contrast near magnetically labeled cells.

Another technique utilizing induced artifacts was described in Chapter 4. Generally, interventional devices are made of metallic alloys or synthetic material. If metallic alloys are used as material, in most cases the susceptibility of the material strongly differs from the surrounding tissue resulting in large signal voids or misregistration artifacts. In contrast, small devices made of synthetic material are often non-magnetic and cannot be detected by use of susceptibility artifacts in MRI. The developed technique showed a possibility to visualize non-magnetic devices with magnetic field distortions induced by direct currents. Here, the aim was the generation of an artifact that can clearly be discriminated from susceptibility artifacts or low signal areas. Therefore, a brass rod was used as a conductor for a direct current, which was switched on and off during the spin echo sequence. By switching on the current only in certain time intervals during the sequence, a transient, local, magnetic field was generated by the current resulting in a distinct artifact in spin echo phase images. The modification of a device and the scanner software is relatively simple, thus this technique could be an alternative approach for localization of interventional devices, especially for devices that are already connected to a power supply. So far, the technique was implemented with a conventional spin echo sequence. For device tracking, a modification of a faster sequence is necessary.

The alteration of the magnetic field in MRI can result in deliberate, local artifacts. These artifacts are not in the least negative for the diagnostic evaluation of the images, but can give guidance for the radiologist to detect special structures. Because of its variety of applications MRI will be the first choice for cell tracking and interventional diagnostics in the future.

References

[Abr83] A. Abragam. *Principles of nuclear magnetism.* Oxford, Oxford (**1983**).

[Ada98] G. Adam, A. Glowinski, J. Neuerburg, A. Bücker, J. J. van Vaals and R. W. Günther. *Visualization of MR-compatible catheters by electrically induced local field inhomogeneities: evaluation in vivo.* J. Magn. Reson. Imaging **8**, 209–213 (**1998**).

[And12] K. J. T. Anderson, G. C. Scott and G. A. Wright. *Catheter tracking with phase information in a magnetic resonance scanner.* IEEE Tran. Med. Imaging **31**, 1173–1180 (**2012**).

[Bak06] C. J. G. Bakker, J. Seppenwoolde and K. L. Vincken. *Dephased MRI.* Magn. Reson. Med. **55**, 92–97 (**2006**).

[Ber04] M. A. Bernstein, K. F. King and X. J. Zhou. *Handbook of MRI pulse sequences.* Academic Press, Waltham (**2004**).

[Ber05] L. Bergmann, C. Schaefer and R. Kassing. *Lehrbuch der Experimentalphysik, Band 6, Festkörper.* de Gruyter, Berlin (**2005**).

[Bie07] O. Bieri, S. Patil, H. H. Quick and K. Scheffler. *Morphing steady-state free precession.* Magn. Reson. Med. **58**, 1242–1248 (**2007**).

[Blo46] F. Bloch, W. W. Hansen and M. Packard. *The nuclear induction experiment.* Phys. Rev. **79**, 474–485 (**1946**).

[Boc08] M. Bock and F. K. Wacker. *MR-Guided intravascular interventions: techniques and applications.* J. Magn. Reson. Imaging **27**, 326–338 (**2008**).

[Bos03] C. Bos, M. A. Viergever and C. J. Bakker. *On the artifact of a subvoxel susceptibility deviation in spoiled gradient-echo imaging.* Magn. Reson. Med. **49**, 400–404 (**2003**).

[Bos05] A. Boss, H. Graf, B. Müller-Bierl, S. Clasen, D. Schmidt, P. L. Pereira and F. Schick. *Magnetic susceptibility effects on the accuracy of MR temperature monitoring by the proton resonance*

frequency method. J. Magn. Reson. Imaging **22**, 813–820 (**2005**).

[Bow02] C. V. Bowen, X. Zhang, G. Saab, P. J. Gareau and B. K. Rutt. *Application of the static dephasing regime theory to superparamagnetic iron-oxide loaded cells.* Magn. Reson. Med. **48**, 52–61 (**2002**).

[Bri88] E. O. Brigham. *The fast Fourier transformation and its applications.* Prentice Hall, Englewood Cliffs (**1988**).

[Bul09] J. W. Bulte. *In vivo MRI cell tracking: clinical studies.* AJR Am. J. Roentgenol. **193**, 314–325 (**2009**).

[Cal93] P. T. Callaghan. *Principles of nuclear magnetic resonance microscopy.* Oxford, Oxford (**1993**).

[Can91] D. Canet. *NMR-Konzepte und Methoden.* Springer, Berlin (**1991**).

[Car58] H. Y. Carr. *Steady-state free precession in nuclear magnetic resonance.* Phys. Rev. **112**, 1693–1701 (**1958**).

[Che95] G. N. Chen and D. I. Hoult. *Biomedical magnetic resonance technology.* IOP Publishing, Bristol (**1995**).

[Chr92] J. R. Christman. *Festkörperphysik.* Oldenbourg, München (**1992**).

[Cun05] C. H. Cunningham, T. Arai, P. C. Yang, M. V. McConnell, J. M. Pauly and S. M. Conolly. *Positive contrast magnetic resonance imaging of cells labeled with magnetic nanoparticles.* Magn. Reson. Med. **53**, 999–1005 (**2005**).

[Dah08] H. Dahnke, W. Liu, D. Herzka, J. A. Frank and T. Schaeffter. *Susceptibility gradient mapping (SGM): a new postprocessing method for positive contrast generation applied to superparamagnetic iron oxide particle (SPIO)-labeled cells.* Magn. Reson. Med. **60**, 595–603 (**2008**).

[Dam71] R. Damadian. *Tumor detection by nuclear magnetic resonance.* Science **171**, 1151–1153 (**1971**).

[Dam77] R. Damadian, M. Goldsmith and L. Minkoff. *NMR in cancer: XVI. FONAR image of the live human body.* Physiol. Chem. Phys. **9**, 97–100,108 (**1977**).

[Dha06] R. Dharmakumar, I. Koktzoglou and D. Li. *Generating positive contrast from off-resonant spins with steady-state free precession magnetic resonance imaging: theory and proof-of-principle experiments.* Phys. Med. Biol. **51**, 4201–4215 (**2006**).

[Dha07] R. Dharmakumar, I. Koktzoglou and D. Li. *Factors influencing fast low angle positive contrast steady-state free precession*

(FLAPS) magnetic resonance imaging. Phys. Med. Biol. **52**, 3261–3273 (**2007**).

[Dod99] S. J. Dodd, M. Williams, J. P. Suhan, D. S. Williams, A. P. Koretsky and C. Ho. *Detection of single mammalian cells by high-resolution magnetic resonance imaging.* Biophys. J. **76**, 103–109 (**1999**).

[Eib10] F. Eibofner, G. Steidle, R. Kehlbach, R. Bantleon and F. Schick. *Positive contrast imaging of iron oxide nanoparticles with susceptibility-weighted imaging.* Magn. Reson. Med. **64**, 1027–1038 (**2010**).

[Eib12] F. Eibofner, G. Steidle, R. Kehlbach, R. Bantleon and F. Schick. *Utilizing echo-shifts in k-space for generation of positive contrast in areas with marked susceptibility alterations.* Magn. Reson. Med. **68**, 1399–1409 (**2012**).

[Eib14] F. Eibofner, H. Wojtczyk, H. Graf and S. Clasen. *Magnetic resonance visualization of conductive structures by sequence-triggered direct currents and spin-echo phase imaging.* Med. Phys. **41** (**2014**).

[Fey57] R. P. Feynman, F. L. Vernon and R. W. Hellwarth. *Geometrical representation of the Schrödinger equation for solving maser problems.* J. Appl. Phys. **28**, 49–52 (**1957**).

[FG03] P. Foster-Gareau, C. Heyn, A. Alejski and B. K. Rutt. *Imaging single mammalian cells with a 1.5 T clinical MRI scanner.* Magn. Reson. Med. **49**, 968–971 (**2003**).

[Fra88] J. Frahm, K. D. Merboldt and W. Hänicke. *Direct FLASH MR imaging of magnetic field inhomogeneities by gradient compensation.* Magn. Reson. Med. **6**, 474–480 (**1988**).

[Fra10] F. Franconi, C. Chapon, J. J. Le Jeune, P. Richomme and L. Lemaire. *Susceptibility gradient quantization by MRI signal response mapping (SIRMA) to dephaser.* Med. Phys. **37**, 877–884 (**2010**).

[Ger22] W. Gerlach and O. Stern. *Der experimentelle Nachweis der Richtungsquantelung im Magnetfeld.* Z. Phys. **9**, 349–352 (**1922**).

[Glo97] A. Glowinski, G. Adam, A. Bücker, J. Neuerburg, J. J. van Vaals and R. W. Günther. *Catheter visualization using locally induced, actively controlled field inhomogeneities.* Magn. Reson. Med. **38**, 253–258 (**1997**).

[Glo98] A. Glowinski, J. Kürsch, G. Adam, A. Bücker, T. G. Noll and

R. W. Günther. *Device Visualization for interventional MRI using local magnetic fields: basic theory and its application to catheter visualization.* IEEE Trans. Med. Imaging **17**, 786–793 (**1998**).

[Gra05] H. Graf, G. Steidle, P. Martirosian, U. A. Lauer and F. Schick. *Metal artifacts caused by gradient switching.* Magn. Reson. Med. **53**, 231–234 (**2005**).

[Gra06] H. Graf, G. Steidle, P. Martirosian, U. A. Lauer and F. Schick. *Effects on MRI due to altered rf polarization near conductive implants or instruments.* Med. Phys. **33**, 124–127 (**2006**).

[Gra12] H. Graf and H. Wojtczyk. *Patent application DE Az.: 10 2012 023 124.5.* German priority date 27.11.2012 (**2012**).

[Haa86] A. Haase, J. Frahm, D. Matthaei, W. Hanicke and K. D. Merboldt. *FLASH imaging. Rapid NMR imaging using low flip-angle pulses.* J. Magn. Reson. **67**, 258–266 (**1986**).

[Haa99] E. M. Haacke, R. W. Brown, M. R. Thompson and R. Venkatesan. *Magnetic resonance imaging: physical principles and sequence design.* Wiley, New York (**1999**).

[Haa04] E. M. Haacke, Y. Xu, Y. N. Cheng and J. R. Reichenbach. *Susceptibility weighted imaging (SWI).* Magn. Reson. Med. **52**, 612–618 (**2004**).

[Haa11] E. M. Haacke and J. R. Reichenbach. *Susceptibility weighted imaging in MRI: basic concepts and clinical applications.* Wiley, Hoboken (**2011**).

[Hah50] E. L. Hahn. *Spin echoes.* Phys. Rev. **80**, 580–594 (**1950**).

[Hin03] K. A. Hinds, J. M. Hill, E. M. Shapiro, M. O. Laukkanen, A. C. Silva, C. A. Combs, T. R. Varney, R. S. Balaban, A. P. Koretsky and C. E. Dunbar. *Highly efficient endosomal labeling of progenitor and stem cells with large magnetic particles allows magnetic resonance imaging of single cells.* Blood **102**, 867–872 (**2003**).

[Hol94] R. W. Holt, P. J. Diaz, J. L. Duerk and E. M. Bellon. *MR susceptometry: an external-phantom method for measuring bulk susceptibility from field-echo phase reconstruction maps.* J. Magn. Reson. Imaging **4**, 809–818 (**1994**).

[Joy89] M. Joy, G. Scott and H. Henkelman. *In vivo detection of applied electric currents by magnetic resonance imaging.* Magn. Reson. Imaging **7**, 89–94 (**1989**).

[Kim09] Y. B. Kim, K. H. Bae, S. S. Yoo, T. G. Park and H. W. Park. *Positive contrast visualization for cellular magnetic resonance*

imaging using susceptibility-weighted echo-time encoding. Magn. Reson. Imaging **27**, 601–610 (**2009**).

[Kok07] I. Koktzoglou, D. Li and R. Dharmakumar. *Dephased FLAPS for improved visualization of susceptibility-shifted passive devices for real-time interventional MRI.* Phys. Med. Biol. **52**, N277–N286 (**2007**).

[Kop56] H. Kopfermann. *Kernmomente.* Akademische Verlagsgesellschaft, Frankfurt a. M. (**1956**).

[Kos08] S. Kos, R. Huegli, G. M. Bongartz, A. L. Jacob and D. Bilecen. *MR-guided endovascular interventions: a comprehensive review on techniques and applications.* Eur. Radiol. **21**, 242–250 (**2008**).

[Lad96] M. E. Ladd, P. Erhart, J. F. Debatin, B. J. Romanowski, P. Boesinger and G. C. McKinnon. *Biopsy needle susceptibility artifacts.* Magn. Reson. Med. **36**, 646–651 (**1996**).

[Lai96] S. Lai, J. R. Reichenbach and E. M. Haacke. *Commutator filter: a novel technique for identification of structures producing significant susceptibility inhomogeneities and its application to functional MRI.* Magn. Reson. Med. **36**, 781–787 (**1996**).

[Lau73] P. C. Lauterbur. *Image formation by induced local interactions: examples employing nuclear magnetic resonance.* Nature **242**, 190–191 (**1973**).

[Lev08] M. H. Levitt. *Spin dynamics: basics of nuclear magnetic resonance.* Wiley, Chichester (**2008**).

[Lew00] M. Lewin, N. Carlesso, C. H. Tung, X. W. Tang, D. Cory, D. T. Scadden and R. Weissleder. *Tat peptide-derivatized magnetic nanoparticles allow in vivo tracking and recovery of progenitor cells.* Nat. Biotechnol. **18**, 410–414 (**2000**).

[Lik79] R. S. Likes. *Moving gradient zeugmatography.* U.S. Patent 4,307,343 (**1979**).

[Liu08] W. Liu, H. Dahnke, E. K. Jordan, T. Schaeffter and J. A. Frank. *In vivo MRI using positive-contrast techniques in detection of cells labeled with superparamagnetic iron oxide nanoparticles.* NMR Biomed. **21**, 242–250 (**2008**).

[Lju83] S. Ljunggren. *A simple graphical representation of Fourier-based imaging methods.* J. Magn. Reson. **54**, 338–343 (**1983**).

[Lue85] K. M. Luedeke, P. Röschmann and R. Tischler. *Susceptibility artefacts in NMR imaging.* Magn. Reson. Imaging **3**, 329–343 (**1985**).

[Man77] P. Mansfield. *Multi-planar image formation using NMR spin echoes.* J. Phys. C **10**, L55–L58 (**1977**).

[Man06] V. Mani, K. C. Briley-Saebo, V. V. Itskovich, D. D. Samber and Z. A. Fayad. *Gradient echo acquisition for superparamagnetic particles with positive contrast (GRASP): sequence characterization in membrane and glass superparamagnetic iron oxide phantoms at 1.5T and 3T.* Magn. Reson. Med. **55**, 126–135 (**2006**).

[Oga90a] S. Ogawa and T. M. Lee. *Magnetic resonance imaging of blood vessels at high field: in vivo and in vitro measurements and image simulation.* Magn. Reson. Med. **16**, 9–18 (**1990**).

[Oga90b] S. Ogawa, T. M. Lee, A. R. Kay and D. W. Tank. *Brain magnetic resonance imaging with contrast dependent on blood oxygenation.* Proc. Natl. Acad. Sci. USA **87**, 9868–9872 (**1990**).

[Par88] H. W. Park, Y. M. Ro and Z. H. Cho. *Measurement of the magnetic susceptibility effect in high-field NMR imaging.* Phys. Med. Biol. **33**, 339–349 (**1988**).

[Pat11] S. Patil, D. Jirak, F. Saudek, M. Hajek and K. Scheffler. *Positive contrast visualization of SPIO-labeled pancreatic islets using echo dephased steady state free precession.* Eur. Radiol. **21**, 214–220 (**2011**).

[Pau36] L. Pauling and C. D. Coryell. *The magnetic properties and structure of hemoglobin, oxyhemoglobin and carbonmonoxyhemoglobin.* Proc. Natl. Acad. Sci. USA **22**, 210–216 (**1936**).

[Pin06a] J. Pintaske, R. Bantleon, R. Kehlbach, C. D. Claussen, J. Wiskirchen and F. Schick. *Effect of concentration of SH U 555A labeled human melanoma cells on MR spin echo and gradient echo signal decay at 0.2, 1.5, and 3T.* Magn. Reson. Mater. Phy. **19**, 71–77 (**2006**).

[Pin06b] J. Pintaske, B. Müller-Bierl and F. Schick. *Geometry and extension of signal voids in MR images induced by aggregations of magnetically labelled cells.* Phys. Med. Biol. **51**, 4707–4718 (**2006**).

[Pos92] S. Posse. *Direct imaging of magnetic field gradients by group spin-echo selection.* Magn. Reson. Med. **25**, 12–29 (**1992**).

[Pur46] E. M. Purcell, H. C. Torrey and R. V. Pound. *Resonance absorption by nuclear magnetic moments in a solid.* Phys. Rev. **69**, 37–38 (**1946**).

[Rab39] I. I. Rabi, S. Millman, P. Kusch and J. R. Zacharias. *The molecu-*

lar beam resonance method for measuring nuclear magnetic moments. Phys. Rev. **55**, 526–535 (**1939**).

[Rau05] A. Rauscher, J. Sedlacik, M. Barth, E. M. Haacke and J. R. Reichenbach. *Nonnvasive assessment of vascular architecture and function during modulated blood oxygenation using susceptibility weighted magnetic resonance imaging.* Magn. Reson. Med. **54**, 87–95 (**2005**).

[Rei97] J. R. Reichenbach, R. Venkatesan, D. A. Yablonskiy, M. R. Thompson, S. Lai and E. M. Haacke. *Theory and application of static field inhomogeneity effects in gradient-echo imaging.* J. Magn. Reson. Imaging **7**, 266–279 (**1997**).

[Sch94] F. Schick, T. Nägele, O. Lutz, K. Pfeffer and J. Giehl. *Magnetic susceptibility in the vertebral column.* J. Magn. Reson. B **103**, 39–52 (**1994**).

[Sch96a] J. F. Schenck. *The role of magnetic susceptibility in magnetic resonance imaging: MRI magnetic compatibility of the first and second kinds.* Med. Phys. **23**, 815–850 (**1996**).

[Sch96b] F. Schick and O. Lutz. *Assessment of the magnetic field distribution in yellow and red bone marrow by the MAGSUS technique.* Magn. Reson. Imaging **14**, 507–519 (**1996**).

[Sco92] G. C. Scott, M. L. G. Joy, R. L. Armstrong and R. M. Henkelman. *Sensitivity of magnetic-resonance current-density imaging.* J. Magn. Reson. **97**, 235–254 (**1992**).

[Sed08a] J. Sedlacik, K. Helm, A. Rauscher, J. Stadler, H. J. Mentzel and J. R. Reichenbach. *Investigations on the effect of caffeine on cerebral venous vessel contrast by using susceptibility-weighted imaging (SWI) at 1.5, 3 and 7 T.* Neuroimage **40**, 11–18 (**2008**).

[Sed08b] J. Sedlacik, C. Kutschbach, A. Rauscher, A. Deistung and J. R. Reichenbach. *Investigation of the influence of carbon dioxide concentrations on cerebral physiology by susceptibility-weighted magnetic resonance imaging (SWI).* Neuroimage **43**, 36–43 (**2008**).

[Seh05] V. Sehgal, Z. Delproposto, E. M. Haacke, K. A. Tong, N. Wycliffe, D. K. Kido, Y. Xu, J. Neelavalli, D. Haddar and J. R. Reichenbach. *Clinical applications of neuroimaging with susceptibility-weighted imaging.* J. Magn. Reson. Imaging **22**, 439–450 (**2005**).

[Seh06] V. Sehgal, Z. Delproposto, D. Haddar, E. M. Haacke, A. E. Sloan, L. J. Zamorano, G. Barger, J. Hu, Y. Xu, K. P. Prab-

hakaran, I. R. Elangovan, J. Neelavalli and J. R. Reichenbach. *Susceptibility-weighted imaging to visualize blood products and improve tumor contrast in the study of brain Masses.* J. Magn. Reson. Imaging **24**, 41–51 (**2006**).

[Sep03] J. H. Seppenwoolde, M. A. Viergever and C. J. G. Bakker. *Passive tracking exploiting local signal conservation: the white marker phenomenon.* Magn. Reson. Med. **50**, 784–790 (**2003**).

[Sep07] J. H. Seppenwoolde, K. L. Vincken and C. J. G. Bakker. *White-marker imaging: deparating magnetic susceptibility effects from partial volume effects.* Magn. Reson. Med. **58**, 605–609 (**2007**).

[Sha13] A. Sharafi and S. Martel. *Magnetic resonance tracking of catheters and mechatronic devices operating in the vascular network with an embedded photovoltaic-based microelectronic circuit.* Conf. Proc. IEEE Eng. MEd. Biol. Soc. 2952–2955 (**2013**).

[Sli96] C. P. Slichter. *Principles of magnetic resonance.* Springer, Berlin (**1996**).

[Sta88] D. D. Stark, R. Weissleder, G. Elizondo, P. F. Hahn, S. Saini, L. E. Todd, J. Wittenberg and J. T. Ferrucci. *Superparamagnetic iron oxide: clinical application as a contrast agent for MR imaging of the liver.* Radiology **168**, 297–301 (**1988**).

[Stu07] M. Stuber, W. D. Gilson, M. Schär, D. A. Kedziorek, L. V. Hofmann, S. Shah, E. Vonken, J. W. M. Bulte and D. L. Kraitchman. *Positive contrast visualization of iron oxide-labeled stem cells using inversion-recovery with on-resonant water suppression (IRON).* Magn. Reson. Med. **58**, 1072–1077 (**2007**).

[Twi83] D. B. Twieg. *The k-trajectory formulation of the NMR imaging process with applications in analysis and synthesis of imaging methods.* Med. Phys. **10**, 610–621 (**1983**).

[Var11] G. Varma, R. E. Clough, P. Acher, J. Senegas, H. Dahnke, S. F. Keevil and T. Schaeffter. *Positive visualization of implanted devices with susceptibility gradient mapping using the original resolution.* Magn. Reson. Med. **65**, 1483–1490 (**2011**).

[Wan00] Y. Wang, Y. Yu, D. Li, K. T. Bae, J. J. Brown, W. Lin and E. M. Haacke. *Artery and vein separation using susceptibility-dependent phase in contrast-enhanced MRA.* J. Magn. Reson. Imaging **12**, 661–670 (**2000**).

[Wan01] Y. J. Wang, S. M. Hussain and G. P. Krestin. *Superparamagnetic iron oxide contrast agents: physicochemical characteristics and applications in MR imaging.* Eur. Radiol. **11**, 2319–2331 (**2001**).

[Wei97] R. Weissleder, H. C. Cheng, A. Bogdanova and A. J. Bogdanov. *Magnetically labeled cells can be detected by MR imaging.* J. Magn. Reson. Imaging **7**, 258–263 (**1997**).

[Woj10] H. Wojtczyk, H. Graf, P. Martirosian, A. Klabes, S. Kegel, V. Ballweg, C. Thomas and F. Schick. *Optimizing the visibility of a carbon fiber cannula in spin echo sequences using currents induced by gradient switching in an attached copper loop: a feasibility study.* Proc. Intl. Soc. Mag. Reson. Med. **18**, 4161 (**2010**).

[Woj11a] H. Wojtczyk, H. Graf, P. Martirosian, V. Ballweg, M. Kraiger, J. Pintaske and F. Schick. *Quantification of direct current in electrically active implants using MRI methods.* Z. Med. Phys. **21**, 135–146 (**2011**).

[Woj11b] H. Wojtczyk, P. Martirosian, V. Ballweg, H. Graf and F. Schick. *MRI near metal objects: investigating the effects of induced RF currents and currents induced by gradient switching on SE phase images using a simple model system.* Proc. Intl. Soc. Mag. Reson. Med. **19**, 4619 (**2011**).

[Won00] E. Y. Wong, Q. Zhang, J. L. Duerk, J. S. Lewin and M. Wendt. *An optical system for wireless detuning of parallel resonant circuits.* J. Magn. Reson. Imaging **12**, 632–638 (**2000**).

[Yab94] D. A. Yablonskiy and E. M. Haacke. *Theory of NMR signal behavior in magnetically inhomogeneous tissues: the static dephasing regime.* Magn. Reson. Med. **32**, 749–763 (**1994**).

[Yab98] D. A. Yablonskiy. *Quantitation of intrinsic magnetic susceptibility-related effects in a tissue matrix. Phantom study.* Magn. Reson. Med. **39**, 417–428 (**1998**).

[Zha00] Y. Zhang, S. J. Dodd, K. S. Hendrich, M. Williams and C. Ho. *Magnetic resonance imaging detection of rat renal transplant rejection by monitoring macrophage infiltration.* Kidney Int. **58**, 1300–1310 (**2000**).

[Zha11] Q. Zhao, J. Langley, S. Lee and W. Liu. *Positive contrast technique for the detection and quantification of superparamagnetic iron oxide nanoparticles in MRI.* NMR Biomed. **24**, 464–472 (**2011**).

[Zho10] R. Zhou, D. Idiyatullin, S. Moeller, C. Corum, H. Zhang, H. Qiao, J. Zhong and M. Garwood. *SWIFT detection of SPIO-labeled stem cells grafted in the myocardium.* Magn. Reson. Med. **63**, 1154–1161 (**2010**).

[Zie05] C. H. Ziener, W. R. Bauer and P. M. Jakob. *Transverse relax-*

ation of cells labeled with magnetic nanoparticles. Magn. Reson. Med. **54**, 702–706 (**2005**).

Contributions

The following persons habe contributed to the publications

[1] Positive contrast imaging of iron oxide nanoparticles with susceptibility-weighted imaging.
Magn Reson Med. 2010;64:1027-1038

[2[Utilizing echo-shifts in k-space for generation of positive contrast in areas with marked susceptibility alterations.
Magn Reson Med. 2012;68:1399-1409

[3] Magnetic resonance visualization of conductive structures by sequence-triggered direct currents and spin-echo phase imaging.
Med Phys. 2014;41:062301

of the present cumulative thesis:

- Rüdiger Bantleon [1,2]:
  Cell labeling and preparation of phantoms and support for the writing of the paragraphs "Cell Phantom" and "Cell Preparation and Phantom".

- Stephan Clasen [3]:
  Applicant and superivsor of the fortüne project "Lokalisierung von Instrumenten in der interventionelle MRT mittels gezielt applizierter Ströme".

- Hansjörg Graf [3]:
  Support for the application of the fortüne project "Lokalisierung von

Instrumenten in der interventionelle MRT mittels gezielt applizierter Ströme" and assistance in the measuring setup and writing of the publication.

- Rainer Kehlbach [1,2]:
  Cell labeling and preparation of phantoms and support for the writing of the paragraphs "Cell Phantom" and "Cell Preparation and Phantom".

- Fritz Schick [1,2]:
  Applicant and supervisor of the DFG project "Strategien zur selektiven Darstellung magnetisch markierter Zellen mittels MRT in verschiedenen Geweben" and assistance in the measuring setup and writing of the publications.

- Günter Steidle [1,2]:
  Assistance in the measuring setup, compilation of the evaluation programs, and writing of the publications.

- Hanne Wojtczyk [3]:
  Support for the application of the fortüne project "Lokalisierung von Instrumenten in der interventionelle MRT mittels gezielt applizierter Ströme".

List of Publications

Publications

- Schäfer R, Bantleon R, Kehlbach R, Siegel G, Wiskirchen J, Wolburg H, Kluba T, **Eibofner F**, Northoff H, Claussen CD, Schlemmer HP
  Functional investigations on human mesenchymal stem cells exposed to magnetic fields and labeled witch clinically approved iron nanoparticles.
  BMC Cell Biol. 2010;11:22
- **Eibofner F**, Steidle G, Kehlbach R, Bantleon R, Schick F
  Positive contrast imaging of iron oxide nanoparticles with susceptibility weighted imaging.
  Magn. Reson. Med. 2010;64:1027-1038
- Steidle G, **Eibofner F**, Schick F.
  Quantitative diffusion imaging of adipose tissue in the human lower leg at 1.5 T.
  Magn. Reson. Med. 2011;65:1118-1124
- Ballweg V, **Eibofner F**, Graf H
  RF tissue-heating near metallic implants during magnetic resonance examinations: an approach in the ac limit.
  Med. Phys. 2011;38:5522-5529
- Kraiger M, Martirosian P, Opriessnig P, **Eibofner F**, Rempp H, Hofer M, Schick F, Stollberger R
  A fully automated trabecular bone structural analysis tool based on T_2^*-weighted magnetic resonance imaging.
  Comput. Med. Imaging Graph. 2012;36:85-94
- **Eibofner F**, Steidle G, Kehlbach R, Bantleon R, Schick F
  Utilizing echo-shifts in k-space for generation of positive contrast in

areas with marked susceptibility alterations.
Magn. Reson. Med. 2012;68:1399-1409

- **Eibofner F**,Wojtczyk H, Graf H, Clasen S
Magnetic resonance visualization of conductive structures by sequence-triggered direct currents and spin-echo phase imaging
Med. Phys. 2014;41:062301
- Grosse U, Henes J, Grözinger G, Kötter I, Martirosian, P, **Eibofner F**, Schick F, Horger M
Anatomic-functional (perfusion-based) magnetic resonance imaging follow-up in patients with rheumatoid arthritis treated with anti-interleukin 6 antibodies: a comparison with clinical scores and serologic data.
J. Comput. Assist. Tomogr. 2015;39:75-82

Conference Contributions

- **Eibofner F**, Pintaske J, Boss A, Schick F
Detection and identification of venous vessels in the lower leg for early diagnosis and characterization of venous diseases with MRI
ESMRMB 2008, Valencia
- Kraiger M, Martirosian P, **Eibofner F**, Rempp H, Schick F
Automatic analysis tool for assessment of trabecular bone quality in the distal femur
ESMRMB 2008, Valencia
- **Eibofner F**, Schick F, Claussen CD
Darstellung von magnetisch markierten Zellen mit positivem Kontrast bei 1.5 Tesla
Experimentelle Radiologie 2009, Mainz
- **Eibofner F**, Schick F, Claussen CD
Nachweis von mit Eisenoxid (SPIO) markierten Zellen in einem Ganzkörper-MRT bei 1.5 Tesla mit positivem Kontrast
Röntgenkongress 2009, Berlin
- **Eibofner F**, Steidle G, Kehlbach R, Bantleon R, Schick F
Positive contrast imaging of iron-oxide nanoparticles by application of a raw-data filter
ESMRMB 2009, Antalya
- Würslin C, Springer F, **Eibofner F**, Schick F
Accurate adipose tissue segmentation from single gradient echo phase

images by adaptive local thresholding
ISMRM 2010, Stockholm

- Springer F, Würslin C, **Eibofner F**, Machann J, Claussen CD, Schick F
  Präzise automatische Segmentierung verschiedener Gewebetypen mittels Phasendifferenz in GRE-Bildern
  Röntgenkongress 2011, Hamburg
- **Eibofner F**, Graf H, Schick F
  Spin-echo phase imaging allows differentiation between wattless and active currents in metallic needles surrounded by media with variable conductivity
  ESMRMB 2012 , Lisbon
- **Eibofner F**, Wojtczyk H, Graf H, Clasen S
  Magnetic resonance visualization of conductive structures by sequence-triggered direct currents and spin-echo phase imaging
  Int. Workshop "Magnetic Resonance Studies" 2014, Bechyně
- **Eibofner F**, Wojtczyk H, Graf H, Clasen S
  Generation of distinct artifacts along conductive structuresin spin-echo phase images by application of sequence-triggered direct currents
  iMRI 2014, Leipzig
- Hoffmann R, **Eibofner F**, Kessler E, Rempp H, Weiß J, Nikolaou K, Clasen S
  In vitro artefact assessment of a prototype MR-compatible microwave antenna for MR-guided tumour ablation and comparison with a standard MR-compatible radiofrequency ablation device
  ECR 2015, Vienna
- Will S, Martirosian P, **Eibofner F**, Schmehl J, Grözinger G, Bantleon R, Vaegler M, Sievert KD, Schick F, Nikolaou K, Kramer U
  Assessment of iron labeled mesenchymal stem cells for endoscopic injection into the porcine urethral sphincter using MRI
  EAU 2015, Madrid

Danksagung

Mein größter Dank gilt Professor Fritz Schick, der es mir ermöglicht hat diese Arbeit anzufertigen. Mit seiner freundlichen Unterstützung und seinem Rat hat er maßgeblich zum Gelingen meiner Forschungsprojekte beigetragen.

Für oftmals fruchtbare Diskussionen und Anregungen und für die Hilfe bei alltäglich anfallenden Problemen möchte ich mich bei den Mitarbeitern der Sektion für Experimentellen Radiologe bedanken. Besonders die langjährigen Sektionsmitarbeiter Hansjörg Graf, Jürgen Machann, Petros Martirosian, Günter Steidle und Karin Werz haben mit ihrer Erfahrung und ihrem Rat bei der Durchführung meiner Projekte sehr geholfen.

Für eine freundliche Zusammenarbeit möchte ich mich außerdem bei meinen jetzigen und ehemaligen Kollegen Verena Ballweg, Rüdiger Bantleon, Bernd Müller-Bierl, Michael Erb, Faezeh Fallah, Patrick Ghibes, Adriane Gröger, Rainer Kehlbach, Uwe Klose, Rupert Kolb, Markus Kraiger, Thomas Küstner, Jörg Pintaske, Cristina Rossi, Holger Schmidt, Michaela Singer, Susanne Will, Hanne Wojtczyk, Christian Würslin, Mao Xiaoxi und Andreas Zimmermann bedanken.

Bezüglich medizinischer Fragestellungen gilt mein Dank dem nicht naturwissenschaftlichen Personal der radiologischen Abteilung Andreas Boss, Stephan Clasen, Ulrich Grosse, Gerd Grözinger, Rüdiger Hoffmann, Christoph Schabel, Jörg Schmehl, Tina Schraml, Nina Schwenzer und ganz besonders Hansjörg Rempp, Fabian Springer und Roland Syha.

Für die Hilfe und Unterstützung während meines Studiums und der Anfertigung dieser Arbeit gilt mein ganz besonderer Dank meiner Familie und vor allem meiner Frau Yana.